

POLITECNICO DI TORINO

Master's Degree in Mechatronic Engineering



Master's Degree Thesis

**EFFICIENT AND GRID FRIENDLY
DC CHARGING STATION**

Supervisors

Prof. RADU BOJOI

Prof. MOHAMMAD SHADMAND

CANDIDATE

PIETRO MINERVA

OCTOBER 2024

ACKNOWLEDGMENT

I am deeply grateful to my MSc advisor, Professor Mohammad Shadmand, for his invaluable insights, endless patience, motivational support, and continuous technical guidance, which were pivotal in navigating me towards the successful completion of my Master's thesis defense. My heartfelt thanks also go out to the distinguished members of my MSc committee: Professor Radu Bojoi and Professor Danilo Erricolo. Their expert advice, constructive discussions, and thoughtful feedback greatly enhanced this journey.

Secondly, I would like to extend my heartfelt thanks to Amirhosein Gohari Nazari. His advice, technical support, and patience have been invaluable, making this journey significantly smoother.

I would like to express my gratitude to all my research colleagues in the Intelligent Power Electronics at Grid Edge (IPEG) Research Laboratory at the University of Illinois Chicago (UIC). Your brilliant support over the year has been invaluable, and I am deeply thankful to each of you.

I want to extend my heartfelt thanks to Jenna Stephens, whose significant support during this challenging academic year has been greatly appreciated. My heartfelt thanks to all the friends who have stood by me this year.

Finally, I would like to express my deepest gratitude to my parents, who have always supported me in pursuing my dreams and facing my challenges. If I have become the person I believe I am today, it is only because of you. I cannot forget to extend my thanks to my brother

ACKNOWLEDGMENT (Continued)

Carlo; you have been and always will be my guide. I am fortunate never to have been alone throughout my entire university journey, and I owe this especially to all my friends, including Cosimo, Leonardo, and Francesca, as well as my grandparents and close family members: with you, I have understood the true values of family.

Thank you all for believing in me more than I have in myself during these years. Now, it is time for me to take my own path and start believing in myself as much as you all have.

PM

CONTRIBUTIONS OF AUTHORS

Major parts of the results and discussions in this thesis are taken from my accepted for publication paper at IEEE. Below, the contributions of all the co-authors are listed. Authors' contributions in IEEE IECON 2024: P. Minerva, A.G. Nazari, and M. Shadmand, conceived the main idea. P. Minerva led the investigations and conducted the analytical analysis, technical results, and write-up. A.G. Nazari, M. Shadmand, and S. Bayhan contributed to review the write-up of the manuscript.

TABLE OF CONTENTS

<u>CHAPTER</u>		<u>PAGE</u>
1	INTRODUCTION	1
1.1	Background and motivations	1
1.2	Master’s Thesis research Scope	6
1.3	Structure	6
2	LITERATURE REVIEW	8
2.1	Charging Stations	8
2.2	DC-DC Converters For Charging Stations	11
2.2.1	Dual-Active-Bridge (DAB) Converter	12
2.2.2	Resonant Converters	13
2.2.2.1	Soft-Switching in Resonant Converters	16
2.2.2.2	Switch Network, Rectifier and Capacitive Filter Networks Analysis	17
2.2.3	CLLC Converter	21
2.2.3.1	Control of CLLC Converter	25
2.3	From Grid-Following to Grid-Forming Inverters	29
2.3.1	Grid-Following	29
2.3.2	Grid-Forming	30
3	CLLC CONVERTER ANALYSIS AND DESIGN	33
3.1	Introduction	33
3.2	Voltage Gain Analysis	33
3.2.1	First-Harmonic-Approximation	33
3.2.1.1	Forward Mode Equivalent Circuit	35
3.2.1.2	Reverse Mode Equivalent Circuit	37
3.3	Operating Principles	39
3.4	Design Procedure and Parameters Selection	43
3.4.1	Design Procedure	43
3.4.2	Design Parameters Choice	48
3.4.3	DC Charging stations Voltage Gains Considerations	51
3.4.3.1	Discharging Mode - V2G	51
3.4.3.2	Charging Mode - G2V	53
4	CONTROL OF CLLC CONVERTER	54
4.1	Proposed Control Strategy for CLLC Converter	54
4.1.1	Charging Mode - G2V	54
4.1.1.1	Soft-Switching Validation in Charging Mode	55

TABLE OF CONTENTS (Continued)

<u>CHAPTER</u>		<u>PAGE</u>	
	4.1.1.2	Simulation results - G2V	57
	4.1.2	Discharging Mode - V2G	59
	4.1.2.1	Soft-Switching Validation in Discharging Mode	60
	4.1.2.2	Simulation results - V2G	61
5	DC CHARGING STATIONS INTEGRATION IN GRID	65	
	5.1	Proposed System	65
	5.2	DC Microgrid Stability Analysis	65
	5.3	Minimum Line Losses Algorithm - V2G	74
	5.3.1	Simulation Results	75
	5.3.1.1	Case 1	76
	5.3.1.2	Case 2	80
	5.3.1.3	Case 3	84
	5.3.1.4	Case 4	88
	5.3.1.5	Case 5	91
6	CLOSING REMARKS AND FUTURE WORK	96	
	6.1	Closing Remarks	96
	6.2	Future Work	97
	CITED LITERATURE	98	
	VITA	108	

LIST OF TABLES

<u>TABLE</u>		<u>PAGE</u>
I	CHARGING STATION TYPOLOGIES (1)	11
II	BIDIRECTIONAL DC-DC CONVERTERS IN LITERATURE (1)	23
III	HYBRID MODULATION STRATEGIES (2)	28
IV	DESIGN PARAMETERS	52
V	PARAMETERS FOR STABILITY ANALYSIS	73
VI	OPTIMIZATION PARAMETERS FOR 1st CASE OF STUDY . .	79
VII	RESULTS FOR 1st CASE OF STUDY	79
VIII	OPTIMIZATION PARAMETERS FOR 2nd CASE OF STUDY . .	83
IX	RESULTS FOR 2nd CASE OF STUDY	83
X	OPTIMIZATION PARAMETERS FOR 3rd CASE OF STUDY . .	87
XI	RESULTS FOR 3rd CASE OF STUDY	87
XII	OPTIMIZATION PARAMETERS FOR 4th CASE OF STUDY . .	91
XIII	RESULTS FOR 4th CASE OF STUDY	91
XIV	OPTIMIZATION PARAMETERS FOR 5th CASE OF STUDY . .	95
XV	RESULTS FOR 5th CASE OF STUDY	95

LIST OF FIGURES

<u>FIGURE</u>		<u>PAGE</u>
1	Smart-Grid: Incorporation of V2G into the grid	5
2	Charging Stations interfaced with DC Power Distribution (1)	6
3	EV Charging System (1)	9
4	DAB Converter Circuit. (a) Bidirectional FBDAB circuit, (b) HBDAB circuit, (c) Current-fed DAB Converter	14
5	Resonant Converter Circuit (3)	15
6	Resonant Tank Topologies. (a) Series tank network, (b) Parallel tank network (3)	15
7	DC-DC resonant converter (3)	16
8	Soft-switching in series resonant converter. (a) Zero-current switching (ZCS), (b) zero-voltage switching (ZVS) (3)	17
9	Waveforms of $v_s(t)$, $v_{s1}(t)$, $i_s(t)$, and $i_g(t)$. (a) Voltage waveforms, (b) current waveforms (3)	19
10	Equivalent model after FHA (3)	19
11	Waveforms of interest for rectifier network. (a) Real waveforms v_R , and i_R , (b) fundamental components v_{R1} , and i_{R1} (3)	20
12	Equivalent circuit for input rectifier with resonant tank, and DC load (3)	21
13	Traditional Modulation Strategies for CLLC Converter Control. (a) Pulse Frequency Modulation (PFM), (b) Primary-Side Phase-Shift Modulation (PSPSM), (c) Secondary-Side Phase-Shift Modulation (SSPSM), (d) Primary-Side Pulse Width Modulation (PSPWM), (e) Secondary-Side Pulse Width Modulation (SSPWM)	27
14	Grid-Forming Inverter Control Strategy. (a) Virtual Synchronous Machine Emulation, (b) Voltage and Frequency Regulation based on Droop Control, (c) Virtual Oscillator Control (VOC)	32
15	CLLC Resonant Converter Circuit	34
16	Equivalent Circuit in G2V Mode	37
17	Equivalent Circuit in V2G Mode	38
18	CLLC converter operating modes for G2V direction. (a) 1st Mode (t_1-t_2), (b) 2nd Mode (t_2-t_3), (c) 3rd Mode (t_3-t_4), (d) 4th Mode (t_4-t_5), (e) 5th Mode (t_5-t_6), (f) 6th Mode (t_6-t_7),	39
19	CLLC converter waveforms below resonance frequency	44
20	Flow Chart for design procedure (4)	45
21	Variation of voltage gain with $C_{r1} = C'_{r2}$ and without it for charging mode for $R_{load} = 35\Omega$	49
22	Variation of voltage gain with $C_{r1} = C'_{r2}$ and without it for discharging mode for $R_{load} = 35\Omega$	49

LIST OF FIGURES (Continued)

<u>FIGURE</u>		<u>PAGE</u>
23	Voltage gain curve for different values of L_{r2} based on design simplification for $R_{load} = 35\Omega$	49
24	Voltage gain curve for different values of h for $R_{load} = 12\Omega$	49
25	Voltage gain curve for different values of h for $R_{load} = 228\Omega$	50
26	Voltage gain curve under different load conditions	50
27	Proposed Control Strategy - G2V	55
28	Soft-Switching Validation - G2V	56
29	Control Validation after switching from Constant Current (CC) to Constant Voltage (CV). (a) Battery Voltage vs Time, (b) Frequency vs Time, (c) Battery Current vs Time, (d) SOC vs Time	58
30	Resonant Tank Currents Waveforms	58
31	Proposed Control Strategy - V2G	59
32	Soft-Switching Validation - V2G	60
33	Voltage Step-up under Closed-Loop Control. (a) Voltage Error vs Time, (b) Frequency vs Time	61
34	Voltage Step-down under Closed-Loop Control. (a) Voltage Error vs Time, (b) Frequency vs Time	62
35	Voltage Step-up under Closed-Loop Control. (a) Voltage Error vs Time, (b) Frequency vs Time	63
36	Voltage Step-down under Closed-Loop Control. (a) Voltage Error vs Time, (b) Frequency vs Time	64
37	Proposed System Structure	65
38	Schematic for Proposed DC system	66
39	Equivalent circuit of the proposed dc system	67
40	Case 1 without Proposed Algorithm. (a) Power Injected, (b) Power Losses	77
41	Case 1 with Proposed Algorithm. (a) Power Injected, (b) Power Losses	78
42	Case 2 without Proposed Algorithm. (a) Power Injected, (b) Power Losses	81
43	Case 2 with Proposed Algorithm. (a) Power Injected, (b) Power Losses	82
44	Case 3 without Proposed Algorithm. (a) Power Injected, (b) Power Losses	85
45	Case 3 with Proposed Algorithm. (a) Power Injected, (b) Power Losses	86
46	Case 4 without Proposed Algorithm. (a) Power Injected, (b) Power Losses	89
47	Case 4 with Proposed Algorithm. (a) Power Injected, (b) Power Losses	90
48	Case 5 without Proposed Algorithm. (a) Power Injected, (b) Power Losses	92
49	Case 5 with Proposed Algorithm. (a) Power Injected, (b) Power Losses	94

SUMMARY

Major parts of the results and discussions in this thesis chapter are derived from my paper accepted for publication at IEEE IECON 2024 (4). With the transition towards renewable energy sources (RESs) such as hydropower, solar, wind, bioenergy, and geothermal energy, future power grids will move away from traditional generators, which could reduce their inertia and make them more vulnerable to fluctuations in frequency and voltage. It's essential to find suitable energy sources to enhance grid stability in response to load changes or generation loss (5). As electric vehicles (EVs) become more prevalent, integrating them into the power grid through DC charging stations offers a promising solution. The use of vehicle-to-grid (V2G) technology allows EVs to contribute to grid support services like ancillary services, load balancing, peak shaving, and frequency regulation, thereby improving grid reliability and safety (6), (7). To enable V2G functionalities, charging stations should be equipped with bidirectional power converters. CLLC converters are a valid technology, since they can maintain consistent performance in both operational modes, with high efficiency, reduced switching losses, improved voltage regulation, and enhanced power density (8). For V2G applications, the capability for power to flow in both directions is crucial, as it allows the surplus energy from the EV battery to be fed back into the power grid.

Various optimization algorithms have been developed to meet power demand, support the grid during peak times, and maximize revenue. In (9), a Binary particle swarm optimization (BPSO) algorithm was implemented to schedule the operations in the EV parking lot to

SUMMARY (Continued)

maximize the revenue from selling and minimize the purchase cost. Another study achieved frequency regulation through the development of an optimal V2G aggregator (10). Also, (11) implemented a real-time V2G control algorithm under price uncertainty to get the highest revenue from selling energy.

This thesis outlines an accurate design procedure for the CLLC converter in the DC charging stations, which is suitable for First-Harmonic-Approximation (FHA) assumption. It works closely to the resonant frequency in a narrow switching frequency interval above it in both operating conditions, with ZVS and a reasonable operating voltage range for a DC bus in the DC microgrid.

To enable G2V operation, a closed-loop voltage controller and a closed-loop current controller to achieve constant voltage (CV) charging and constant current (CC) are implemented. Instead, the discharging mode (V2G) operates with soft-start under constant voltage (CV) operation, and a voltage closed loop controller is implemented. Both control strategies have been validated through simulations, demonstrating soft switching for both full-bridges. Also, in this thesis, an algorithm that aims to minimize the losses incurred from injecting energy from the fleet of EVs in the charging station into the grid is proposed. The algorithm updates the power to be drawn from each EV based on the arrival state of charge (SOC), recalculating it every time there is an EV arrival or departure from the charging station (4).

CHAPTER 1

INTRODUCTION

1.1 Background and motivations

Major parts of the results and discussions in this thesis chapter are derived from my paper accepted for publication at IEEE IECON 2024 (4). It is currently estimated that 11% of global carbon dioxide emissions come from personal vehicles that are powered by fossil fuels (12). To decrease greenhouse gas emissions, and reduce the dependence on carbon fossil fuels while providing a cleaner and quieter mode of transportation, it is believed that electric vehicles (EVs) are the most viable and sustainable solution. One contributing factor is the superior efficiency of electric vehicles (EVs) compared to internal combustion engines (ICE). While ICEs typically achieve an efficiency rate of around 60%, EVs can reach efficiency rates as high as 90% (13). As the global use of EVs continues to rise, it is becoming increasingly important to integrate them into the electric grid (4). In (14) the tons of CO₂ emissions generated by internal combustion engine vehicles (ICEV), hybrid electric vehicles (HEV), plug-in hybrid electric vehicles (PHEV), and battery electric vehicles (BEV), showing a clear decreasing impact on the emissions between 2023 and 2035 prediction.

However, it is important to note that if EVs are only used in charging mode, they may impact on distribution networks. In the future, power grids will rely more on renewable energy sources like hydropower, solar, wind, bioenergy, and geothermal energy (15; 4).

The International Energy Agency (IEA) forecasts a renewable capacity growth of approximately 3,700 GW over the next five years, representing a 147% increase compared to the growth observed during the 2017-2022 period. By 2025, renewable energy sources are expected to surpass coal as the primary means of electricity generation. To reach a global renewable energy capacity of 11,000 GW by 2030, the capacity would need to triple from 2022 levels, in alignment with the IEA's Net Zero Emissions by 2050 Scenario. The accelerated scenario considers predictions based on improvements in government policies (16).

In addressing this challenge, four key issues need to be considered (16):

1. Policy Uncertainties and delays: Governments' interventions in energy markets during crises introduced uncertainty for investors, negatively affecting the investment environment. This was exacerbated by inflexible auction designs, a lack of adjustments for reference prices, and project contract price indexation, primarily impacting projects in advanced economies.
2. Insufficient Grid Infrastructure Investment: Over 3000 GW of renewable capacity is waiting in the queue due to inadequate grid infrastructure, a bottleneck for both advanced and developing nations. Also, the lengthy development times for grid improvements significantly lag those of renewable projects like wind and solar PV.
3. Complex Permitting Processes: Obtaining permits can take anywhere from one to nine years, depending upon the project type. These protracted and complex authorization procedures slow down the growth of project pipelines, increase risks and costs, and deteriorate project economics.

4. Inadequate Financing in Developing Countries: High-risk environments, policy uncertainties, and government-owned utilities under financial stress result in higher capital costs, reducing the bankability of renewable projects. A reduction in the weighted average cost of capital could significantly lower generation costs for wind and solar PV.

These hurdles collectively impede the global transition to renewable energy, calling for innovative solutions and international cooperation to overcome them.

As we integrate more renewable energy sources (RESs) into our power grids, we're transitioning away from traditional generators. This shift decreases the grid's inertia, making it more susceptible to issues like frequency and voltage fluctuations, including harmonic distortion. To address these challenges, it's crucial that we make enhancements to the grid infrastructure. To counteract this, a new energy source is needed to support the grid, transforming EVs from mere consumers of electricity to active participants in the energy ecosystem. Electric Vehicle (EV) parking lots are a great candidate for this, thanks to the potential bidirectionality of EVs. When energy is transferred from the vehicle to the grid - known as Vehicle-to-Grid (V2G) technology - it can support the grid. In particular, taking part in ancillary services, load balance, load peak shaving, and frequency regulation (7), or simply supplying the grid during peak demand periods. Moreover, V2G technology presents economic advantages for EV owners, allowing them to capitalize on the energy stored in their vehicle batteries. By engaging in grid services or demand response initiatives, EV owners can generate additional income, offsetting the costs associated with vehicle ownership and charging infrastructure, thereby making EVs an even more appealing option for consumers (17; 18).

In Figure 1 (19), a V2G system incorporated into the grid is shown. On the left, a simple grid connection is illustrated. For the grid compliant case, also defined as level 0 by DIN/ISO 15118-20, unidirectional charging is allowed, and the only local utility, defined as distribution system operator (DSO), manages the load conditions by distributing electricity to end-users based on the information received from the transmission system operator (TSO), which is responsible for large-scale electricity transmission. Another possibility, when the electric vehicle (EV) is a load for the infrastructure, consists of the controlled case, where more charging options are available with different power levels for charging, and the time for the charging operations is well defined. Moving towards grid integrations, level 2 is defined by cooperative charging EVs. Here, more EVs can be connected, and the price is defined based on grid conditions. A further improvement is shown at level 3, where the charging power flow is bidirectional, allowing energy storage. Finally, Level 4 shows aggregated fleets, suitable for private companies' charging infrastructures, allowing bidirectional energy flow between the vehicles and the grid.

The introduction of microgrids in "smart-grids" meets all the problems explained above, such as low inertia in the grid due to the increased amount of RES, the high electricity demand, and the necessary reduction of greenhouse gas emissions (20). They can mainly operate under two modes: grid-connected mode when the microgrid is connected to the main distribution network, or islanded mode, when it is isolated. Its capability of working as generator or consumer makes it suitable for bidirectional power flow systems. For this kind of application, both AC and DC distribution networks are valid systems to be interfaced with charging stations. The main advantages of alternate-current solutions are easier protection, and the metering is

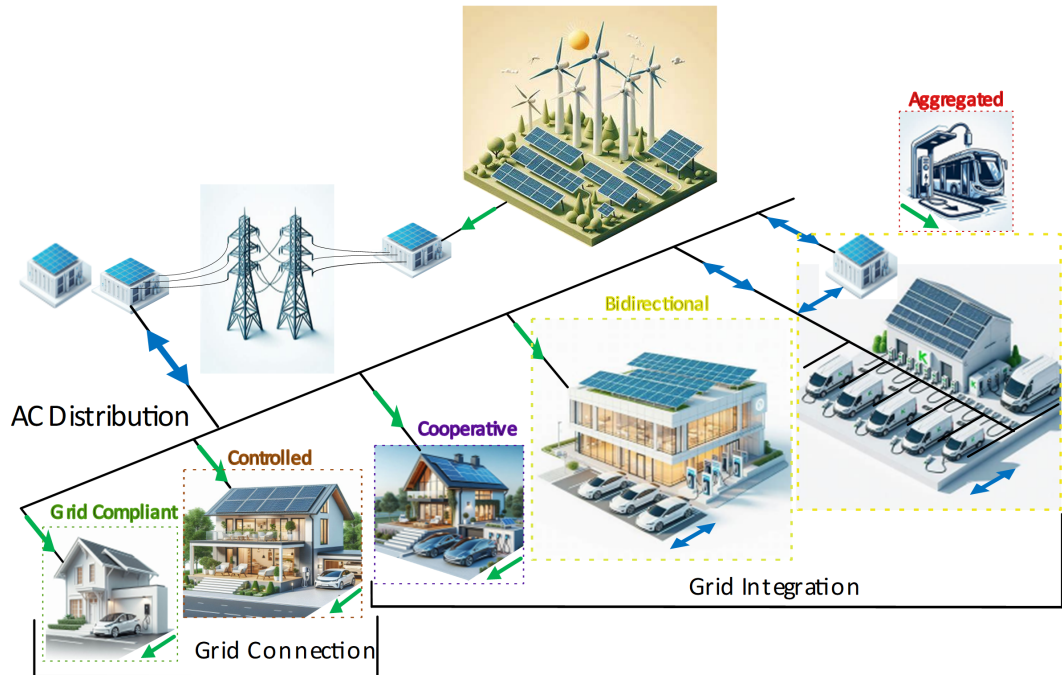


Figure 1: Smart-Grid: Incorporation of V2G into the grid

already standardized. On the other hand, DC connection offers fewer conversion stages, higher efficiency, and simpler control. It eliminates the synchronization problem and reactive power flow. However, it requires an active front-end rectifier, a more complex protection system, and non-standardized metering (20; 21). By the way, the increasing adoptions of DC microgrids is justified by the wide spread of dc loads and RES. In Figure 2, a system formed by four charging stations with DC power distribution is shown (4).

The integration between the DC distribution system with EV charging stations, rely on bidirectional DC-DC converters (BDCs) to allow bidirectional power flow allowing charging and discharging operations. In particular, to satisfy safety requirements, isolated configurations are

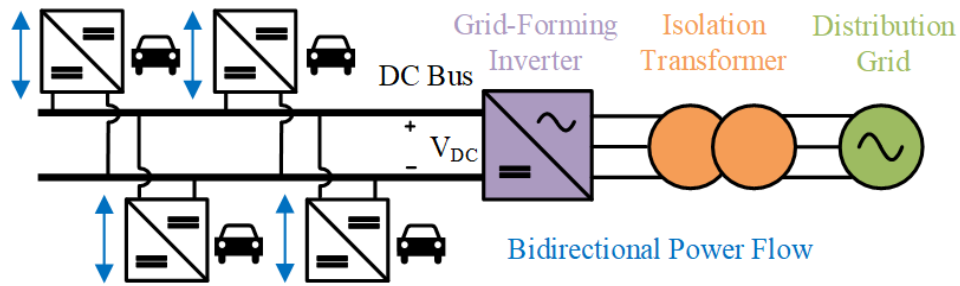


Figure 2: Charging Stations interfaced with DC Power Distribution (1)

more adapt. Galvanic isolation from the grid, can be included before the inverter stage in case of nonisolated converter by inserting a line-frequency transformer. Otherwise, topologies with high-frequency transformer implemented in the DC-DC converter are another valid option to provide isolation.

1.2 Master's Thesis research Scope

The presented work aims at enhancing the efficiency and grid-interaction of DC charging stations interfaced with the AC grid. This requires

1. Optimal design and control of Bidirectional DC-DC converter topology for meeting the requirements of DC charging stations
2. Planning optimal DC charging station operations to minimize total system losses, improve overall efficiency and provide support to the AC grid

1.3 Structure

The thesis work is structured as follows:

1. State-of-the-art techniques for Bidirectional DC-DC Converters in Charging Stations, control strategies in literature for CLLC resonant converters, and transition from grid-following to grid-forming inverters
2. Analysis and design for the CLLC DC-DC converter in grid-to-vehicle and vehicle-to-grid modes
3. Implementation of control strategies for the CLLC converter in DC charging stations
4. Presenting an energy management strategy to reduce line losses

CHAPTER 2

LITERATURE REVIEW

2.1 Charging Stations

With the rise of electric vehicles (EVs), conveniently located charging stations are becoming increasingly important. There are various types of EV charging stations, based on AC or DC charging and the charging level. In Figure 3 (1), two possible EV charging systems are illustrated for both on-board and off-board typologies. The AC connections are defined by red lines, while blue lines are adopted at DC level. For both configurations, the eMotor is directly connected to a DC-AC inverter that is interfaced on the DC side to a common DC Bus. In this stage, the system is bidirectional since the eMotor can work under traction and braking mode. Moreover, an electronic load can be connected to a DC-DC converter, that interfaces the common bus on the other side. The DC common bus is connected to a supercapacitor or a low-voltage (LV) battery (usually at 12 V). Also, a DC-DC converter is connected between the DC bus and the high-voltage (HV) battery pack. When an On-Board charger is implemented, the connection between the battery pack and the grid is made by an AC-DC power conversion (typically unidirectional) with a two-stage topology inside the On-Board charger. The on-board system is fed from a dedicated AC charging station or domestic outlets. It is formed by a PFC rectifier (power-factor-corrector) with sinusoidal input current and unity PF, connected to an isolated DC-DC converter. Otherwise, an off-board charger can be included, but using DC

charging stations. The off-board charger follows the same structure as the on-board one, but it is embedded in the charging station. Also, in this case, the power flow can be bidirectional, allowing both charging and discharging operations between the electric vehicles and the charging stations.

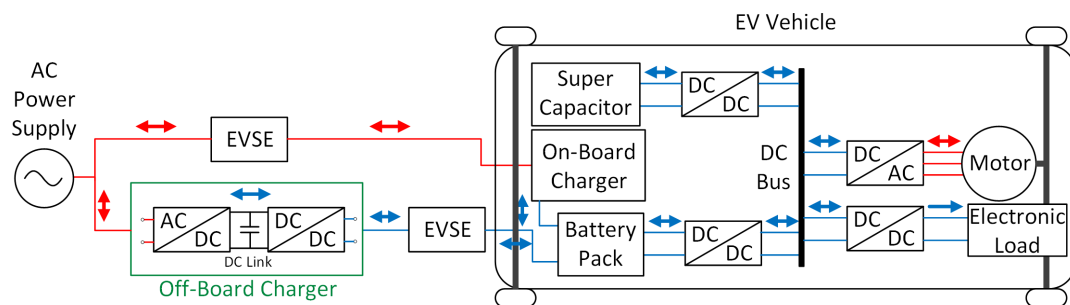


Figure 3: EV Charging System (1)

Different charging level typologies are presented in Table I (1). Conductive battery chargers for electric vehicles are categorized into different levels based on their power levels and corresponding charging times. These categories help in understanding the capabilities of each type of charger.

Level-1 (AC) Charging is typically used for residential charging and involves on-board chargers. These chargers operate on a standard 120/230V AC power supply with a current range of 12A to 16A in single-phase. The power output of Level-1 chargers is lower than 2 kW. Due to their lower power output, these chargers require a longer duration to fully charge an electric

vehicle, typically taking between 11 to 36 hours for EVs with a battery capacity of 16 to 50 kWh (1).

Level-2 (AC) Charging is more suitable for both residential and workplace environments, using on-board chargers that operate on a 208/240V AC power supply. These chargers can handle a higher current range of 15A to 80A in single or split-phase configurations, delivering power levels between 3.1 kW and 19.2 kW. As a result, Level-2 chargers can significantly reduce charging time, taking approximately 2 to 6 hours to charge EVs with a battery capacity of 16 to 30 kWh (1).

Level-3 (DC Fast) Charging stations are designed for public and commercial locations, where fast charging is crucial. These off-board chargers utilize a 300-600V DC power supply and can deliver high power levels ranging from 50 kW to 350 kW. They are capable of providing a rapid charge, reducing the time required to less than 30 minutes for EVs with a battery capacity of 20 to 50 kWh. This makes them ideal for use in public charging stations and locations where quick turnaround is essential (1).

The next generation of DC Ultra-Fast Charging is pushing the boundaries even further. These off-board chargers operate with an 800V DC power supply or higher, and can deliver power levels starting at 400 kW and going upwards. Such chargers are designed to offer extremely rapid charging times, approximately 10 minutes for EVs with a battery capacity of 20 to 50 kWh. This advanced technology is particularly beneficial for high-traffic public charging stations and future-proofing the infrastructure for electric vehicles with larger battery capacities (1).

In summary, the progression from Level-1 to Ultra-Fast DC charging represents significant advancements in charging technology, with each level offering faster and more efficient solutions to meet the diverse needs of electric vehicle owners.

TABLE I: CHARGING STATION TYPOLOGIES (1)

Charging Station Type	Power Supply and Level	Charging Time
Level-1 (AC) On-board (home)	120/230V _{ac} , 12A-16A, 1.44kW-1.92kW	11-36 hours for EVs
Level-2 (AC) On-board (domestic or workplace)	208/240V _{ac} , 15A-80A (Single/split phase), 3.1kW-19.2kW	2-6 hours for EVs
Level-3 (DC Fast) Off-board (public places)	300-600V _{dc} , Maximum current 400A, (Three phase), 50kW-350kW	≤ 30 minutes for EVs
DC Ultra-Fast Charging Off-board (public places)	400-1000V _{dc} , ≥ 400A (Polyphase), ≥ 400kW	~ 10 minutes for EVs

2.2 DC-DC Converters For Charging Stations

Major parts of the results and discussions in this thesis chapter are derived from my paper accepted for publication at IEEE IECON 2024 (4). In (21; 1) the critical role of isolated DC-DC converters in facilitating rapid and efficient charging of electric vehicle (EV) batteries is highlighted. Various isolated and non-isolated DC-DC converter topologies suitable for DC fast off-board chargers are discussed, including unidirectional and bidirectional configurations. Here, only the bidirectional converter topologies are discussed, such as bidirectional isolated DC-DC converters like the dual active bridge (DAB) and CLLC converters. In (22) an analysis

and comparison between the two topologies have been provided, with valuable insights into design methodologies and performance evaluation criteria.

2.2.1 Dual-Active-Bridge (DAB) Converter

DAB converter is a bidirectional isolated DC/DC converter often used in electric vehicle (EV) charging applications due to its high power density, efficiency, and ability to handle both bucks and boost operations effectively (23). The DAB converter achieves bidirectional power flow by controlling phase shift between the primary and secondary voltages leverages the transformer's leakage inductance for power transfer. Additionally, the DAB converter operates with minimal device stress, thanks to its inherent zero-voltage switching (ZVS) operation for both bridges (24), leading to improved reliability and longevity of power semiconductor devices. Soft-switching capability is facilitated by involving snubber capacitors into the DAB architecture. Moreover, advancements in semiconductor technologies, such as SiC and GaN devices, have further enhanced the efficiency and power density of DAB converters (25). However, the DAB converter also has some drawbacks. One challenge is the design of the leakage inductance, which is crucial for achieving wide operating ranges and maintaining efficiency (26). Designing the leakage inductance involves a tradeoff between achieving a wide ZVS range and minimizing reactive power flow, which can impact the efficiency (27). Additionally, the DAB converter may suffer from high-frequency charging ripple due to reactive power inherent in its operation (28). Despite these challenges, ongoing research and development efforts aim to mitigate these drawbacks and further improve the performance of DAB converters for EV charging and other applications.

Exploring the main solutions within DAB converters brings us to two predominant types: Voltage-fed DAB and Current-fed DAB, each with its unique advantages and challenges (29).

Starting with Voltage-fed DAB, the standout advantage is its suitability for a wide voltage range, making it particularly suitable for applications like vehicle-to-grid technologies. However, it is essential to recognize challenges such as restricted voltage conversion range, high circulating current, and increased reactive power injection (29).

On the other hand, the Current-fed DAB topology is characterized by its extensive input voltage range, low input currents, and significant reductions in diode ringing and the transformer turns ratio. It is notable for its zero duty cycle loss, higher voltage gains, fewer diodes, lower transformer turns ratio, and improved current control capabilities. However, to diminish the switching losses found in current-fed converters, it's necessary to employ active snubbers to alleviate spikes, although this could lead to higher costs. Snubber capacitors are typically implemented across the switching devices, as referenced in (30; 31; 32; 33; 34; 35; 36). This strategy is effective in mitigating transients during switching, reducing voltage and current spikes, cutting down on electromagnetic interference, and alleviating issues with diode reverse recovery. In Figure 4 the Full-Bridge Voltage Fed DAB converter, the half-bridge DAB converter and the Current-fed DAB are shown (37).

2.2.2 Resonant Converters

Resonant power converters feature L-C resonant networks. Each switching period involves different operations, with voltages and currents exhibiting sinusoidal variations within each subinterval. This converter topology usually operates at frequencies that can span between

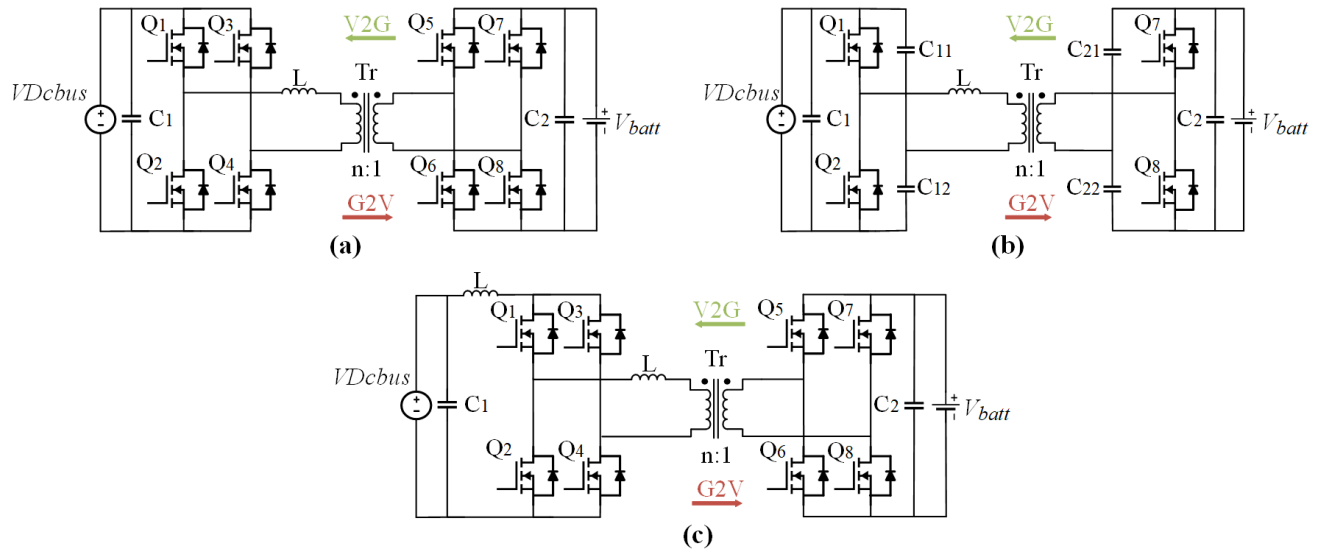


Figure 4: DAB Converter Circuit. (a) Bidirectional FBDAB circuit, (b) HBDAB circuit, (c) Current-fed DAB Converter

tens to hundreds of kHz. The main structure of a resonant inverter is shown in Figure 5 (3). It is basically formed by a switch network and a resonant tank. Different types of resonant tanks are shown in Figure 6. They can be differentiated into series resonant and parallel resonant. The first category shows the resonant tank in series with the load, while parallel resonant converters have their resonant tank in parallel with the load (3).

The most common tank networks are the LCC and LLC. In the LCC topology, a tank capacitor is used in series and parallel with the load, while in the LLC topology, the inductor is both in series and parallel with the load. Using rectifiers and filtering the output, the resonant inverter can be transformed into a DC-DC resonant converter as in Figure 7 (3).

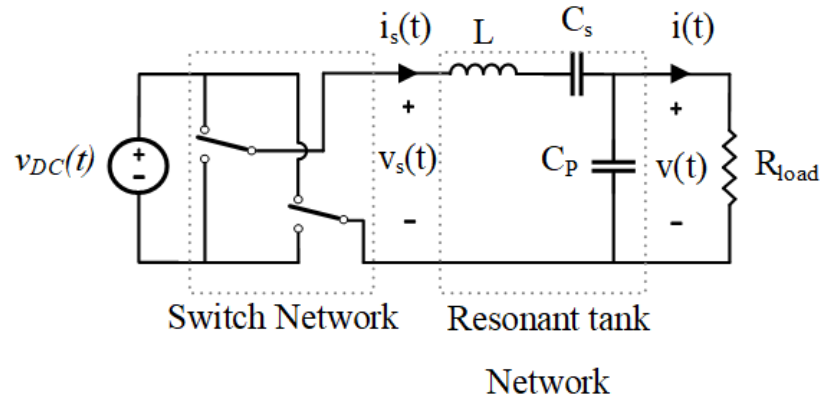


Figure 5: Resonant Converter Circuit (3)

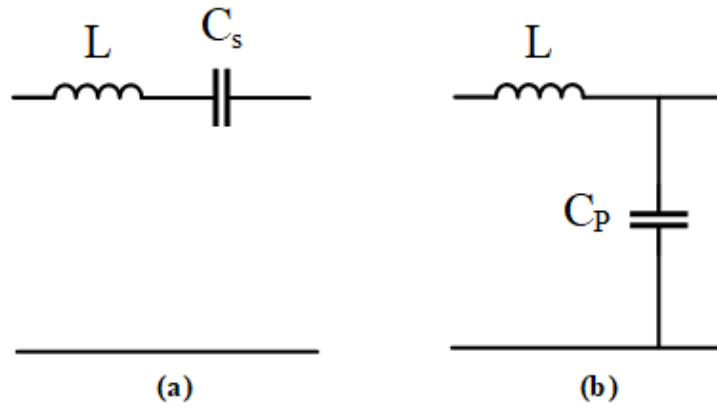


Figure 6: Resonant Tank Topologies. (a) Series tank network, (b) Parallel tank network (3)

Series resonant converters work by stepping down the voltage. When the transformer ratio has a unitary value, the output voltage is lower than the input voltage above and below the resonant frequency. On the other hand, for parallel resonant converters, the voltage gain depends on the switching frequency.

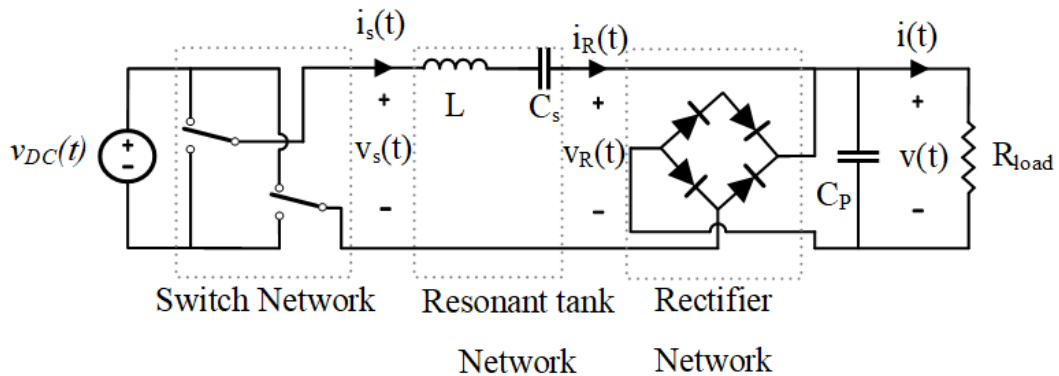


Figure 7: DC-DC resonant converter (3)

2.2.2.1 Soft-Switching in Resonant Converters

Soft-switching in resonant converters can lead to reduced switching loss through zero-current switching (ZCS) and zero-voltage switching (ZVS). For both series and parallel full-bridge resonant converters operating below the resonant frequency, ZCS condition can be obtained. Basically, it happens when the current circulating through the switching device goes to zero before it is turned off. In other words, this phenomenon appears in the presence of a capacitive load to the switches, such that i_s crosses zero before v_{s1} crosses zero voltage. Under this operation, the resonant tank impedance is dominated by the capacitor, then the switch current i_s leads the fundamental switch voltage v_{s1} . Figure 8(a) (3) shows ZCS for a series resonant converter. Instead, above the resonant frequency, the inductor dominates the resonant tank impedance, showing zero-voltage switching and the switch output voltage v_s leads the switch current i_s . Then, v_s anticipates i_s in the zero-crossing. Figure 8(b) (3) shows ZVS for a series resonant converter.

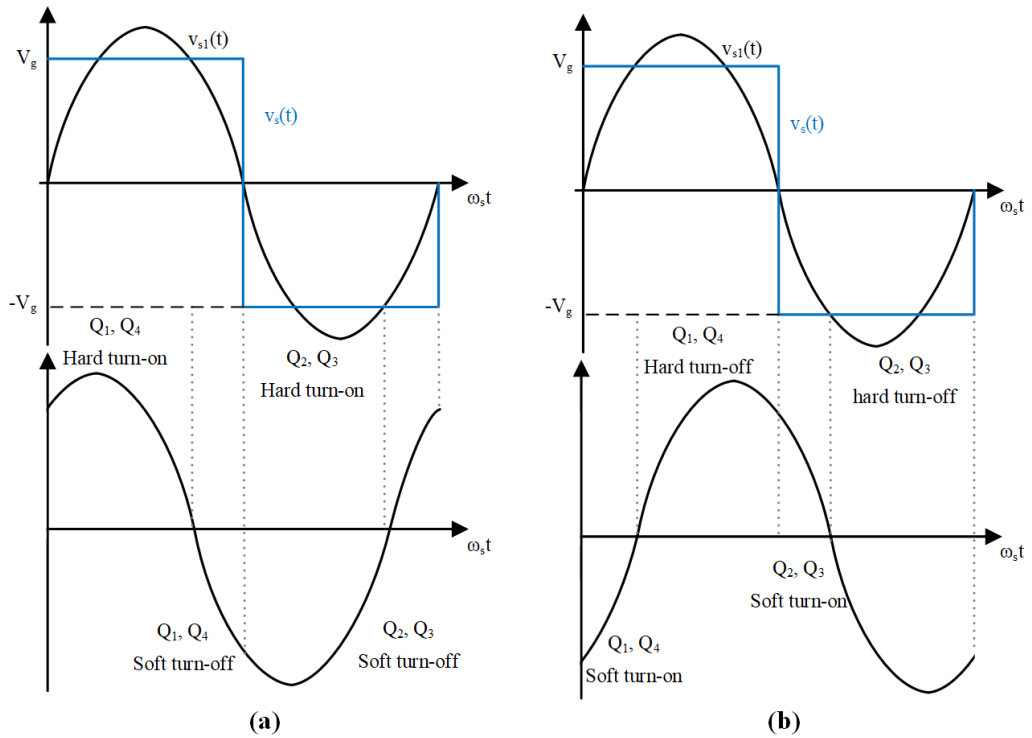


Figure 8: Soft-switching in series resonant converter. (a) Zero-current switching (ZCS), (b) zero-voltage switching (ZVS) (3)

2.2.2.2 Switch Network, Rectifier and Capacitive Filter Networks Analysis

When the resonant converter operates close to the resonant frequency, the fundamental components can approximate v_s , neglecting the harmonic frequencies nf_s , where $n = 3, 5, 7, \dots$. The switch output v_s is a square waveform, whose frequency f_s must be close to the resonant frequency f_r . Under these assumptions, first-harmonic-approximation (FHA) is a valid tool to retrieve the fundamental components of $v_s(t)$, $i_s(t)$, $i_R(t)$, and $v_R(t)$. Considering the switch

network in Figure 7, the output voltage $v_s(t)$ is a square wave with frequency f_s defined by the Fouries series as (3)

$$v_s(t) = \frac{4V_g}{\pi} \cdot \sum_{n=1,3,5,\dots}^{\infty} \frac{1}{n} \sin(2\pi n f_s t) \quad (2.1)$$

and the fundamental component can be expressed as

$$v_{s1}(t) = \frac{4V_g}{\pi} \cdot \sum_{n=1,3,5,\dots}^{\infty} \frac{1}{n} \sin(2\pi n f_s t) = V_{s1} \sin(\omega_s t) \quad (2.2)$$

where t expresses the time, and n is an odd integer number. Now that the output is modeled as a sinusoidal voltage generator, the model of the converter dc input port can follow. Let's define I_g as the DC component of the switch current i_g . Depending on the position of the switch, $i_g(t)$ equals $i_s(t)$ or $i_g(t) = -i_s(t)$. Then

$$i_s(t) \simeq I_{s1} \sin(2\pi f_s t - \varphi_s) \quad (2.3)$$

where I_{s1} is the current peak and φ_s the phase. Taking the average of $i_g(t)$ over half-switching period:

$$\langle i_g(t) \rangle_{T_s} = \frac{2}{T_s} \int_0^{T_s/2} i_g(t) dt \simeq \frac{2}{T_s} \int_0^{T_s/2} I_{s1} \sin(2\pi f_s t - \varphi_s) dt = \frac{2}{\pi} I_{s1} \cos(\varphi_s) \quad (2.4)$$

In Figure 9(a),(b) (3) the waveforms of $v_s(t)$, $v_{s1}(t)$, $i_s(t)$, and $i_g(t)$ are illustrated, while Figure 10 (3) shows the built model after FHA.

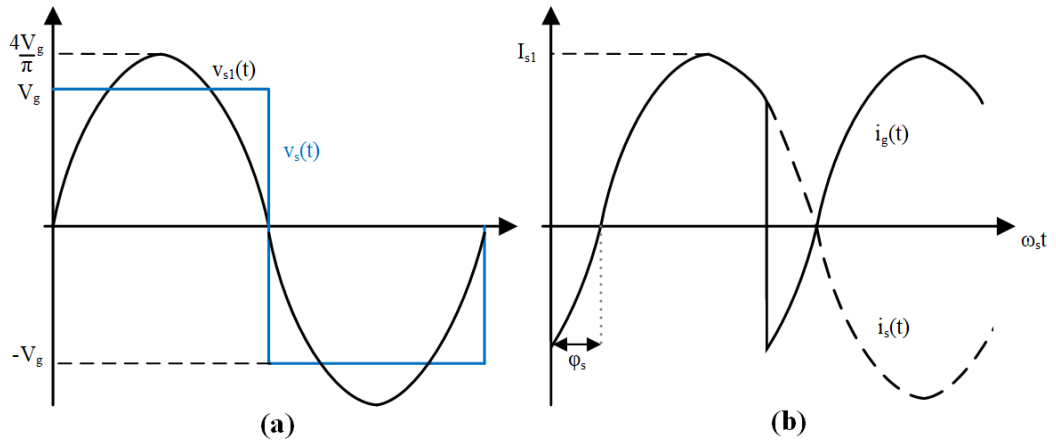


Figure 9: Waveforms of $v_s(t)$, $v_{s1}(t)$, $i_s(t)$, and $i_g(t)$. (a) Voltage waveforms, (b) current waveforms (3)

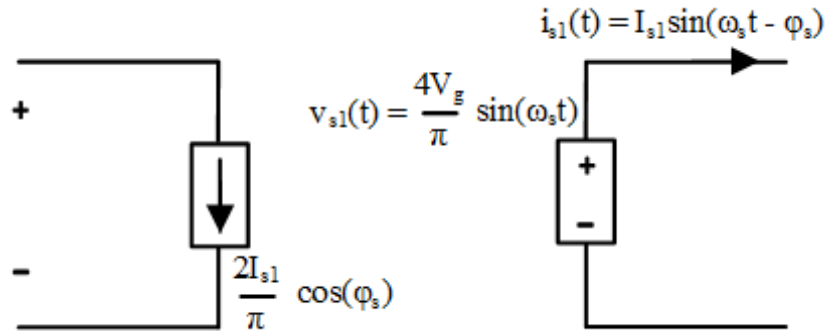


Figure 10: Equivalent model after FHA (3)

Now, we can consider the input rectifier with resonant tank, and DC load in Figure 7. Where the current $i_r(t)$ drives the rectifier, and a large filter capacitor C_f at the output makes valid the small-ripple approximation resulting in $v(t) \simeq V$ and $i(t) \simeq I$ (since $v(t)$ harmonics can be neglected). The waveforms of $v_R(t)$, $i_R(t)$, $v_{R1}(t)$, and $i_{R1}(t)$ are given in Figure 11 (3).

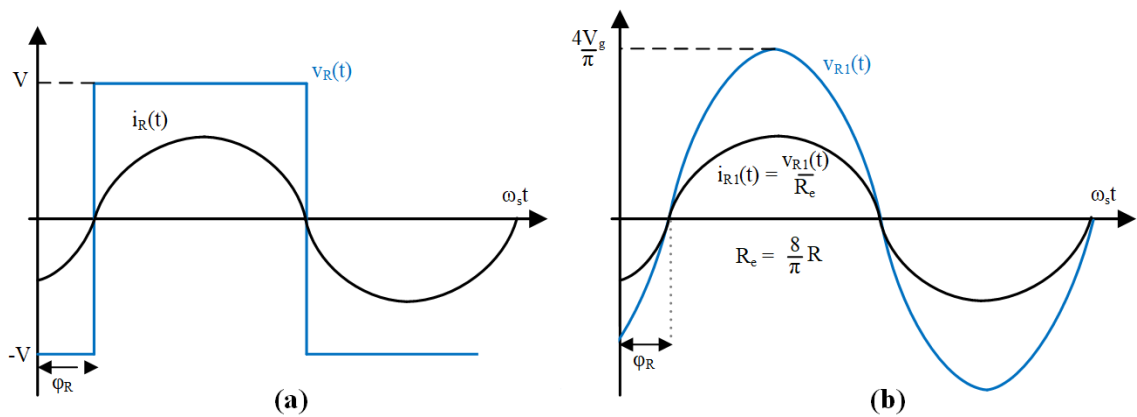


Figure 11: Waveforms of interest for rectifier network. (a) Real waveforms v_R , and i_R , (b) fundamental components v_{R1} , and i_{R1} (3)

Now, the tank output current i_R is defined as

$$i_R(t) = I_{R1} \sin(2\pi f_s t - \varphi_R) \quad (2.5)$$

and the rectifier input voltage in the Fourier series follows

$$v_R(t) = \frac{4V}{\pi} \cdot \sum_{n=1,3,5,\dots}^{\infty} \frac{1}{n} \sin(2\pi n f_s t - \varphi_R) \quad (2.6)$$

where φ_R represents the phase shift. And its fundamental component

$$v_{R1}(t) = \frac{4V}{\pi} \sin(2\pi f_s t - \varphi_R) \quad (2.7)$$

Since $V_{R1}(t)$ and $i_R(t)$ are in phase, the equivalent output resistance R_{eq} , is computed as follows:

$$R_{eq} = \frac{v_{R1}(t)}{i_R(t)} = \frac{8}{\pi^2} \frac{V}{I} = \frac{8}{\pi^2} R \quad (2.8)$$

that damps the tank network. Finally, the model including the input rectifier with resonant network and DC load is illustrated in Figure 12 (3).

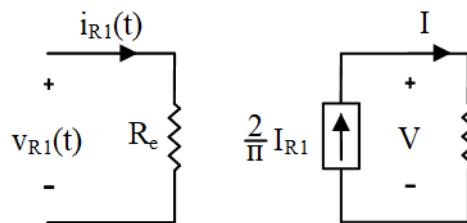


Figure 12: Equivalent circuit for input rectifier with resonant tank, and DC load (3)

2.2.3 CLLC Converter

Resonant-type DC-DC converters are currently under investigation for a wide range of voltage applications. They do not need clamp or snubber circuits (29). They are known for their high frequency operation, outstanding efficiency, minimal electromagnetic interference, and fewer components. Resonant converters are more efficient for low loads and equally efficient for high power transfer compared to phase-shifted DAB (29; 38).

The LLC DC-DC converter has become widely used in EV chargers due to its advantages such as output voltage regulation at light load, ZVS over a broad voltage range, ZCS for rectifier diodes, and simple output filtering (39; 40). It operates in three modes based on the

switching and resonant frequencies, providing optimized performance at resonant frequency, buck operation when the switching frequency is above resonance, and boost operation when it is below. Bidirectional power flow is crucial for V2G applications, enabling excess energy from the EV battery to be fed into the grid. However, bidirectional operation is challenging due to the asymmetrical resonant tank in LLC converters (1).

Solutions include using CLLC converters with additional capacitors for symmetry, ensuring similar characteristics in both modes (41; 8) , and employing adjustable DC link voltage to maintain efficiency. Enhancements like CLLC designs improve bidirectional operation and power density. This topology offers several advantages over conventional converters, such as reduced switching losses, improved voltage regulation, and enhanced power density. The CLLC converter is symmetrical and provides similar voltage gain characteristics in both power flow directions. This makes it less complex to control and results in lower leakage inductance (21). Furthermore, lower leakage inductance value results in lower reactive power with respect to DAB converter topology (21). However, the CLLC converter also faces some challenges. It needs to achieve Zero Voltage Switching (ZVS) and high efficiency when dealing with a wide voltage range (42), and it requires precise control to operate effectively (43). Several studies have contributed to the advancement of bidirectional CLLC resonant converters for EV charging applications. Research efforts have increasingly focused on enhancing both efficiency and power density. This includes the adoption of synchronous rectification (44), leveraging wide-bandgap devices (45), and optimizing operating frequency ranges. Additionally, the integration of auxiliary transformers has been explored for Zero-Voltage Switching (ZVS) realization (46), alongside the

development of parameter design methodologies for robust power regulation (47). The inclusion of integrated magnetic components is another strategy aimed at improving power density (48). Moreover, innovations such as snubberless operation (43) and optimized switching transitions (49) have further advanced the performance and reliability of bidirectional CLLC converters. These improvements make them well-suited for the demanding EV charging environments (4).

TABLE II: BIDIRECTIONAL DC-DC CONVERTERS IN LITERATURE (1)

Converter	Maximum Power (kW)	Switching Mode	Switching Frequency (kHz)	Efficiency [%]
DAB Dual voltage-fed	30	Hard	20	-
Half-full-bridge LLC resonant	10	Soft	90-150	≥ 96 (G2V), ≥ 98 (V2G)
Half-bridge CLLC resonant	3.3	Soft	100-200	97.5 (G2V), 97.3 (V2G)
Full-bridge PWM-RC	6.6	Soft	50	97.7 (G2V), 97.3 (V2G)
Full-bridge CLLC resonant	3.5	Soft	85-145 (G2V), 40-110 (V2G)	97.7 (G2V), 98.1 (V2G)

Table II (1) presents a comparison of isolated bidirectional DC-DC converters as reported in (29). It categorizes the converters based on their topology, maximum power, switching mode,

switching frequency, and efficiency. The first converter listed is the DAB Dual voltage-fed (50), which has a maximum power of 30kW and employs hard-switching at a frequency of 20kHz. However, no efficiency data is provided for this converter, which is used as a Level 2 charger.

Next, the Half-full-bridge LLC resonant (51) converter supports up to 10 kW of power, uses soft switching, and operates within a frequency range of 90 – 150kHz. This converter boasts efficiencies greater than 96% for grid-to-vehicle (G2V) and greater than 98% for vehicle-to-grid (V2G) operations, and it is also used as a Level 2 charger.

The Half-bridge CLLC resonant (52) converter has a maximum power of 3.3kW, employs soft switching, and operates within a frequency range of 100 – 200kHz. Its efficiency is 97.5% for G2V and 97.3% for V2G, making it suitable as a Level 1 charger.

The Full-bridge PWM-RC (53) converter handles up to 6.6kW, uses soft switching at a frequency of 50kHz, and has efficiencies of 97.7% for G2V and 97.3% for V2G. This converter is used as a Level 2 charger.

Finally, the Full-bridge CLLC resonant (54) converter has a maximum power capacity of 3.5 kW and employs soft switching. It operates at frequencies ranging from 85 – 145kHz for G2V and 40 – 110kHz for V2G, with efficiencies of 97.7% and 98.1% respectively. This converter is used as a Level 1 charger.

Overall, this detailed comparison highlights the performance and application of various isolated bidirectional DC-DC converters, aiding in the selection of appropriate technology for specific charging needs.

2.2.3.1 Control of CLLC Converter

Pulse frequency modulation (PFM) is the most common control strategy adopted for resonant converters (55). This applies also to the CLLC converter, where the output voltage regulation depends on the impedance of the resonant tank. The impedance characteristics of the resonant tank change with the operating frequency, which in turn affects the regulation of the output voltage. By the way, when a wide input or output voltage is required, the operating frequency interval must be wide as well. This might result in a more complicated design of magnetic components, loss of soft switching operation, and high electromagnetic interference (EMI). Furthermore, very high frequency may lead the converter to instability, particularly for no-load condition (2; 56).

Modulation strategies, such as phase-shift modulation (PSM), pulse width modulation (PWM), and resonant frequency modulation (RFM), are implemented to narrow the operating frequency range or set it as fixed (55). In primary-side phase-shift modulation (PSPSM) (57; 58; 59), adjusting the phase-shift angle between two switching legs allows for the regulation of the resonant tank's input voltage, ultimately controlling the output voltage. While PSM is capable of regulating the output voltage across a broad spectrum, achieving ZVS for the lagging-leg switches poses a challenge, limiting the range of voltage that can be effectively controlled. Furthermore, an enhancement to PSPSM is the introduction of secondary-side PSM (60) (SSPSM), which involves substituting the two bottom full-bridge rectifier diodes with MOSFETs. This modification enables the regulation of output voltage by adjusting the phase-shift angle on the secondary side.

Another method to maintain a fixed frequency operation involves using pulse width modulation (PWM). With primary-side PWM (PSPWM), to regulate the output voltage, the duty cycle of a supplementary bidirectional switch is changed. This adjustment can transform the system's configuration into a half-bridge structure (61; 56). Similarly, secondary-side PWM (SSPWM) (62) controls the output voltage by modulating the duty cycle of the new supplementary switch on the secondary side to create a voltage doubler rectifier (62; 56; 55).

Besides PSM and PWM, resonant frequency modulation (RFM) (56) offers another route to fixed frequency operation. RFM's core principle for output voltage control lies in the management of the normalized switching frequency. Maintaining a constant switching frequency allows for the adjustment of the resonant frequency, thereby altering the normalized switching frequency and, consequently, the output voltage.

The traditional modulation strategies mentioned above adopted for resonant converters are reported in Figure 13 (60; 61; 62), including their control schemes and circuits.

In (56), an overview of the modulation strategies, with particular insight about hybrid modulation, is described. In (63), an advanced control scheme known as optimized extended phase shift (EPS), also termed dual phase shift control in (64), is introduced. This method regulates voltage by modifying the amplitude of the primary side's square wave voltage, enabling high-efficiency operation particularly under light loads. Conversely, (65) presents an asymmetric PWM control on the primary side designed to enhance light load efficiency, though its capability is confined to step-down regulation at the resonant frequency. Similarly, (66) explores the synchronized PWM control of CLLLC, detailing its operational framework and power transfer

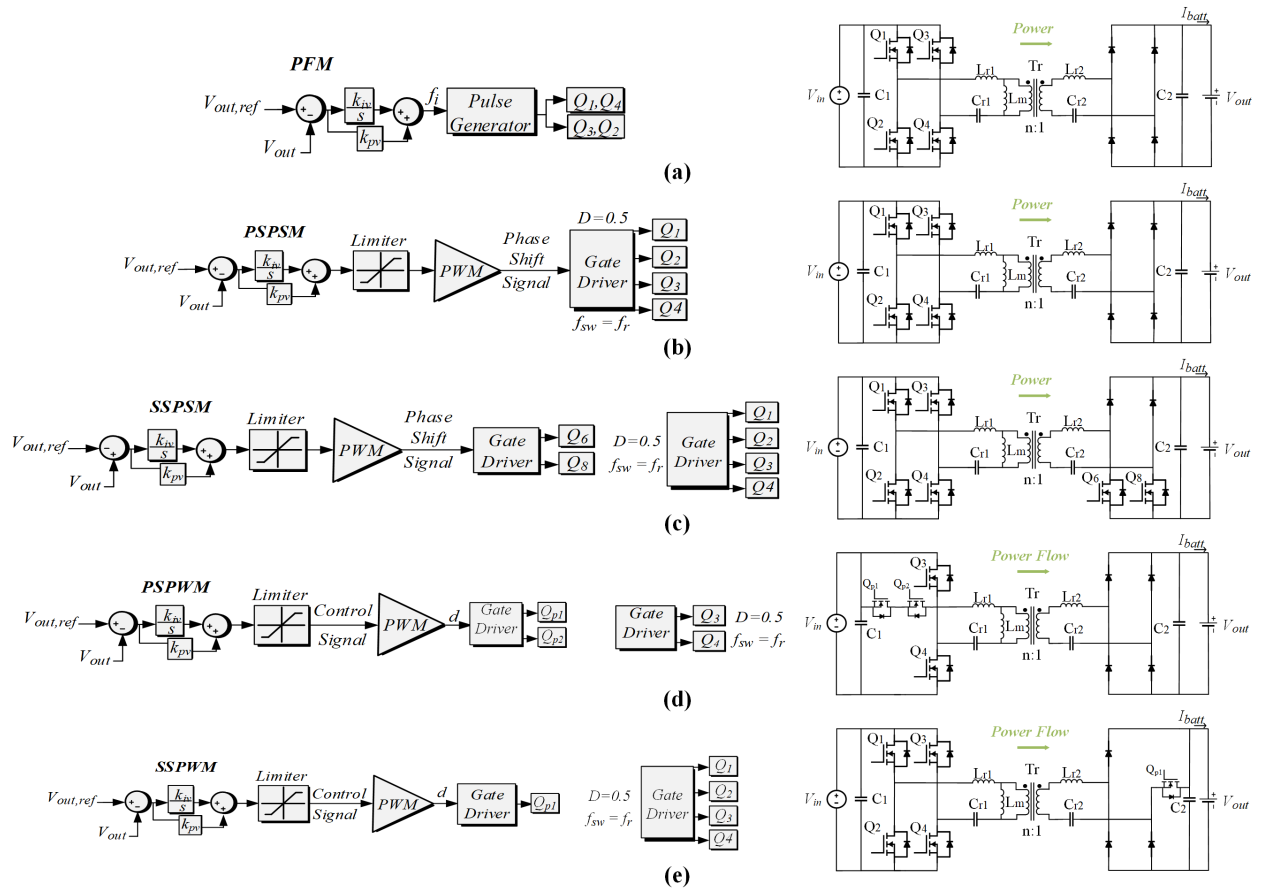


Figure 13: Traditional Modulation Strategies for CLLC Converter Control. (a) Pulse Frequency Modulation (PFM), (b) Primary-Side Phase-Shift Modulation (PPSM), (c) Secondary-Side Phase-Shift Modulation (SSPSM), (d) Primary-Side Pulse Width Modulation (PSPWM), (e) Secondary-Side Pulse Width Modulation (SSPWM)

features. At their core, (63; 65; 66) share a methodological approach of voltage adjustment through alterations in the fundamental voltage amplitude, utilizing in-phase control on both the primary and secondary sides. In (67), PFM is merged with phase shift control across the primary and secondary sides, analyzing how this affects both the active and reactive power,

along with the phase shift angle. This strategy notably expands the ZVS range and reduces reactive power. In a different approach outlined in (68), a unique primary asymmetric duty cycle control for LLC stands out, offering an alternative to PSAPWM as it acts as a frequency multiplier of switching, effectively halving the actual switching frequency to enhance efficiency. Given that single-output CLLC converters cannot simultaneously offer multiple voltage levels, controlling multi-port converters has emerged as a significant yet underexplored area. Typically, the integration of various distinct modulation strategies offers improved control outcomes. As illustrated in (69), a hybrid modulation combining PFM and PWM is employed for the three-port bidirectional CLLC in car charging applications, uniquely integrating the secondary side of CLLC with an interleaved bidirectional boost and buck circuit, enhancing both power rating and output stability while maintaining ZVS for all switches. The application of PFM+PSM modulation to a three-port bidirectional CLLC within a small home microgrid, as discussed in (70), aims for optimal efficiency and addresses the limitations associated with phase shift control under such configurations. In Table III, the most attractive hybrid modulation techniques are reported (2). All of them showing a wide voltage gain range and multiport capability.

TABLE III: HYBRID MODULATION STRATEGIES (2)

Control Strategy	ZVS (ps)/ZCS (ss)	Control Complexity	Switching Frequency
PSAPWM + SSAPWM	Yes/Yes	Simple	Fixed
PSM + PFM	Yes/No	Moderate	Narrow Range
PSPSM + SSPSM	Yes/Yes	Moderate	Fixed
PSSPWM + SSSPWM	Yes/Yes	Complicate	Fixed

2.3 From Grid-Following to Grid-Forming Inverters

The increasing penetration of power-electronic-interfaced energy sources, such as renewables and energy storage systems, is surpassing the use of conventional synchronous generators (71). This shift challenges current grid management strategies, which rely on power electronic converter controls to replicate inertial response and maintain stable grid frequency and voltage (71). In modern power systems, power electronic converters are critical. They serve as the interface between the grid and various distributed energy sources, enabling the integration of renewables, storage systems, and electric motors (72; 73). However, these converters typically operate as either AC voltage or current sources, limiting their effectiveness in grid stabilization (72; 73).

2.3.1 Grid-Following

Grid-following converters have been essential in integrating power into the grid by relying on a stable grid voltage for proper functionality. These converters use a phase-locked loop (PLL) mechanism to align with the grid's frequency, operating as current-controlled units that modulate power output to match the grid's flow, behaving as sinusoidal current sources (71; 73). However, with the increasing share of renewable energy sources (RESs), the assumption of a stiff and stable grid voltage is being challenged. Inverter-based generation, primarily using grid-following inverters, depends on the voltage provided by synchronous machines. This dependence poses risks during blackouts or islanding situations, where these inverters cannot autonomously support or restore the grid. These limitations underscore the inadequacy of current grid-following technologies in adapting to a system dominated by RESs, raising concerns

about their effectiveness in a future with minimal traditional synchronous generators (74; 75). Existing systems, equipped with outer-loop synchronizing units such as PLLs, may not suffice in a heavily inverter-interfaced grid due to the lack of voltage regulation capability inherent in grid-following converters (71; 75). Designed to follow rather than dictate grid dynamics, grid-following inverters struggle in scenarios where they must lead in voltage and frequency regulation, a situation increasingly likely (74; 75). This evolving scenario highlights the urgent need for advancements in converter technology. Moving beyond current grid-following models is essential to ensure stability, reliability, and autonomy in future power systems.

2.3.2 Grid-Forming

Considering the growing complexity and evolving nature of modern power systems, grid-forming inverters are emerging as a cornerstone for the future of electricity generation and distribution. Unlike traditional grid-following models, grid-forming inverters function as voltage sources, integrating seamlessly into the grid regardless of its state (71). This approach inherently controls the system's voltage and frequency, eliminating the need for phase-locked loops (PLLs) and enabling smooth transitions between grid-tied and islanded operations (76). Grid-forming controls are especially important in systems heavily reliant on converter-interfaced energy storage. They can uniquely manage active and reactive power flow based on the grid's impedance characteristics (74). This capability is crucial for grids with predominantly resistive or inductive impedance. The stability and performance of these inverters are significantly influenced by the grid's impedance, necessitating a deep understanding of these characteristics (77; 78; 79). As power systems evolve, there is a clear need for advanced grid-forming inverters

capable of maintaining system voltage and frequency autonomously. This represents a pivotal shift toward systems managed primarily by inverter-based resources (75). The widespread deployment of RESs calls for decentralized control mechanisms that ensure resilience without relying on rapid, communication-dependent actions or traditional synchronous machines. Droop control remains a fundamental grid-forming strategy. Using voltage source inverters and their respective output impedances, power control can be achieved by adjusting the voltage magnitude and angle, also known as angle droop and frequency droop controls. The droop characteristics for the amplitude and frequency of the inverter output voltage are represented by typical droop curves of active power (P) vs frequency (ω) and reactive power (Q) vs voltage (V). The droop control mechanism ensures the synchronization of phase angles between the inverter voltage and the grid voltage (80; 81) as in Figure 14(b).

Nevertheless, its slower transient response has led to the exploration of virtual synchronous machines and virtual inertia methods (74). These innovative approaches emulate the dynamic responses of traditional generators, offering rapid response capabilities crucial for the stability and reliability of future low-inertia grids. The direct emulation of the synchronous machine is a simple way to give inverters grid-forming capabilities. These algorithms vary for the emulation level and the current and voltage controls implemented. By the way, an equation that describes the electromechanical effect in the form of the swing equation (80; 81) as in Figure 14(a) is commonly included.

Furthermore, novel control methodologies inspired by nonlinear oscillator dynamics promise for achieving high responsiveness and stability in zero-inertia, inverter-based systems. The

virtual oscillator control (VOC) is different from the methods cited earlier because it is a sinusoidal time domain implementation connected to the synchronization principle of oscillators that couple in complex networks (80). This method utilizes a Van der Pol oscillator with a non-linear differential equation to create the virtual oscillator. Only the output current is used as a feedback parameter, which is then employed to drive the virtual oscillator circuit (80; 81) as in Figure 14(c).

Acknowledging the foundational role of synchronous generators in stabilizing grid operations through traditional controls is imperative (75). As we transition to a future dominated by inverter-based systems, grid-forming controls aim to replicate and enhance these traditional functions, ensuring the smooth integration of renewable energy sources and battery storage into the grid, thereby enhancing grid stability and resilience. The ongoing refinement of standards, such as IEEE Standard 1547, underscores the industry's commitment to developing grid-forming controls that adapt to the evolving power systems landscape, ensuring their relevance and effectiveness for years to come (75).

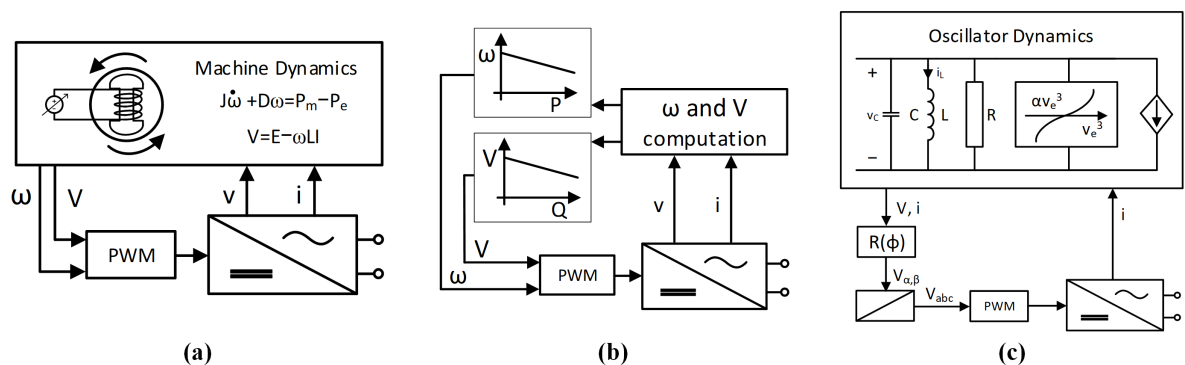


Figure 14: Grid-Forming Inverter Control Strategy. (a) Virtual Synchronous Machine Emulation, (b) Voltage and Frequency Regulation based on Droop Control, (c) Virtual Oscillator Control (VOC)

CHAPTER 3

CLLC CONVERTER ANALYSIS AND DESIGN

3.1 Introduction

Major parts of the results and discussions in this thesis chapter are derived from my paper accepted for publication at IEEE IECON 2024 (4). The CLLC Converter in Figure 15 is a Full-Bridge bidirectional converter. In G2V mode, it operates as charging mode for the battery, while in the reverse power flow, it operates in V2G mode, and the battery is consequently discharged. The grid side of the converter is located on the left side, and the battery is located on the right side. The resonant tank is formed by the inductances L_{r1} and L_{r2} that are the leakage inductances, L_m is the magnetizing inductance, C_{r1} and C_{r2} are the resonant capacitors. Instead, C_1 and C_2 are the filter output capacitors, and their main role is to filter out the voltage ripple in the output (4).

3.2 Voltage Gain Analysis

Major parts of the results and discussions in this thesis chapter are derived from my paper accepted for publication at IEEE IECON 2024 (4).

3.2.1 First-Harmonic-Approximation

The First Harmonic Approximation (FHA) is needed to retrieve the equivalent circuits of the resonant converter for both operations (82). In this way, the gain expressions will be more easily expressed. Starting from the voltage at the input of the resonant converter, the Fourier

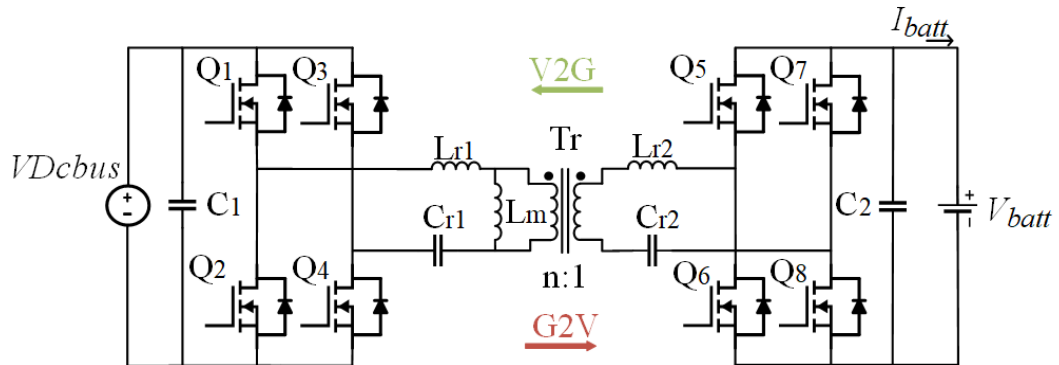


Figure 15: CLLC Resonant Converter Circuit

series can be used to define v_i (where the input voltage corresponds to the voltage DC Bus V_{DCbus} , while the output voltage to the battery voltage V_{batt}). Its formulation follows below (82):

$$v_i(t) = \frac{4V_{in}}{\pi} \cdot \sum_{n=1,3,5,\dots}^{\infty} \frac{1}{n} \sin(2\pi n f_s t) \quad (3.1)$$

where t expresses the time, n is an odd integer number, and f_s is the switching frequency of the power MOSFET. After that, the fundamental component can be computed with the following expression (82):

$$v_{i,FHA}(t) = \frac{4}{\pi} V_{in} \sin(2\pi f_s t) \quad (3.2)$$

The same procedure might be followed to express the output voltage of the resonant network (82):

$$v_o(t) = \frac{4V_o}{\pi} \cdot \sum_{n=1,3,5,\dots}^{\infty} \frac{1}{n} \sin(2\pi n f_s t - \varphi) \quad (3.3)$$

where φ represents the phase shift. And its fundamental component (82)

$$v_{o,\text{FHA}}(t) = \frac{4}{\pi} V_o \sin(2\pi f_s t - \varphi) \quad (3.4)$$

For computing the equivalent output resistance $R_{o,\text{eq}}$, also the rms value is needed (82):

$$V_{o,\text{FHA}} = \frac{2\sqrt{2}}{\pi} V_o \quad (3.5)$$

At this scope, the FHA current $i_{r,\text{FHA}}$ flowing through the rectifier circuit, is defined as (82):

$$i_{r,\text{FHA}}(t) = \sqrt{2} I_{r,\text{FHA}} \sin(2\pi f_s t - \varphi) \quad (3.6)$$

where $I_{\text{rms},\text{FHA}}$ defines the rms value of $I_{r,\text{FHA}}$ as follows (82):

$$I_{\text{rms},\text{FHA}} = \frac{2\sqrt{2}}{\pi} \int_0^{T_s/2} i_{r,\text{FHA}}(t) dt = \frac{2\sqrt{2} I_{r,\text{FHA}}}{\pi} \quad (3.7)$$

3.2.1.1 Forward Mode Equivalent Circuit

Finally, taking into account the transformer turn ratio, the expression for the equivalent output resistance $R_{o,\text{eq}}$ is (52; 82):

$$R_{o,\text{eq}} = \frac{V_{o,\text{FHA}}}{I_{r,\text{FHA}}} = \frac{8n^2}{\pi} R_o \quad (3.8)$$

where R_o is the load resistance in charging mode. Figure 16 shows the equivalent circuit for the G2V operation. In this mode, the equivalent inductance and capacitor can be computed as (52; 82):

$$L'_{r2} = n^2 L_{r2}, \quad C'_{r2} = \frac{C_{r2}}{n^2} \quad (3.9)$$

Therefore, the voltage gain for the G2V operation can be expressed as (83; 52; 82):

$$G_{g2v}(s) = \frac{1}{n} \cdot \frac{R_{o,eq}}{R_e + sL'_2 + \frac{1}{sC'_2}} \cdot \frac{R_{o,eq} + sL'_2 + \frac{1}{sC'_2}}{sL_1 + \frac{1}{sC_1} + \left(R_{o,eq} + sL_2 + \frac{1}{sC'_2} \right) \parallel sL_m} \quad (3.10)$$

Since the resulting input impedance and output impedance are defined as (52; 82)

$$Z_1 = R_{o,eq} + sL'_2 + \frac{1}{sC'_2}, \quad Z_2 = sL_{r1} + \frac{1}{sC_{r1}} + Z_1 \parallel sL_m \quad (3.11)$$

The voltage gain in charging mode can be expressed more compactly as (52; 82)

$$G_{g2v}(s) = \frac{1}{n} \cdot \frac{R_{o,eq}}{Z_1} \cdot \frac{Z_1 \parallel sL_m}{Z_2} \quad (3.12)$$

Before introducing the module value of the voltage gain, some parameters must be introduced (52; 82):

$$\begin{aligned} h &= \frac{L_m}{L_{r1}}, \quad k = \frac{L'_2}{L_{r1}}, \quad g = \frac{C'_2}{C_1}, \quad \omega_n = \frac{\omega_s}{\omega_{r1}}, \quad \omega_r = \frac{1}{\sqrt{L_{r1}C_1}}, \quad Q = \frac{\sqrt{\frac{L_{r1}}{C_1}}}{R_{o,eq}}, \\ a &= \frac{1}{h} + 1 - \frac{1}{h\omega_n^2}, \quad b = \left(\frac{k}{h} + 1 + \frac{1}{g \cdot h} + \frac{1}{g} \right) \cdot \frac{Q}{\omega_n} - \left(\frac{k}{h} + 1 + k \right) \cdot \omega_n Q - \frac{Q}{g \cdot h \cdot \omega_n^3} \end{aligned} \quad (3.13)$$

where the quality factor is defined by Q . Now, since we desire to have the same resonant frequency of primary and secondary side fixed at the same value $f_{r1} = f_{r2}$, and at the same time simplify the design procedure, we set $L_{r1} = L'_{r2}$ and $C_{r1} = C'_{r2}$, so that $k = 1$, and $g = 1$ (84; 82). Then, the module of the gain can be expressed as (4; 82; 52)

$$|G(s)|_{g2v} = \frac{1}{n\sqrt{a^2 + b^2}} \quad (3.14)$$

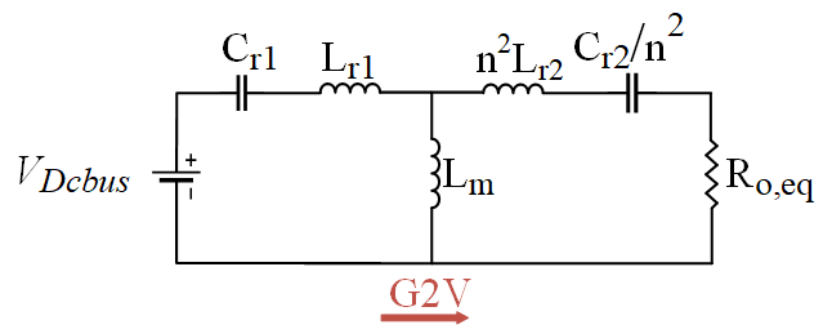


Figure 16: Equivalent Circuit in G2V Mode

3.2.1.2 Reverse Mode Equivalent Circuit

The equivalent load, the leakage and magnetizing inductances, and the resonant capacitor are computed as (82; 52):

$$R'_{o,eq} = \frac{8}{n^2\pi} R_o, \quad L'_1 = \frac{L_{r1}}{n^2}, \quad L'_m = \frac{L_m}{n^2}, \quad C'_{r1} = n^2 C_{r1} \quad (3.15)$$

Then, similarly as before, the required parameters are derived as follows (82; 52):

$$\begin{aligned}
 h' &= \frac{L'_m}{L_{r2}}, \quad k = \frac{L'_1}{L_{r2}}, \quad g = \frac{C'_1}{C_2}, \quad \omega'_n = \frac{\omega_s}{\omega_{r2}}, \\
 \omega_{r2} &= \frac{1}{\sqrt{L_{r2}C_{r2}}}, \quad Q' = \frac{\sqrt{\frac{L_{r2}}{C_{r2}}}}{R'_{o,eq}}, \quad c = \frac{1}{h'} + 1 - \frac{1}{h'\omega_n'^2}, \\
 d &= \left(\frac{k'}{h'} + 1 + \frac{1}{g' \cdot h'} + \frac{1}{g'} \right) \cdot \frac{Q'}{\omega_n'} - \left(\frac{k'}{h'} + 1 + k' \right) \cdot \omega_n' Q' - \frac{Q'}{g' \cdot h' \cdot \omega_n'^3}
 \end{aligned} \tag{3.16}$$

Now, the module of the gain in the reverse mode can be formulated as follows (82; 52)

$$|G(s)|_{v2g} = \frac{n}{\sqrt{c^2 + d^2}} \tag{3.17}$$

Finally, in Figure 17 the equivalent circuit for the V2G operations is displayed (4).

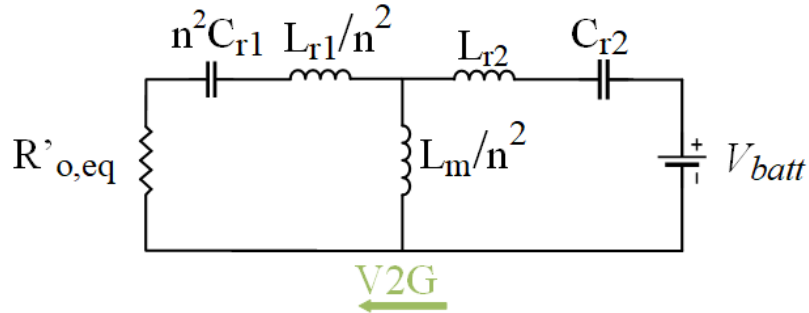


Figure 17: Equivalent Circuit in V2G Mode

3.3 Operating Principles

Major parts of the results and discussions in this thesis chapter are derived from my paper accepted for publication at IEEE IECON 2024 (4). The six stages of operation for a bidirectional CLLC resonant converter within a single switching cycle are illustrated in Figure 18 (85).

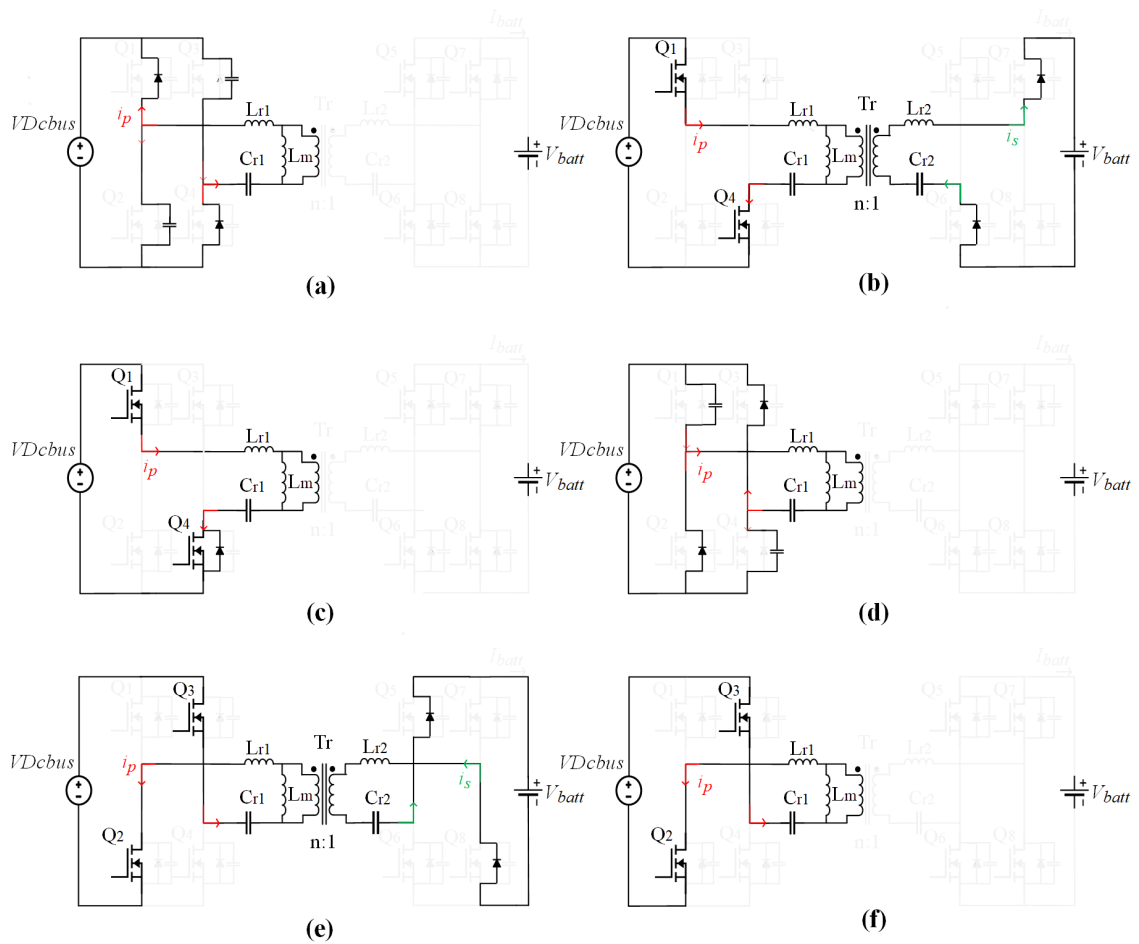


Figure 18: CLLC converter operating modes for G2V direction. (a) 1st Mode (t_1-t_2), (b) 2nd Mode (t_2-t_3), (c) 3rd Mode (t_3-t_4), (d) 4th Mode (t_4-t_5), (e) 5th Mode (t_5-t_6), (f) 6th Mode (t_6-t_7),

The first three stages are identical to the ones from the fourth to the sixth, with the only difference being the mosfets and diode couples involved in the process. Notably, Modes 1 and 4 have dead-time intervals, while Modes 2 and 5 are characterized by resonance and power transmission. Modes 3 and 6, however, occur outside of resonance. During the power transfer from the primary side to the secondary side, the switches Q_1 and Q_4 are ON and the secondary switches are deactivated, thus acting as rectifiers in a rectifying mode (85).

Figure 19 illustrates the theoretical waveforms of the converter through every stage within a single switching interval when it is in generating mode below resonance frequency.

The modes operate as detailed below (85):

1. 1st Mode ($t_1 - t_2$): This initial mode is characterized by a pause in power transfer to the secondary rectification stage. During this period, the primary current is engaged in charging the output capacitance of switches Q_2 and Q_3 , and discharging that of Q_1 and Q_4 . Subsequently, the primary current passes through the anti-parallel diode of Q_1 and Q_4 , facilitating ZVS for these switches (85).
2. 2nd Mode ($t_2 - t_3$): In this phase, Q_1 and Q_4 become active, facilitating the transfer of power to the secondary stage of rectification through the transformer. This leads to a shift in the primary current towards a positive direction, a change that is influenced by the activation of Q_1 and Q_4 and driven by the input voltage, V_{in} . Throughout this stage, the output voltage on the secondary side impacts the transformer, causing a gradual rise in the magnetic energy within the magnetizing inductance, L_m . Consequently, during this

phase, the resonance of the primary stage does not involve L_m , marking its exclusion (85).

After defining the primary current at t_2 , Δ , and ω_r as (85)

$$i_p(t_2) \approx -\frac{V_{in}}{L_m + L_r} \left(\frac{T_s}{4} - \frac{\Delta}{2} \right), \quad \Delta = t_4 - t_3 = t_7 - t_6, \quad \omega_r = 2\pi f_r, \quad Z_r = \sqrt{\frac{L_r}{C_r}} \quad (3.18)$$

where T_s expresses the switching period, and $\Delta = 0$ at resonant frequency. The primary current i_p , with the assumption that the dead-time can be neglected, follows (85)

$$i_p(t) = i_p(t_2) \cos \omega_r(t-t_2) + \frac{V_{in} - V_{Cr1}(t_2)}{Z_r} \sin \omega_r(t-t_2) - \int_{t_2}^t V_T(t-\tau) \cos \omega_r \tau \, d\tau \quad (3.19)$$

where the voltage across the primary resonant capacitor and the transformer are respectively V_{Cr1} and V_T . Since $i_p(t_2) = i_m(t_2)$ holds, the magnetizing current is defined as (85)

$$i_m(t) = i_m(t_2) + \frac{1}{L_m + L_r} \left[V_{in}(t-t_2) - \int_{t_2}^t V_{Cr1}(\tau) \, d\tau \right] \quad (3.20)$$

The transition between the 2nd and 3rd Mode (from resonant to non-resonant stage) is determined when i_p and i_m meet (85).

3. 3rd Mode (t_3-t_4): Here, no power is transmitted to the secondary side, rendering the secondary current i_s effectively zero, which consequently can't charge the output capacitor. The primary and the magnetizing currents equalize, and i_m keeps increasing until Q_1 and Q_4 are deactivated. At this stage, the output side is disconnected from the primary

side. Within the 3r Stage, the primary current i_p aligns with the magnetizing current i_m , thanks to a sufficiently large magnetizing inductance that mitigates the resonance effect (85). If it doesn't hold, i_p can be expressed as (85)

$$i_p(t) = i_p(t_3) \cos \omega_m(t - t_3) + \frac{V_{in} - V_{Cr1}(t_3)}{Z_m} \sin \omega_m(t - t_3) \quad (3.21)$$

where $\omega_m = \frac{1}{\sqrt{(L_m + L_r)C_r}}$ and $Z_m = \sqrt{\frac{L_m + L_r}{C_r}}$.

4. 4th Mode (t_4 - t_5): In this mode, a dead-time period with the switch pair of Q_2 and Q_3 is involved. It introduces a variation in the charging and discharging capacities of the switch pair, which differs from those in the 1st Stage. This mode enables the primary current to flow through the antiparallel diode of Q_2 and Q_3 , allowing these switches to activate under ZVS conditions (85).
5. 5th Mode (t_5 - t_6): The activation of Q_2 and Q_3 initiates the power transfer from the primary side to the secondary side of the converter. This mode prompts a directional change in the current, i_p , mirroring the behavior observed in the 2nd stage. Essentially, the 5th mode operates identically to the 2nd one, but utilizes a different set of switches Q_2 and Q_3 . Then, since $i_p(t_2) = i_p(t_5)$ (85)

$$i_p(t) = i_p(t_5) \cos \omega_r(t - t_5) - \frac{V_{in} - V_{Cr1}(t_5)}{Z_r} \sin \omega_r(t - t_5) - \int_{t_5}^t V_T(t - \tau) \cos \omega_r \tau d\tau \quad (3.22)$$

while given $i_p(t_5) = i_m(t_5)$, the magnetizing current i_m can be obtained as (85)

$$i_m(t) = i_m(t_5) - \frac{1}{L_m + L_r} \left[V_{in}(t - t_5) + \int_{t_5}^t V_{Cr1}(\tau) d\tau \right] \quad (3.23)$$

6. 6th Mode (t_6 - t_7): This mode is characterized by no power transfer and is outside of resonance, rendering the secondary current i_s effectively zero. ZCS is achieved when the mosfets Q_5 and Q_8 act as rectifiers. The expression for computing i_p follows (85)

$$i_p(t) = i_p(t_6) \cos \omega_m(t - t_6) - \frac{V_{in} + V_{Cr1}(t_5)}{Z_m} \sin \omega_m(t - t_6) \quad (3.24)$$

Figure 19 (86) shows the CLLC converter waveforms below the resonance frequency for each operation stage (85).

3.4 Design Procedure and Parameters Selection

Major parts of the results and discussions in this thesis chapter are derived from my paper accepted for publication at IEEE IECON 2024 (4).

3.4.1 Design Procedure

The design of the CLLC converter is described in this section. One of the design goals is to consider the operating conditions of the CLLC converter as they need to be connected together inside the charging station. In DC charging stations, the sudden arrival or departure of an electric vehicle can lead to abrupt changes in load, affecting the stability of the power converter at the designated charging station. This design procedure is finely crafted to meet this challenge

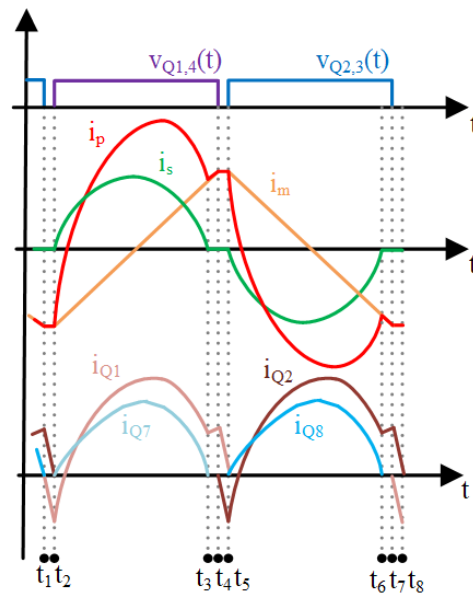


Figure 19: CLLC converter waveforms below resonance frequency

effectively. The converter is engineered to both charge and discharge within specific battery voltage ranges, accommodating every voltage value within the predefined interval of the DC bus. The central challenge in the design process is to maximize the battery voltage level during Grid-to-Vehicle (G2V) charging phases, while minimizing it throughout the Vehicle-to-Grid (V2G) discharging stages. It is imperative to maintain the operation of the converter in close proximity to its designated resonance frequency, since for seamless compatibility between the converter's design and its actual performance, FHA assumptions must be valid. This results in a narrow frequency band, which closely approaches the resonant frequency and consistently remains above it (87). Moreover, the proposed design procedure achieves ZVS and linear control under all load conditions with a clear simplified path that follows in Figure 20 (4).

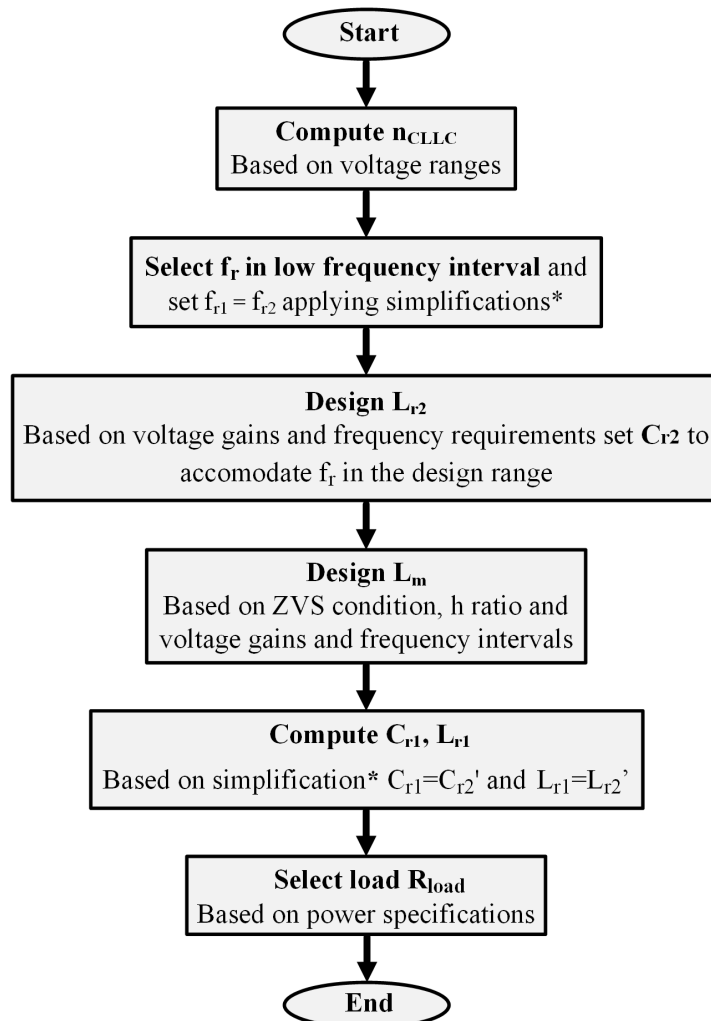


Figure 20: Flow Chart for design procedure (4)

1. The transformer ratio is defined here as the ratio between the maximum DC bus voltage V_{DCbus}^{V2Gmax} in the V2G direction and the minimum battery discharging level V_{batt}^{V2Gmax} , which corresponds to the maximum gain G_{v2g}^{max} in reverse mode. At this stage, It is important to choose n_{CLLC} in such a way that the ratio $\frac{C_{r2}}{C_{r1}}$ is as close as possible to 1. Therefore, the

design curve shape is preserved to avoid significant differences between the two operations (43).

2. When designing a CLLC resonant converter using FHA, it is recommended to opt for a low-frequency converter design, especially without exceeding 300 kHz range (88). Since it is desired the converter to work in a similar frequency interval for both directions (implying simplified resonant tank design and control complexity), it follows that $L_{r1} = L'_{r2}$ and $C_{r1} = C'_{r2}$. This results in the same resonant frequency $f_r = f_{r1} = f_{r2}$ for G2V and V2G operations. For $C_{r1} = C'_{r2}$ at lower capacitors values correspond lower frequency ranges, while without considering the assumption, lower capacitors values lead to higher frequency intervals, which is less suitable for our design scope. Figure 21 and Figure 22 show the impact of the above-mentioned assumption in both operations.

The secondary side resonant components selection can start by C_{r2} , which doesn't significantly affect the design curves in terms of voltage gains and switching frequency interval.

3. Selecting the right value for secondary side inductance L_{r2} is critical for optimizing design performance, particularly concerning switching frequency intervals as shown in Figure 23. This decision must account for system gain and frequency requirements while ensuring the inductance value is minimized appropriately.
4. The ZVS condition below defines the maximum magnetizing inductance value (85)

$$16L_m C_{oss} f_{smax} \leq T_{dead} \quad (3.25)$$

where C_{oss} is the Mosfet junction capacitor, f_{smax} defines the maximum operating frequency for the converter, while T_{dead} defines the dead time and is chosen to satisfy the following condition (43):

$$T_{dead} = t_{rise} + t_{fall} + t_{on} + t_{off} \quad (3.26)$$

with t_{rise} , t_{fall} , t_{on} , t_{off} parameters related to the mosfet.

The magnetizing inductance is then selected to satisfy both voltage gains and frequency range, such as condition (9). At this scope, the design curve under different values of the ratio L_m/L_{r1} must be analyzed. From Figure 24 and Figure 25, it can be observed that increasing values of h result in limited gain value and a wider operating frequency range (54). This phenomenon is more evident under lower load conditions. A suitable range for h spans from 3 to 5 (43).

5. The selection of the load resistance R_{load} depends mostly on the output power. Figure 26 (4) illustrates the design curves under varying load conditions. For both operations, the converter operates close and above the resonant frequency f_r (peaking at $1.2f_r$) in the decreasing monotonical behavior region of the curve, under all load conditions. In this way, the converter performs similarly to the design curves derived by the FHA, the converter can be controlled under linear control with a simple PI controller and ZVS condition are satisfied under all load conditions. The Quality factor (Q) significantly influences gain variations and the switching frequency range. Higher Q values are associated with in-

creased gain variations and a narrower switching frequency range. To simplify control and ensure the converter operates efficiently, it is important to avoid very narrow frequency intervals, which can cause the converter to work in the conductive region. The design should be adjusted if necessary to accommodate a higher maximum converter power. As illustrated in Figure 23, reducing the value of L_{r2} (and consequently increasing the resonant frequency) can flatten the curve and enable the converter to achieve higher power levels. This makes it more suitable for handling potential fast-charging or discharging requirements, as needed in DC parking lots. Lower Q values present reduced gain variations and an expanded frequency range (82).

In this way, the converter performs similarly to the design curves derived by the FHA, the converter can be controlled under linear control with a simple PI controller, and the ZVS condition is satisfied under all load conditions (4).

3.4.2 Design Parameters Choice

As mentioned above, FHA assumptions must be valid to ensure seamless compatibility between the converter's design and its actual performance (87). The outcome is a narrow frequency band, which closely approaches the resonant frequency and consistently remains above it. This validates the limited voltage ranges on both the DC Bus and battery side for all operations. Also, the operation of a DC microgrid makes it particularly challenging to define wider voltage ranges on both sides. Given the desired operation in the inductive region and the need for a monotonically decreasing behavior to ensure ZVS under any load, the transformer ratio must be selected to accommodate the battery voltage intervals of 326V – 360V for G2V

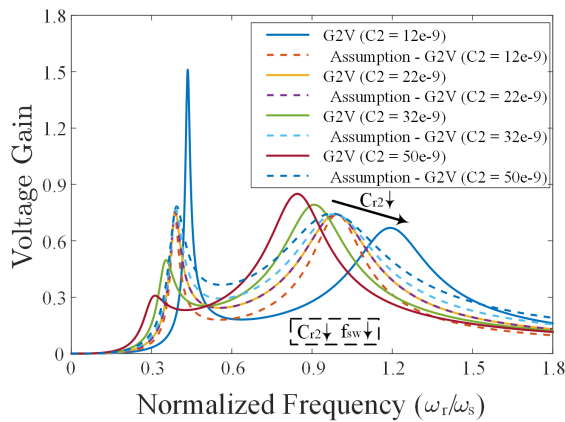


Figure 21: Variation of voltage gain with $C_{r1} = C'_{r2}$ and without it for charging mode for $R_{load} = 35\Omega$

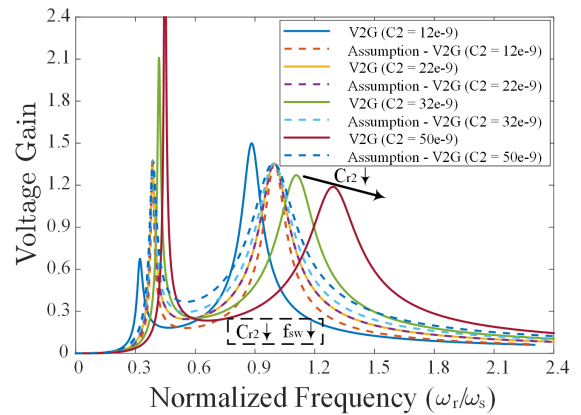


Figure 22: Variation of voltage gain with $C_{r1} = C'_{r2}$ and without it for discharging mode for $R_{load} = 35\Omega$

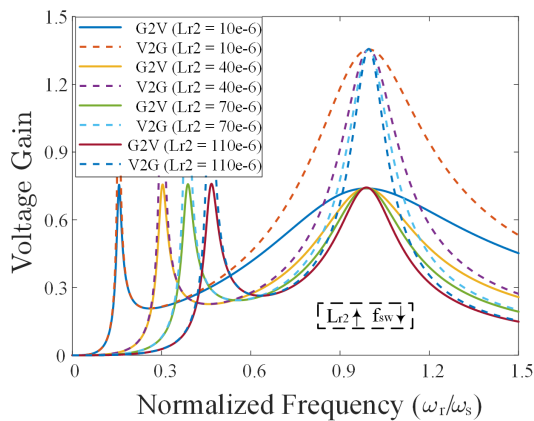


Figure 23: Voltage gain curve for different values of L_{r2} based on design simplification for $R_{load} = 35\Omega$

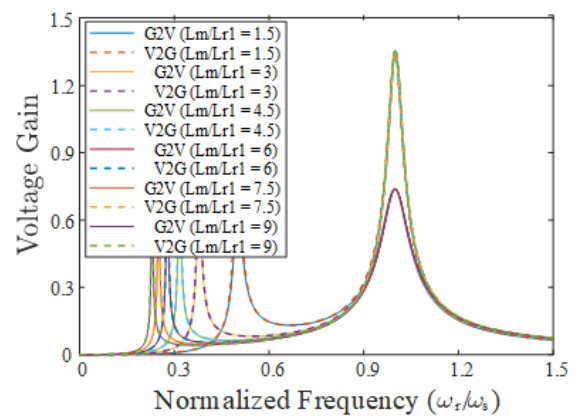


Figure 24: Voltage gain curve for different values of h for $R_{load} = 12\Omega$

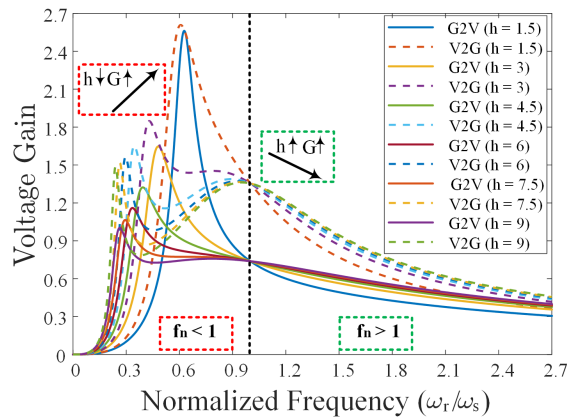


Figure 25: Voltage gain curve for different values of h for $R_{\text{load}} = 228\Omega$

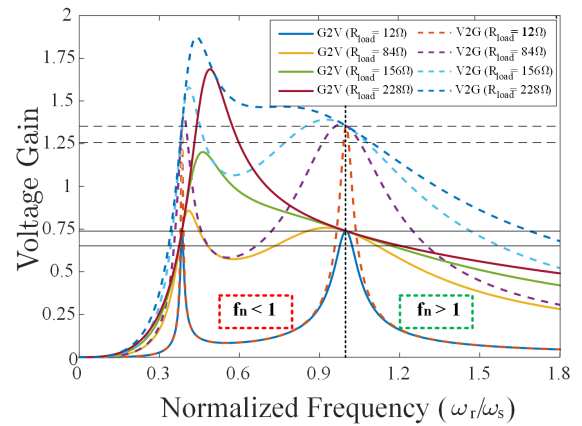


Figure 26: Voltage gain curve under different load conditions

and 379V–398V for V2G. Moreover, since this methodology justifies the minor DC bus voltage variation around the nominal voltage, set to 500V with a tolerance of $\pm 2.5\%$ ranging from 487.5V to 512.5V. The transformer ratio is defined as the ratio between the upper voltage DC bus limit in V2G direction and the minimum battery discharging level, with $n_{\text{CLLC}} = 1.352$ which corresponds to the maximum gain $G_{\text{v2g}}^{\text{max}}$ in reverse mode. The gain intervals can be specified as $[0.652 - 0.7385]$ in G2V mode, and $[1.256 - 1.352]$ in V2G mode. The secondary side resonant components selection can start by $C_{r2} = 84\text{nF}$. The selection of the inductance on the secondary side affects the design curves with respect to switching frequency intervals, as shown in Figure 23. A good balance between a narrow switching frequency range and component values is achieved by setting L_{r2} to $120\mu\text{H}$.

From this, the resonant frequency can be computed as

$$f_r = \frac{1}{2\pi\sqrt{C_{r2}L_{r2}}} = 50\text{kHz} \quad (3.27)$$

for charging and discharging mode. The computation of the primary side tank components value is trivial and equivalent to $L_{r1} = n_{\text{CLLC}}^2 L_{r2}$ and $C_{r1} = C_{r2}/n_{\text{CLLC}}^2$, resulting in $L_{r1} = 220\mu\text{H}$ and $C_{r1} = 46\text{nF}$.

The selection of L_m depends on the ZVS condition, and it can't exceed the maximum value derived in (15). A recommended $T_{\text{dead.time}}$ is 200ns (43). From Figure 24 and Figure 25, it can be observed that a value of h close to 3 would satisfy the design requirements. Then, a suitable choice for the magnetizing inductor is $L_m = 660\mu\text{H}$ in this design, resulting in $h = 3$.

For $f_n \geq 1$ the voltage gains designed are satisfied for any load (Figure 26). For both operations, the converter operates close and above the resonant frequency f_r (peaking at $1.2f_r$) in the inductive region of the design curve, under all load conditions. The design specifications are summarized in Table IV (4).

3.4.3 DC Charging stations Voltage Gains Considerations

3.4.3.1 Discharging Mode - V2G

Let's begin by examining the various scenarios for the discharging mode, which are contingent upon the DC microgrid's voltage value. The most critical scenario occurs when the DC bus voltage reaches its peak while the battery voltage is at its lowest:

TABLE IV: DESIGN PARAMETERS

Parameters	G2V	V2G
Battery Voltage Range (V)	326-360	379-398
DC Microgrid Voltage Range (V)	487.5-500	500-512.5
Gain Range	0.652-0.7385	1.256-1.352
Operating Switching Frequency f_s (kHz)	50-60	50-60
Resonant Frequency f_r (kHz)		50
Transformer Ratio n_{CLLC}		1.352:1
Primary Resonant Capacitor C_{r1} (nF)		46
Secondary Resonant Capacitor C_{r2} (nF)		84
Primary Resonant Inductance L_{r1} (μ H)		220
Secondary Resonant Inductance L_{r2} (μ H)		120
Magnetizing Inductance L_m (μ H)		660
Dead Time T_{dead} (ns)		200
Mosfet Junction Capacitor C_{oss} (pF)		20
Load Resistance Interval R_{load} (Ω)		31-228
Output Filter Capacitor C_1 (μ F)		520
Output Filter Capacitor C_2 (μ F)		520

$$G_{v2g}^{\max} = \frac{V_{DCbus}^{V2G_{\max}}}{V_{batt}^{V2G_{\min}}} = 1.352 \quad (3.28)$$

Instead, the lower voltage gain:

$$G_{v2g}^{\min} = \frac{V_{DCbus}^{V2G_{\min}}}{V_{batt}^{V2G_{\max}}} = 1.256 \quad (3.29)$$

But, since also EVs with higher battery voltage values may occur, we might start discharging from higher battery values. Indeed, for lower voltage gains, the converter still works in the inductive region, and then higher voltage levels on the battery side can be easily accommodated.

By the way, the design is realized by accomplishing the worst scenarios, resulting in narrower battery voltage and frequency ranges.

3.4.3.2 Charging Mode - G2V

Also in this case, let's start by considering the worst scenarios, where the DC bus is at its lowest value and the battery voltage is at its maximum. It results in the following voltage gain

$$G_{g2v}^{\max} = \frac{V_{\text{batt}}^{\text{G2Vmax}}}{V_{\text{DCbus}}^{\text{G2Vmin}}} = 0.7385 \quad (3.30)$$

Instead, the minimum gain for the charging operation is defined by

$$G_{g2v}^{\min} = \frac{V_{\text{batt}}^{\text{G2Vmin}}}{V_{\text{DCbus}}^{\text{G2Vmax}}} = 0.652 \quad (3.31)$$

when the battery voltage is at its minimum value and DC bus voltage at its maximum. A better scenario, in terms of the battery charging voltage level is defined when the upper limit of the DC bus voltage range is considered. Since, for lower voltage gains, the converter still works in the inductive region, lower voltage levels in the battery side can be easily accommodated.

CHAPTER 4

CONTROL OF CLLC CONVERTER

4.1 Proposed Control Strategy for CLLC Converter

Major parts of the results and discussions in this thesis chapter are derived from my paper accepted for publication at IEEE IECON 2024 (4). A frequency modulation strategy has been implemented with closed-loop control to test the converter, which is typical for resonant converters. Despite the challenges described in the literature for this control strategy, the narrow voltage range and the resulting restricted operating frequency interval enable us to achieve soft-switching conditions for both power directions.

4.1.1 Charging Mode - G2V

The following approach utilizes a battery model to achieve the desired charging characteristics while maintaining optimal control over the charging process. Reducing frequency ripple is the primary challenge as it significantly impacts the controller's performance.

Throughout the charging process, our system employs both current-controlled and voltage-controlled loops to perform constant current (CC) and constant voltage (CV) charging, respectively, as described in Figure 27. The dual-loop architecture maintains a constant current stage until the voltage level reaches a particular state of charge (%SOC). At this point, the system switches to a CV stage, and the output current begins to track the resulting reference current from the Voltage Closed loop.

The PI controllers are tuned to ensure the frequency is within the inductive region of the design curve, resulting in $k_{pi} = 10^3$ and $k_{ii} = 10^5$. The primary challenge was the frequency ripple, which resulted in imprecise converter behavior. A centering frequency is added to ensure that the converter operates in the inductive region.

The parameters are tuned to be $k_{pv} = 0.1$ and $k_{iv} = 0.1$. The resulting reference current is multiplied by a negative unitary factor (4).

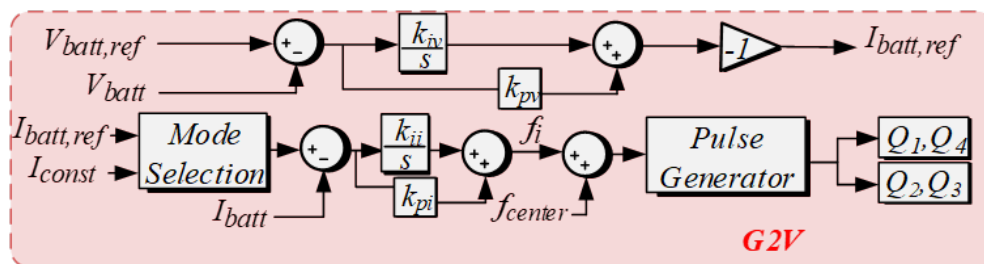


Figure 27: Proposed Control Strategy - G2V

4.1.1.1 Soft-Switching Validation in Charging Mode

In Figure 28, soft-switching conditions for both the full-bridges have been validated. Starting with the bridge formed by Q_1 , Q_2 , Q_3 , and Q_4 , ZCS at the MOSFETs turn-off has been observed, as the current circulating through the MOSFETs is zero when they turn off. Additionally, ZVS condition at MOSFET turn-on has been demonstrated, with the voltage across the MOSFETs Q_5 , Q_6 , Q_7 , and Q_8 being zero when they turn on.

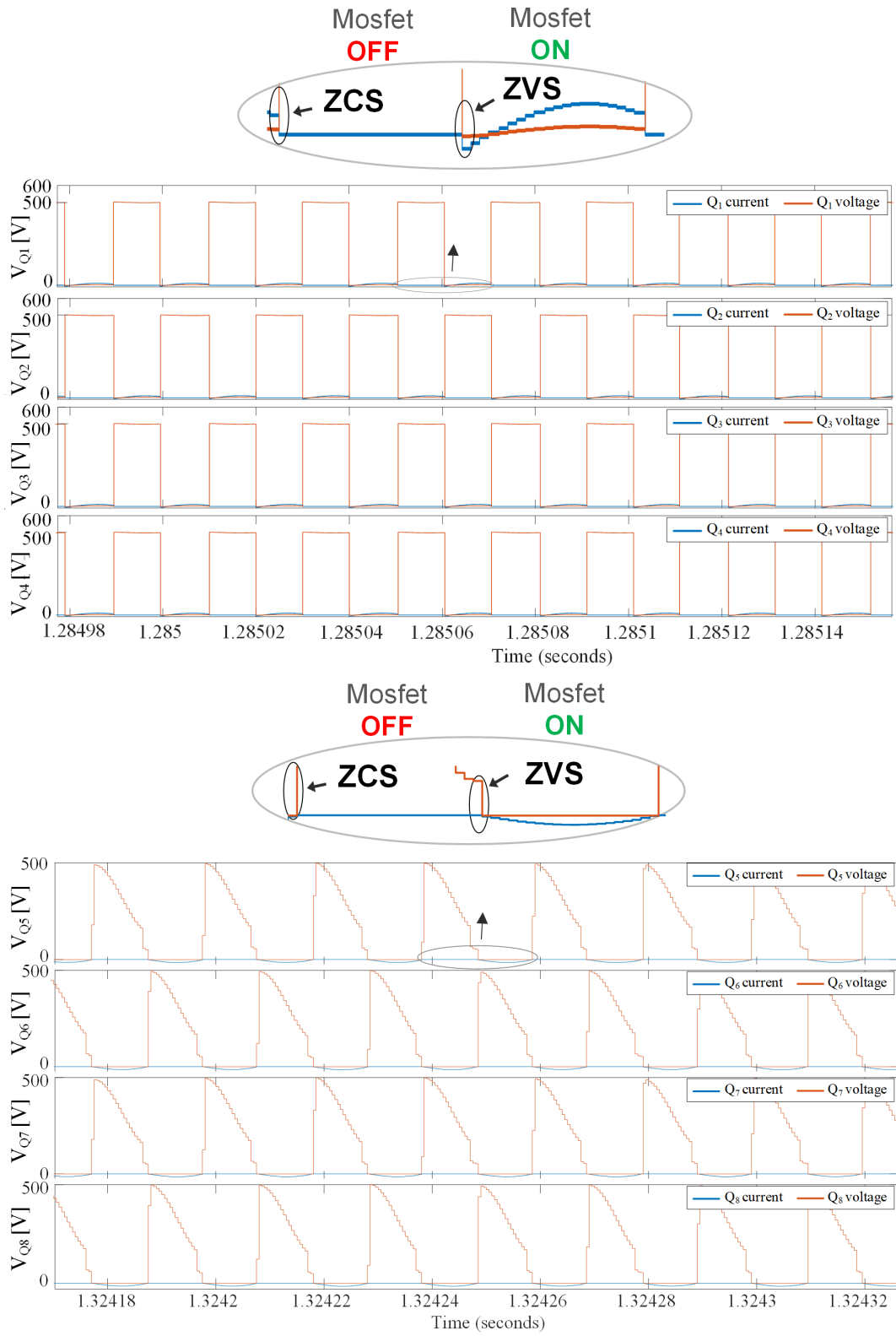


Figure 28: Soft-Switching Validation - G2V

4.1.1.2 Simulation results - G2V

In Figure 29, the charging mode simulation results are depicted. Initially, the battery voltage is at 20% of State of Charge (SOC), equating to 338V. Charging occurs under current control, adhering to a constant reference of 5A. At $t = 5.4s$, the controller transitions to constant voltage control. The battery voltage reference is adjusted to 340V, and the battery current aligns with the new reference in blue, produced by the voltage-control mechanism. To thoroughly understand the constant voltage (CV) stage, extended simulation durations are necessary, as the battery requires time to approach the set voltage reference. The converter operates within the linear control region, specifically, the inductive segment of its design curve. This is evidenced by the voltage step-down in Figure 29(a), which correlates with the frequency increase displayed in Figure 29(b). Furthermore, as the voltage rises to meet the set point, the frequency subsequently decreases post this stage. As anticipated, the SOC slope diminishes at $t = 5.4s$, as represented in Figure 29(d).

Since the converter is designed and controlled to operate close to its resonant frequency, the impedance of the resonant cavity is almost zero (86). This results in the resonant tank current waveforms shown in Figure 30, which are slightly different from the ones observed in Figure 19.

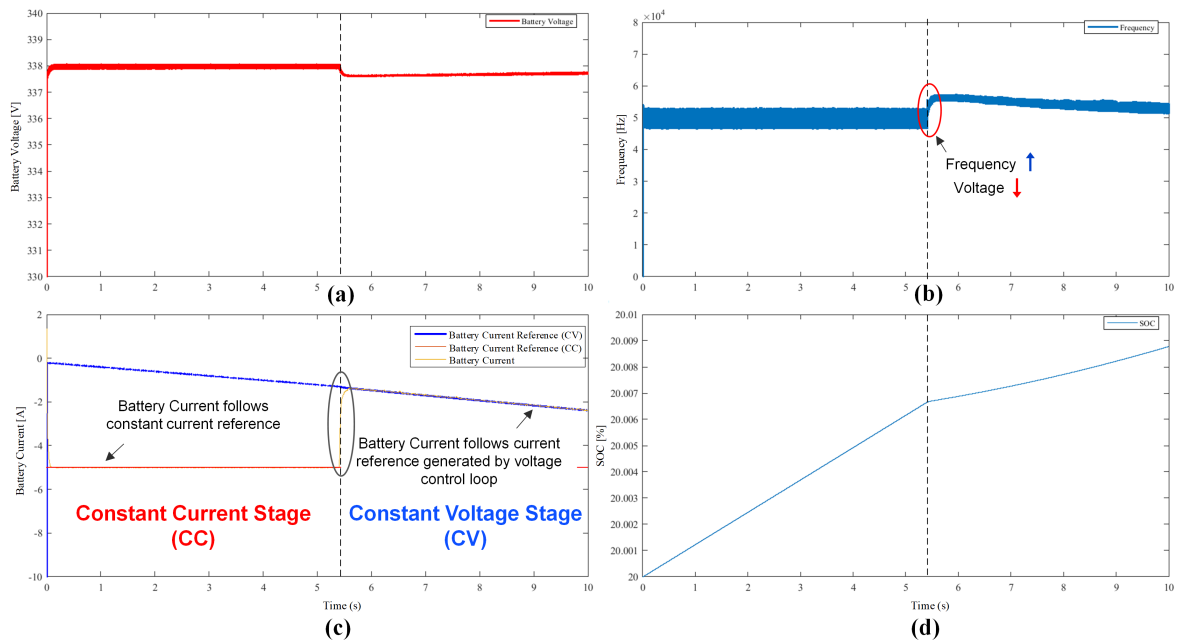


Figure 29: Control Validation after switching from Constant Current (CC) to Constant Voltage (CV). (a) Battery Voltage vs Time, (b) Frequency vs Time, (c) Battery Current vs Time, (d) SOC vs Time

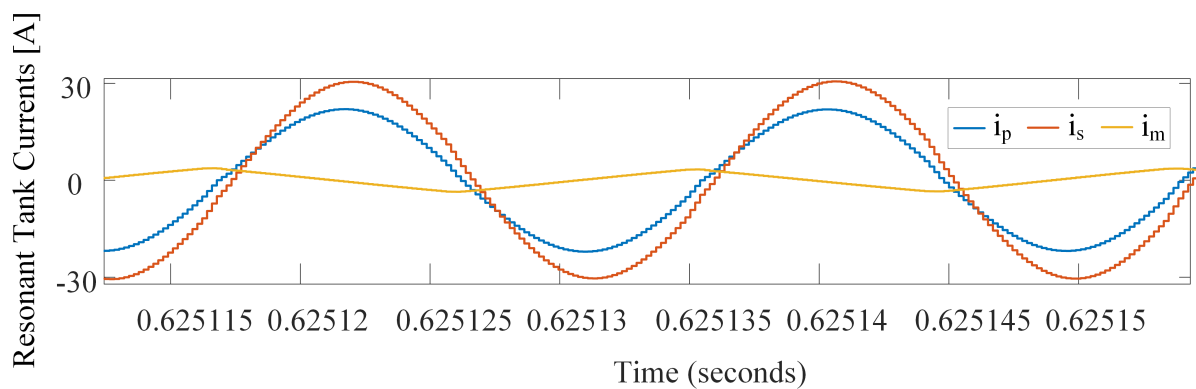


Figure 30: Resonant Tank Currents Waveforms

4.1.2 Discharging Mode - V2G

In order to regulate the voltage at a specific stage, the voltage-controlled loop was employed in discharging mode in Figure 31. The battery underwent a constant voltage (CV) discharge, and the control strategy was tested using Simulink. The converter curve presented a challenge, demonstrating four distinct frequency values at which each voltage gain was achieved. To address this issue, significant modifications were made to the voltage-closed loop. During the transient, a soft start was implemented. The frequency was decreased from a starting value to a lower one close to the resonant frequency to prevent diverging or converging into the conductive region, which would result in losing ZVS. A different reference for the DC bus voltage is generated depending on the selected mode. The PI controller was selected, resulting in $k_{pv} = 4$ and $k_{iv} = 100$. The frequency was multiplied by a negative unitary factor. Finally, a centering frequency was added to the final frequency to ensure that the converter operated in the inductive region with ZVS and the specified frequency interval (4).

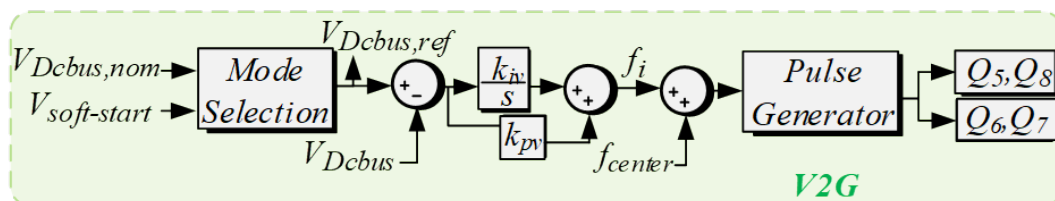


Figure 31: Proposed Control Strategy - V2G

4.1.2.1 Soft-Switching Validation in Discharging Mode

In Figure 32, soft-switching conditions for both sets of full bridges. For the bridge including Q_1 , Q_2 , Q_3 , and Q_4 , ZCS is observed at the moment these MOSFETs are turned off, due to the fact that the current through these MOSFETs becomes zero at turn-off. Similarly, ZVS conditions are achieved during the turn-on phase for Q_5 , Q_6 , Q_7 , and Q_8 , with the voltage across these MOSFETs being zero upon their activation.

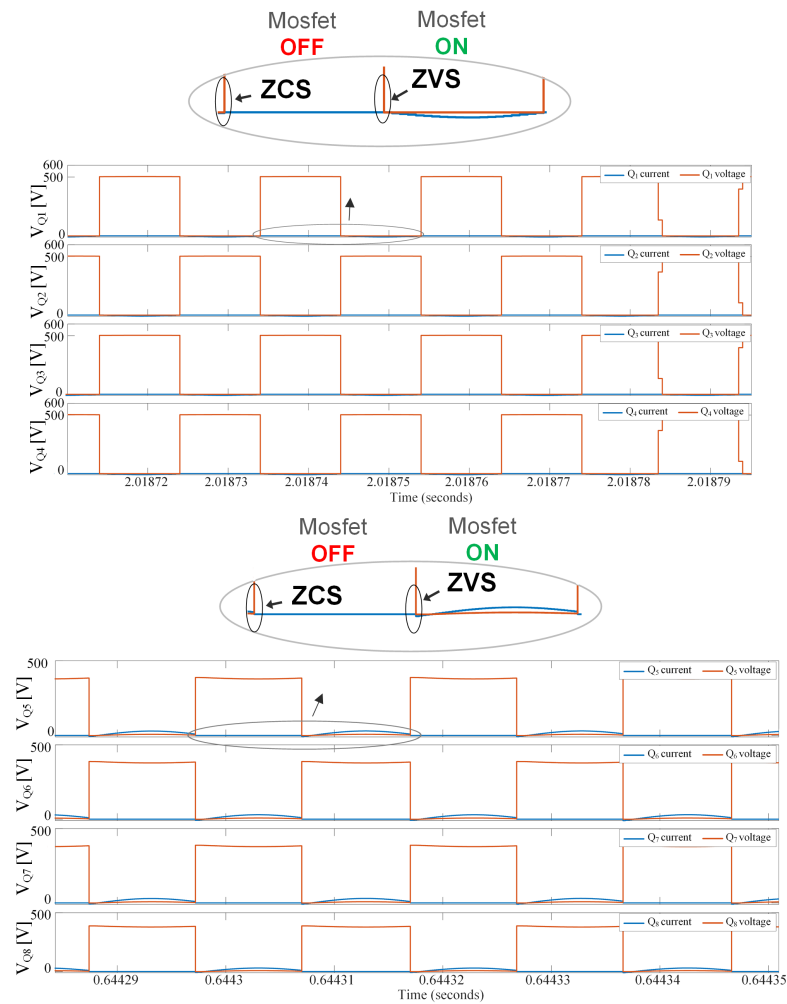


Figure 32: Soft-Switching Validation - V2G

4.1.2.2 Simulation results - V2G

In Figure 33, we verified the stability of the proposed controller for a load resistance of $R_{\text{load}} = 90\Omega$, a battery voltage of $V_{\text{batt}} = 398\text{V}$, and a voltage step-up for the DC bus from 500V to 512.5V.

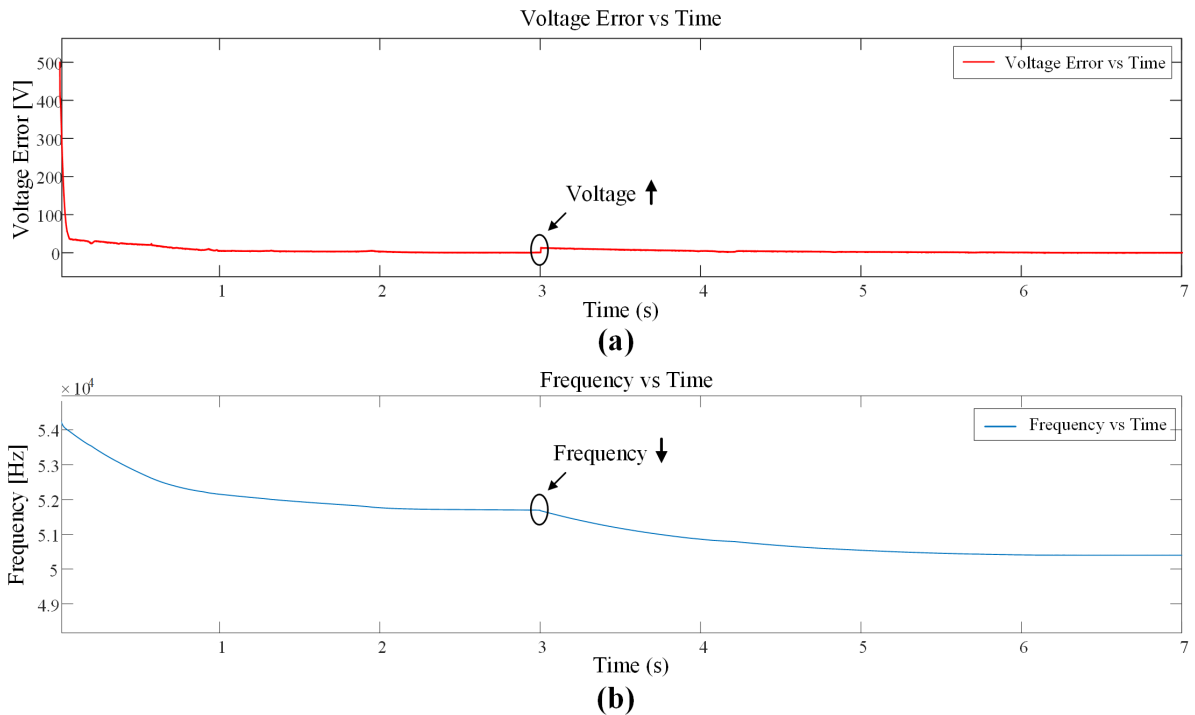


Figure 33: Voltage Step-up under Closed-Loop Control. (a) Voltage Error vs Time, (b) Frequency vs Time

Figure 34 shows the stability verification of the proposed controller for the same load resistance and battery voltage, but with a voltage step-down for the DC bus from 512.5V to 500V.

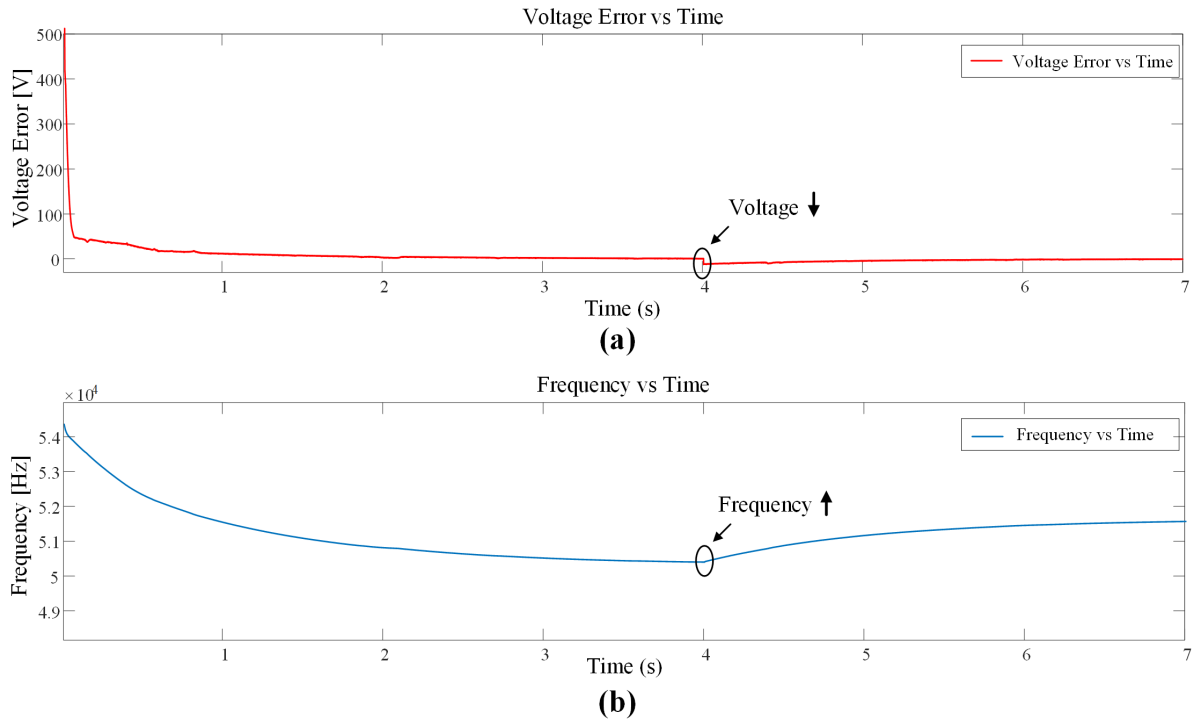


Figure 34: Voltage Step-down under Closed-Loop Control. (a) Voltage Error vs Time, (b) Frequency vs Time

In Figure 35, we verified the stability of the proposed controller for a load resistance of $R_{load} = 90\Omega$, a battery voltage of $V_{batt} = 379V$, and a voltage step-up for the DC bus from 500V to 512.5V. After the voltage step-up, the operating frequency approached 48.5kHz. Although the converter is designed with a resonant frequency of 50kHz, it operated above resonance in this case. This behavior, observed as the frequency decreased while the voltage output increased and the voltage error decreased until reaching steady zero error, indicated that the converter was operating in the linear decreasing region (inductive region) of the design curve. This phenomenon was also justified by simulations in (87) due to the lack of accuracy in FHA.

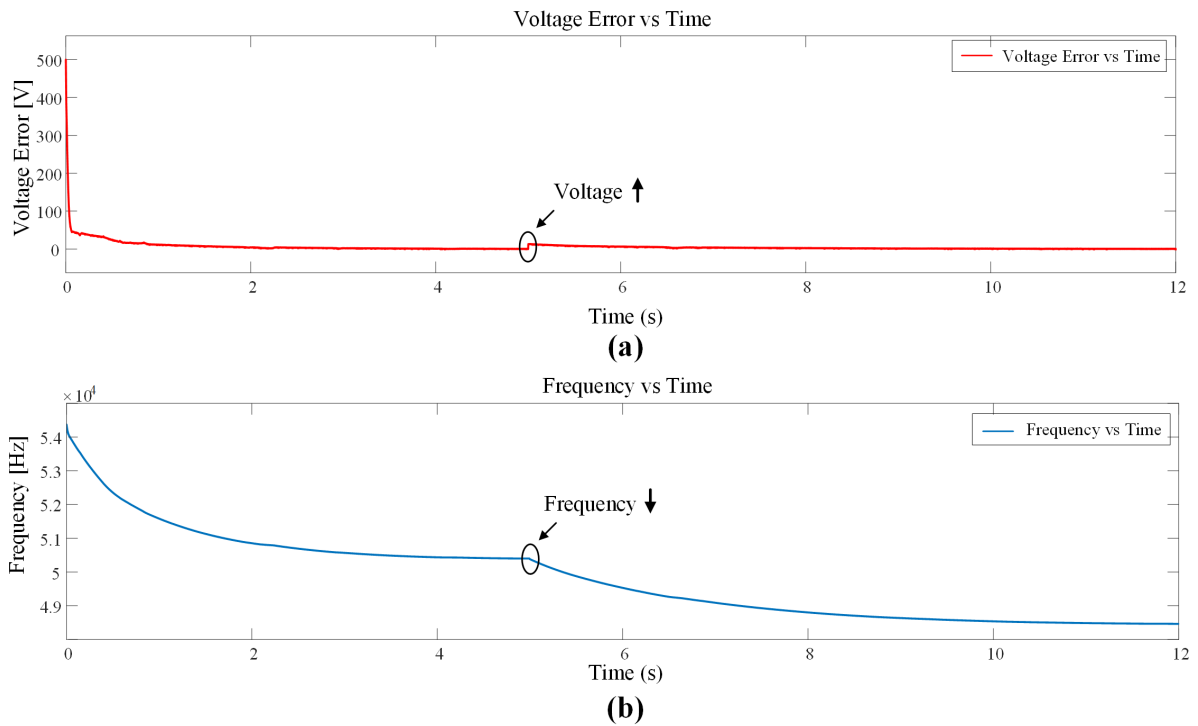


Figure 35: Voltage Step-up under Closed-Loop Control. (a) Voltage Error vs Time, (b) Frequency vs Time

Figure 36 shows the stability verification of the proposed controller for a load resistance of $R_{\text{load}} = 90\Omega$, a battery voltage of $V_{\text{batt}} = 379\text{V}$, and a voltage step-down for the DC bus from 512.5V to 500V. Before the voltage step-down, the grid voltage slowly increased, the voltage error approached zero, and the switching frequency converged to 48.5kHz. After the voltage step-down, the frequency increased and the output voltage decreased until reaching zero voltage error, and the frequency settled slightly above 50kHz.

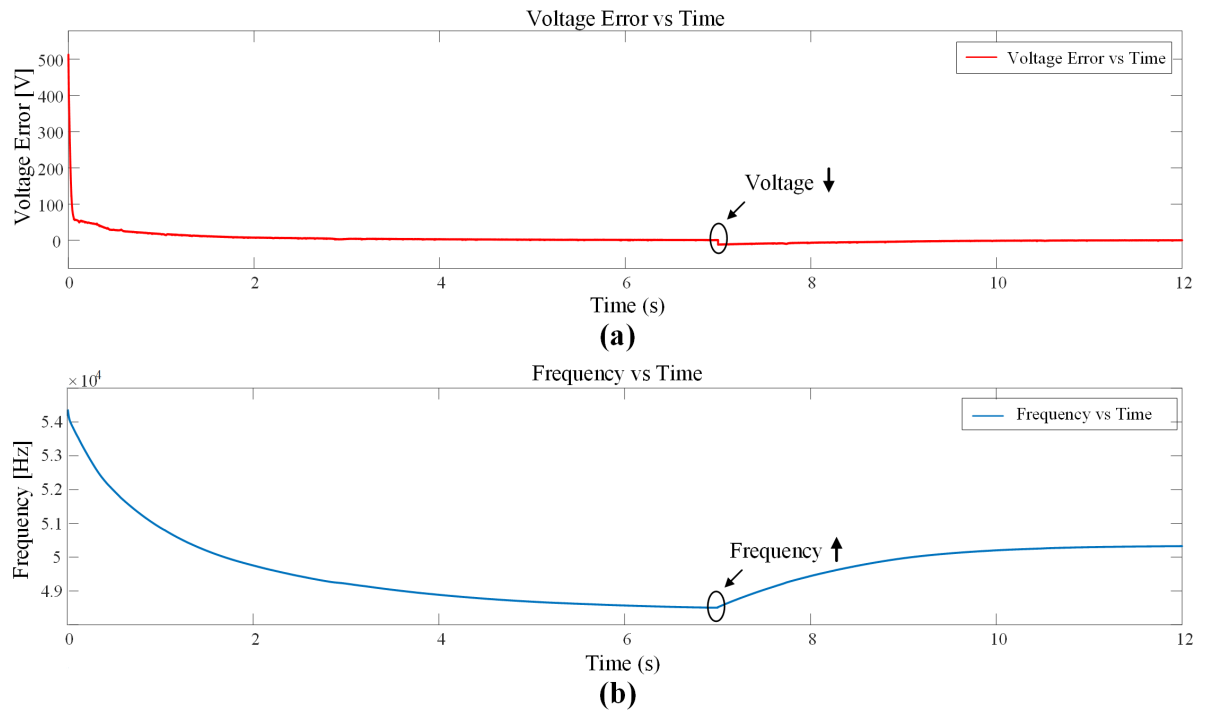


Figure 36: Voltage Step-down under Closed-Loop Control. (a) Voltage Error vs Time, (b) Frequency vs Time

CHAPTER 5

DC CHARGING STATIONS INTEGRATION IN GRID

5.1 Proposed System

Major parts of the results and discussions in this thesis chapter are derived from my paper accepted for publication at IEEE IECON 2024 (4). Figure 37 shows the structure of the DC parking lot interacting with a grid-forming inverter. Each EV is connected to the single charging station, represented by the CLLC resonant converter. All the converters interface with a DC distribution system, which is further connected to a Grid-Forming AC/DC Inverter. Finally, an isolation transformer separates the inverter from the grid (4).

5.2 DC Microgrid Stability Analysis

Major parts of the results and discussions in this thesis chapter are derived from my paper accepted for publication at IEEE IECON 2024 (4). In the system in Figure 37, for some conditions instability may occur when the DC-DC converters operate under G2V mode (89). It

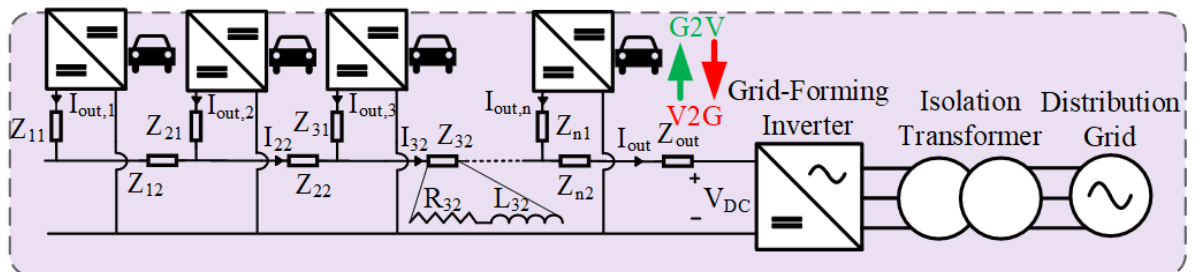


Figure 37: Proposed System Structure

follows the necessity of representing both the steady state and dynamic studies of the proposed system, as proposed in (89). Also, from the system behaviours, the existence of the steady state and the stability analysis are retrieved. Firstly, as in (89), the schematic of the proposed system structure is shown in Figure 38. Each converter is connected to the DC system through an impedance formed by the i th L_i inductance in series with the i th resistance R_i . The i th power exiting or entering each CLLC converter is denoted with $P_{c,i}$.

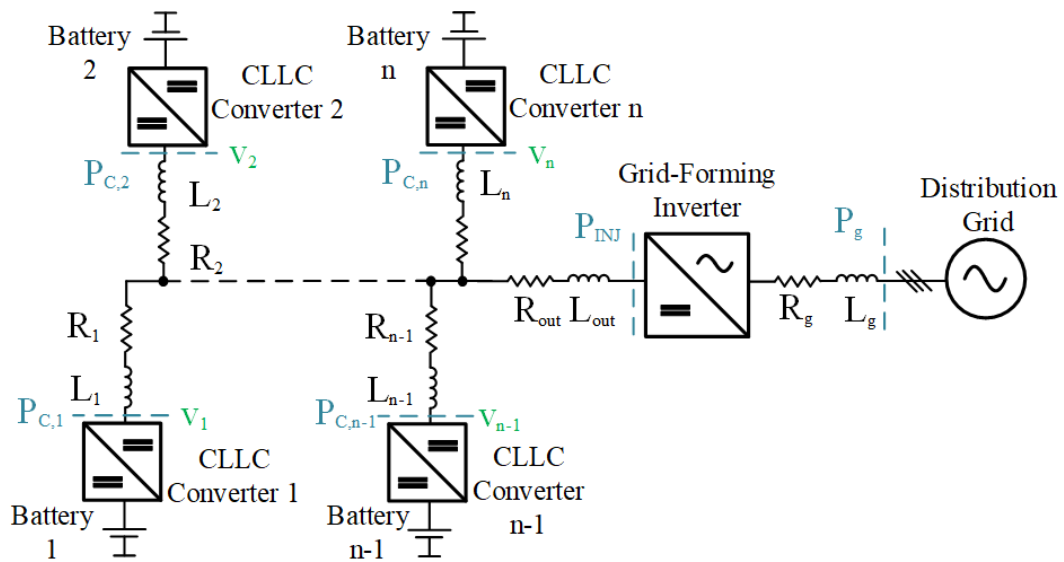


Figure 38: Schematic for Proposed DC system

In order to build the mathematical model for the proposed system, an equivalent system of the dc system must be retrieved (89).

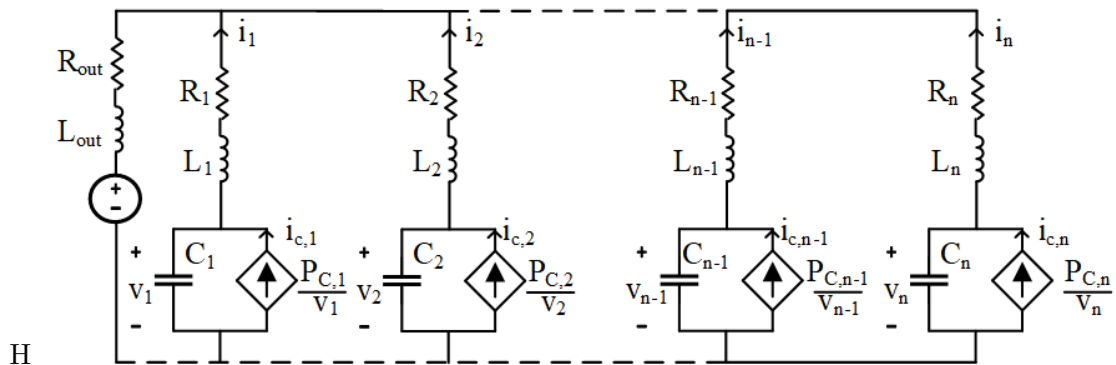


Figure 39: Equivalent circuit of the proposed dc system

In Figure 39, the grid-forming inverter is represented as a voltage dc source, while each converter is defined by a capacitor in parallel with a dependent current source (89). This is justified in (89) from the fact that the power in power devices with regulated output doesn't depend on the port voltage of the network-side. Then, the i th current of each current generator is defined as

$$i_{c,i} = \frac{P_{c,i}}{v_i} \quad (5.1)$$

where v_i defines the grid-side voltage of the i th converter. At this stage, the main assumption in (89) assumes that the DC bus of the proposed DC system corresponds with a node, as in Figure 39. Then, the differential equations neglecting the inductance and resistance related to the DC bus are presented below (89):

$$L_i \frac{di_i}{dt} + L_{out} \sum_{j=1}^n \frac{dj}{dt} + R_{out} \sum_{j=1}^n i_j - v_i + R_i i_i = v_{dc} \quad (5.2)$$

$$C_i \frac{dv_i}{dt} = \frac{P_{c,i}}{v_i} - i_i \quad (5.3)$$

For defining the existence of the steady-state some matrices of interest can be introduced.

$$\mathbf{C}_f = \begin{bmatrix} C_1 & 0 & \cdots & 0 \\ 0 & C_2 & \cdots & 0 \\ \vdots & \vdots & \ddots & \vdots \\ 0 & 0 & \cdots & C_n \end{bmatrix}, \quad \mathbf{L} = \begin{bmatrix} L_1 & 0 & \cdots & 0 \\ 0 & L_2 & \cdots & 0 \\ \vdots & \vdots & \ddots & \vdots \\ 0 & 0 & \cdots & L_n \end{bmatrix}, \quad \mathbf{R} = \begin{bmatrix} R_1 & 0 & \cdots & 0 \\ 0 & R_2 & \cdots & 0 \\ \vdots & \vdots & \ddots & \vdots \\ 0 & 0 & \cdots & R_n \end{bmatrix} \quad (5.4)$$

$$\mathbf{v} = \begin{bmatrix} v_1 \\ v_2 \\ \vdots \\ v_n \end{bmatrix}, \quad \mathbf{i} = \begin{bmatrix} i_1 \\ i_2 \\ \vdots \\ i_n \end{bmatrix}, \quad \mathbf{R} = \mathbf{R}_{out} + \mathbf{R} \quad (5.5)$$

where the matrix \mathbf{R}_{out} is a matrix defined by $n \times n$ entries equal to R_{out} , the C_i diagonal components of matrix \mathbf{C}_f display the filter capacitor for the i th converter, the L_i diagonal components of matrix \mathbf{L} represents the sum $L_{i1} + L_{i2} + L_{out}$ for the i th converter, the R_i diagonal components of matrix \mathbf{R} represents the sum $R_{i1} + R_{i2} + R_{out}$ for the i th converter, and the diagonal components of matrix \mathbf{B} are defined by the ratio between $P_{C,i}$ and V_i for the i th converter. $P_{C,i}$ represents the power the i th converter draws/absorbs, and V_i represents its output voltage. At steady state, Equation 5.2 becomes

$$\mathbf{V} = \mathbf{R}\mathbf{I} + \mathbf{V}_{dc} \quad (5.6)$$

with

$$\mathbf{V} = \begin{bmatrix} V_1 \\ V_2 \\ \vdots \\ V_n \end{bmatrix}, \quad \mathbf{I} = \begin{bmatrix} I_1 \\ I_2 \\ \vdots \\ I_n \end{bmatrix}, \quad \mathbf{V}_{dc} = \begin{bmatrix} V_{dc} \\ V_{dc} \\ \vdots \\ V_{dc} \end{bmatrix}, \quad \mathbf{B} = \begin{bmatrix} \frac{P_{c,1}}{V_1^2} & 0 & \dots & 0 \\ 0 & \frac{P_{c,2}}{V_2^2} & \dots & 0 \\ \vdots & \vdots & \ddots & \vdots \\ 0 & 0 & \dots & \frac{P_{c,n}}{V_n^2} \end{bmatrix} \quad (5.7)$$

After some manipulations, the Equation 5.6 can be rearranged as

$$P_{TOT} = \mathbf{I}^T \mathbf{V} = \mathbf{I}^T \mathbf{R} \mathbf{I} + \mathbf{I}^T \mathbf{V}_{dc} \quad (5.8)$$

where P_{TOT} is the sum of the power entering/exiting from each converter, $\mathbf{I}^T \mathbf{R} \mathbf{I}$ defines the power dissipated in the network cables, and $\mathbf{I}^T \mathbf{V}_{dc}$ the one entering into the grid-forming-inverter (89).

The minimum value for the total power P_{TOT}^{\min} must be retrieved to establish the existence of the steady-state. At this scope, after setting the derivative with respect to \mathbf{I} of the total power to zero, the related current value is computed as

$$\mathbf{I}_{P,\min} = -\frac{1}{2} \mathbf{R}^{-1} \mathbf{V}_{dc} \quad (5.9)$$

Then, by substituting $I_{P,\min}$ into Equation 5.8, the minimum value for the total power can be formulated as

$$P_{\text{TOT}}^{\min} = -\frac{1}{4} \mathbf{V}_{\text{dc}}^T \mathbf{R}^{-1} \mathbf{V}_{\text{dc}} \quad (5.10)$$

Since \mathbf{R} and \mathbf{V}_{dc} are positive definite matrices, P_{TOT}^{\min} is always negative. Then, for the existence of the steady state, we need that $P_{\text{TOT}} \geq P_{\text{TOT}}^{\min}$, that is a necessary but not sufficient condition (89).

After the definition of the condition for the existence of the steady-state, the definition of the state-space model for studying the system stability can be introduced. In (89), the following equations in matrix form showing the behavior of the DC system is proposed

$$\mathbf{L} \frac{d\tilde{\mathbf{i}}}{dt} = -\mathbf{R}\tilde{\mathbf{i}} + \tilde{\mathbf{v}}, \quad \mathbf{C}_f \frac{d\tilde{\mathbf{v}}}{dt} = -\mathbf{A}\tilde{\mathbf{v}} - \tilde{\mathbf{i}} \quad (5.11)$$

where $\tilde{\mathbf{v}}$ and $\tilde{\mathbf{i}}$ denote the perturbed variables derived by the small-signal model, from the steady-state matrices defined at Equation 5.7. Since the matrices \mathbf{C}_f and \mathbf{B} are nonsingular, the equations in Equation 5.11 can be written more compactly as $\dot{\mathbf{x}} = \mathbf{A}\mathbf{x}$, where the matrix \mathbf{A} is defined as

$$\mathbf{A} = \begin{bmatrix} -\mathbf{L}^{-1}\mathbf{R} & \mathbf{L}^{-1} \\ -\mathbf{C}_f^{-1} & -\mathbf{C}_f^{-1}\mathbf{B} \end{bmatrix} \quad (5.12)$$

while the vector \mathbf{x} is simply the $2n \times 1$ vector

$$\mathbf{x} = \begin{bmatrix} \tilde{\mathbf{i}} \\ \tilde{\mathbf{v}} \end{bmatrix}. \quad (5.13)$$

As in (89), by expressing the matrix \mathbf{A} as

$$\mathbf{A} = \mathbf{F}^{-1}\mathbf{E} \quad (5.14)$$

where

$$\mathbf{F} = \begin{bmatrix} -\mathbf{L} & \mathbf{0}_{n \times n} \\ \mathbf{0}_{n \times n} & -\mathbf{C}_f^{-1} \end{bmatrix}, \quad \mathbf{E} = \begin{bmatrix} \mathbf{R} & -\mathbf{I}_{n \times n} \\ \mathbf{I}_{n \times n} & \mathbf{B} \end{bmatrix} \quad (5.15)$$

with \mathbf{F} nonsingular. It is essential to define the eigenvalues λ of matrix \mathbf{A} , before discussing about the existence of the steady-state, and the stability of the DC microgrid. At this scope, we can formulate

$$\mathbf{A}\mathbf{w} = \lambda\mathbf{w} \quad (5.16)$$

with the eigenvector of \mathbf{A} , $\mathbf{w} \neq 0$. After some computations, precisely detailed in (89), it follows that

$$\bar{\mathbf{w}}(\mathbf{E} + \mathbf{E}^T)\mathbf{w} = 2\text{Re}(\lambda)\bar{\mathbf{w}}\mathbf{F}\mathbf{w} \quad (5.17)$$

where $\bar{\mathbf{w}}$ defines the adjoint of \mathbf{w} . Then, $\text{Re}(\lambda) > 0$ if $(\mathbf{E} + \mathbf{E}^\top)$ is positive definite, since \mathbf{F} is a real-symmetric negative-definite matrix. Finally, since $\mathbf{w} = [w_1, w_2]^\top$, where w_1 and w_2 can't both be zero, Equation 5.17 results in (89)

$$\bar{\mathbf{w}}(\mathbf{E} + \mathbf{E}^\top)\mathbf{w} = 2\bar{w}_1\mathbf{R}w_1 + 2\bar{w}_2\mathbf{B}w_2 \quad (5.18)$$

Putting Equation 5.14 into Equation 5.16 and manipulating the resulting expression, one can find that (89)

$$(\mathbf{E} - \lambda\mathbf{F})\mathbf{w} = 0 \quad (5.19)$$

then setting to zero the determinant of $(\mathbf{E} - \lambda\mathbf{F})$, defined as (89):

$$\begin{vmatrix} \mathbf{R} + \lambda\mathbf{L} & -\mathbf{I}_{n \times n} \\ \mathbf{I}_{n \times n} & \mathbf{B} + \lambda\mathbf{C}_f \end{vmatrix} = 0 \quad (5.20)$$

finally, Equation 5.20 can be rearranged as

$$\begin{vmatrix} x_1 + y_1 & x_2 & \cdots & x_n \\ x_1 & x_2 + y_2 & \cdots & x_n \\ \vdots & \vdots & \ddots & \vdots \\ x_1 & x_2 & \cdots & x_n + y_n \end{vmatrix} = 0 \quad (5.21)$$

or similarly expressed as

$$\prod_{i=1}^n y_i + \sum_{i=1}^n \left(x_i \prod_{\substack{j=1 \\ j \neq i}}^n y_j \right) = 0 \quad (5.22)$$

where the terms x_i and y_i are defined as

$$x_i = \lambda^2 L_{\text{out}} C_i + \lambda \left(R_{\text{out}} C_i + \frac{P_{C,i} L_{\text{out}}}{V_i^2} \right) + \frac{P_{C,i} R_{\text{out}}}{V_i^2}, \quad y_i = \lambda^2 L_i C_i + \lambda \left(R_i C_i + \frac{P_{C,i}}{V_i} L_i \right) + \left(1 + \frac{P_{C,i}}{V_i^2} R_i \right) \quad (5.23)$$

If none of the converters absorb power from the grid, the existence of a steady-state solution for the DC system is guaranteed. For stability, it is essential that \mathbf{B} is positive definite and the real part of its eigenvalues is always negative. This condition is both necessary and sufficient in this case of study. The most critical case for both steady-state and stability occurs when all the converters absorb their designed maximum power from the grid (4). The parameters considered at this scope are summarized in Table V.

TABLE V: PARAMETERS FOR STABILITY ANALYSIS

Variables	Value
Line Resistances R_i (m Ω)	84
Line Inductances L_i (μ H)	200
Filter Output Capacitances C_{out} (μ F)	520
Converters Grid-Side Voltages V_i (V)	500
Line Currents I_i (A)	16
Power Absorbed by Each Converter $P_{C,i}$ (kW)	8

Then, the steady-state condition is guaranteed since $P_{TOT} = -32kW$ and $P_{TOT}^{\min} = -595kW$, resulting in $P_{TOT} > P_{TOT}^{\min}$. This also ensures that the steady-state solution is guaranteed when all the power converters deliver power to the grid.

Once the steady-state has been established, we can analyze the stability of the overall system for the same scenario. After solving the 2nd-order equation in Equation 5.22, with the parameters in Table V, the resulting eigenvalue vector λ of matrix A is (89)

$$\lambda = \begin{bmatrix} -175.96 - 1438.1i \\ -175.96 + 1438.1i \\ -175.96 - 3252.5i \\ -175.96 - 3252.5i \\ -175.96 - 3252.5i \\ -175.96 + 3252.5i \\ -175.96 + 3252.5i \\ -175.96 + 3252.5i \end{bmatrix} \quad (5.24)$$

from which $\text{Re}(\lambda) < 0$. Then, we can claim that the considered system shows a steady-state solution and is stable under the worst possible case scenario in terms of DC system stability.

5.3 Minimum Line Losses Algorithm - V2G

Major parts of the results and discussions in this thesis chapter are derived from my paper accepted for publication at IEEE IECON 2024 (4).

Once the system stability has been established, an algorithm that aims to support the grid while discharging electric vehicles (EVs), prioritizing EVs with a higher percentage of state of charge (SOC) while minimizing power losses in the line is proposed. Here, the EV with the highest SOC level at arrival should inject more power into the grid. An increasing value in the index i means that the converter shows lower losses (it is located closer to the grid). The same convention is followed to define the SOC_i assigned to each EV. The optimization problem above can be transformed into a non-linear minimization problem with linear constraints as below (4)

$$\begin{aligned}
& \min_{P_i} P_{\text{loss}} \\
& \text{s.t. } P_i = V_i I_{\text{out},i}, \quad \forall i = 1, \dots, n \\
& \quad \sum_{i=1}^n P_i = P_{\text{inj}} \\
& \quad I_{i2} = I_{\text{out},i-1} + I_{\text{out},i}, \quad \forall i = 2, \dots, n \\
& \quad I_{\text{out}} = I_{\text{out},1} + I_{\text{out},2} + \dots + I_{\text{out},n} \\
& \quad P_{\text{SOC}1} \geq P_{\text{SOC}2} \geq \dots \geq P_{\text{SOC}n}
\end{aligned} \tag{5.25}$$

where

$$P_{\text{loss}} = R_{\text{line}}(2I_{\text{out},1}^2 + I_{\text{out},i}^2 + I_{i2}^2 + \dots + I_{\text{out},n}^2 + 2I_{\text{out}}^2), \quad \forall i = 2, \dots, n-1 \tag{5.26}$$

5.3.1 Simulation Results

In this section, we verified the feasibility of the algorithm considering various SOC levels for the EVs, such as their departures and arrivals. The simulation is conducted in MATLAB/

Simulink. The impact of the optimization algorithm on the discharging process of EVs at an EV charging station is compared with the conventional power sharing without loss optimization and SOC consideration.

5.3.1.1 Case 1

Figure 40 shows the power drawn to the grid by each converter and the power losses for the first three branches and the entire line, respectively, when the algorithm is not used. Initially, for $t \leq 4s$, the power is distributed as follows: 4.4kW are drawn from the EVs in positions 1 and 2 with associated SOC values of 50% and 80% respectively, while 3.1kW of power is drawn from the EV in position 3 with 70% SOC. The power drawn is lower than the one injected by the EV in position 4 with 90% SOC, around 4.1kW. A power reallocation is needed at $t_1 = 4s$ due to the EV's departure from position 3. In the interval $4s \leq t \leq 7s$, the power is distributed similarly as before, and the maximum power is injected by the 1st EV with 50% of SOC, close to 6kW. Finally, at $t_2 = 7s$ the arrival of the EV in position 3 with 80% of SOC implies another power reallocation. In this case, 4.7kW is injected from the 1st EV, 4kW from the 4th EV and around 3.5kW from the 2nd and 3rd EVs, without any consideration for losses and EVs' SOC. This results in total line losses equal to 250W for $t \leq t_1$, 275W for $t_1 \leq t \leq t_2$, and 255W for $t \geq t_2$.

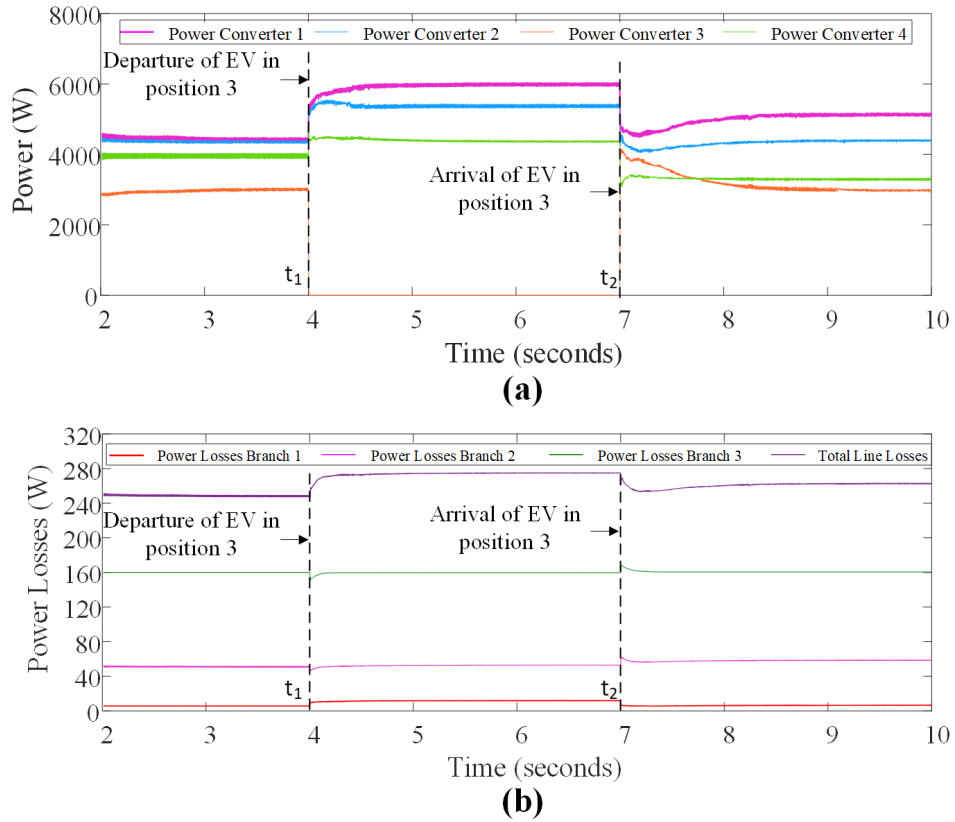


Figure 40: Case 1 without Proposed Algorithm. (a) Power Injected, (b) Power Losses

Figure 41 illustrates the results when the algorithm is implemented. Upon connection to the charging infrastructure, each vehicle's SOC is reported to the management system, triggering the commencement of the optimization algorithm's execution. Initially, power distribution favors the 4th EV, as it exhibits lower losses and higher SOC for $t \leq 4$ s. As one moves from the 3rd EV to the 1st, the amount of power allocated decreases due to increasing energy losses and a decreasing SOC in that sequence. The scenario progresses to $t_1 = 4$ s, marking the departure of the EV previously situated in position 3, which necessitates a reallocation of power distribution

in accordance with the prescribed optimization algorithm Equation 5.25. Yet, the distribution continues to adhere to the established hierarchy. Finally, the arrival of an EV in position 3 at time $t_2 = 7s$ prompts a further adjustment in power distribution. Beyond this point, since the 3rd and 2nd EVs have identical SOCs, they almost inject the same amount of power, leading to lower losses. The efficiency of the distribution algorithm is validated by a change in losses over time: starting from 205W for $t \leq t_1$, increasing to 220W between t_1 and t_2 , and finally reducing to 210W after t_2 . This demonstrates the algorithm's ability to optimize power distribution and to reduce significantly the total losses (4).

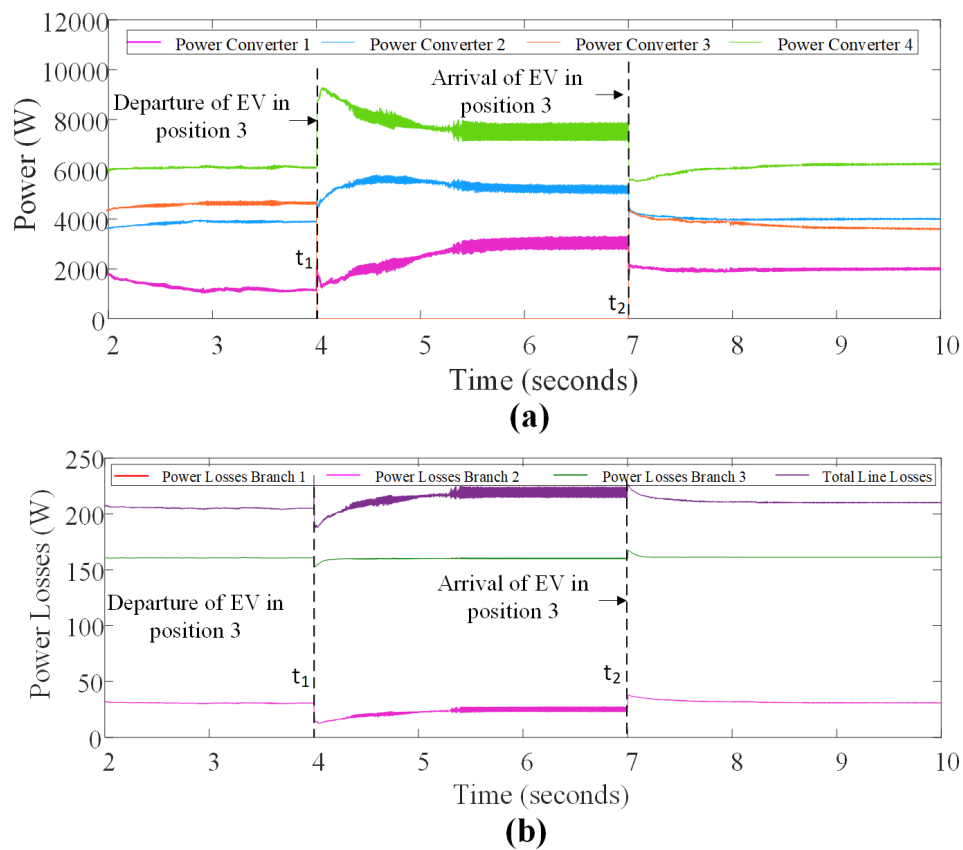


Figure 41: Case 1 with Proposed Algorithm. (a) Power Injected, (b) Power Losses

The optimization variables for both the algorithm-assisted and algorithm-independent scenarios are concisely summarized in Table VI (4), while Table VII shows the results for the 1st case of study.

TABLE VI: OPTIMIZATION PARAMETERS FOR 1st CASE OF STUDY

Variables	Value
Initial State of charge in Position 1 SOC_1 (%)	50
Initial State of charge in Position 2 SOC_2 (%)	80
Initial State of charge in Position 3 SOC_3 (%)	70
Initial State of charge in Position 4 SOC_4 (%)	90
State of charge in Position 3 at Departure SOC_3 (%)	0
State of charge in Position 3 at Arrival SOC_3 (%)	80
Total Power Injected P_{inj} (kW)	16
Line Impedance Z_{ii}	$(84 + j0.2\omega) \cdot 10^{-3}$
Output Impedance Z_{out}	$(84 + j0.2\omega) \cdot 10^{-3}$

TABLE VII: RESULTS FOR 1st CASE OF STUDY

Variables	$t \leq t_1$	$t_1 \leq t \leq t_2$	$t \geq t_2$
$P_{1,A}$ (kW)	1.6	3	2
$P_{2,A}$ (kW)	3.9	5	4
$P_{3,A}$ (kW)	4.4	0	3.8
$P_{4,A}$ (kW)	6.1	8	6.2
P_1 (kW)	4.4	6	4.7
P_2 (kW)	4.4	5.4	3.6
P_3 (kW)	3.1	0	3.7
P_4 (kW)	4.1	4.6	4
$P_{\text{loss},A}$ (W)	205	220	210
P_{loss} (W)	250	275	255

5.3.1.2 Case 2

Figure 42 shows the power drawn to the grid by each converter and the power losses for the first three branches and the entire line, respectively, when the algorithm is not used. Initially, for $t \leq 4s$, around $5.3kW$ are drawn from the EVs in positions 1, 2, and 4 with associated SOC values of 90%, 70%, and 60%, respectively, while position 3 is empty. At this stage, the power distribution is similar to what can be observed when the algorithm is adopted. A power reallocation is needed at $t_1 = 4s$ due to the EV's arrival in position 3, and the simultaneous departure of the 2nd EV. In the interval $4s \leq t \leq 7s$, the power is distributed as follows: the maximum power is injected by the 1st EV with 90% of SOC, close to $7kW$, while $6.5kW$ and $2.5kW$ are drawn by the EVs in position 4 and 3. Finally, at $t_2 = 7s$ the arrival of the EV in position 2 with 50% of SOC implies another power reallocation. In this case, $4.7kW$ is injected from the 2nd EV, $4.8kW$ from the 1st EV, $3.4kW$ from the 3rd, and $3.1kW$ from the last EV, without any consideration for losses and EVs' SOC. This results in total line losses equal to $265W$ for $t \leq t_1$, $240W$ for $t_1 \leq t \leq t_2$, and $260W$ for $t \geq t_2$.

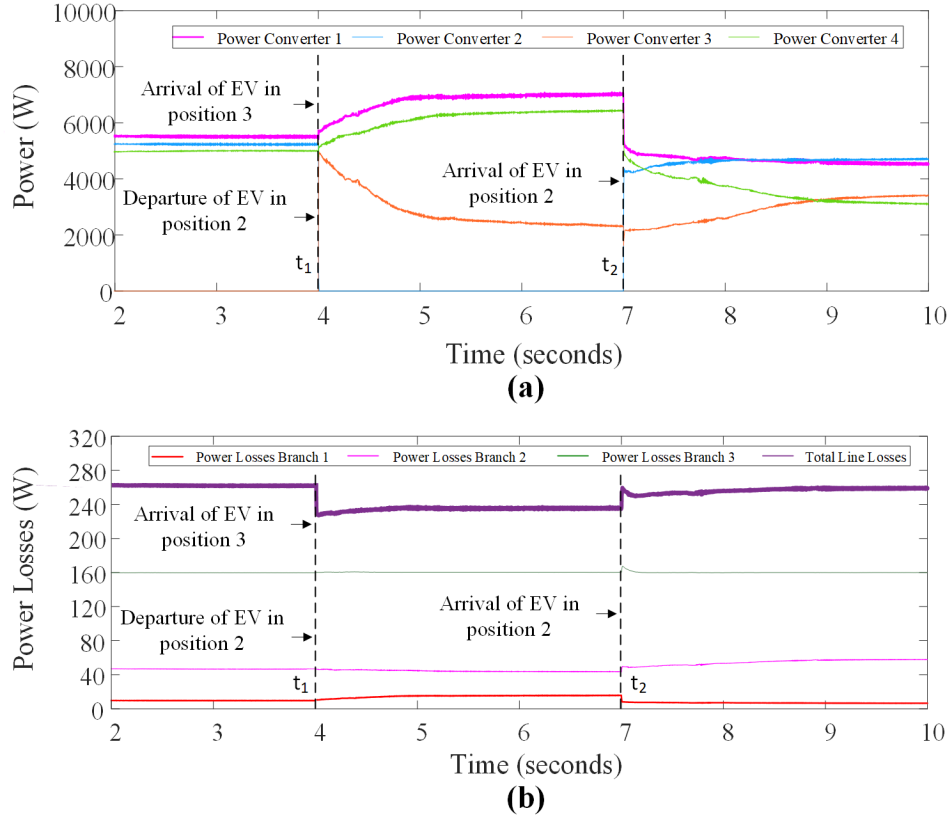


Figure 42: Case 2 without Proposed Algorithm. (a) Power Injected, (b) Power Losses

Figure 43 illustrates the results when the the algorithm is implemented. Upon connection to the charging infrastructure, each vehicle's SOC is reported to the management system, triggering the commencement of the optimization algorithm's execution. Initially, the power is equally distributed between the 1st, 2nd and 4th EVs. 5.3kW are injected by each of them for $t \leq 4$ s. At $t = 4$ s, as the 3rd EV arrives, and the EV in position 2 leaves, the power distribution almost remains the same since the SOC of the EV in position 3 is the lowest, similar to the EV in position 2 in the previous time interval. The scenario progresses to $t_2 = 7$ s, marking

the arrival of the EV in position 2, which necessitates a reallocation of power distribution in accordance with the prescribed optimization algorithm Equation 5.25. Beyond this point, similar power levels are drawn from the EVs in position 4 and 1, around 5kW, while close to 4kW are injected by the 2nd and 3rd EVs. The distribution algorithm's efficiency is validated by monitoring changes in losses over time: starting from 260W for $t \leq t_1$, increasing to 220W between t_1 and t_2 , and finally 235W after t_2 .

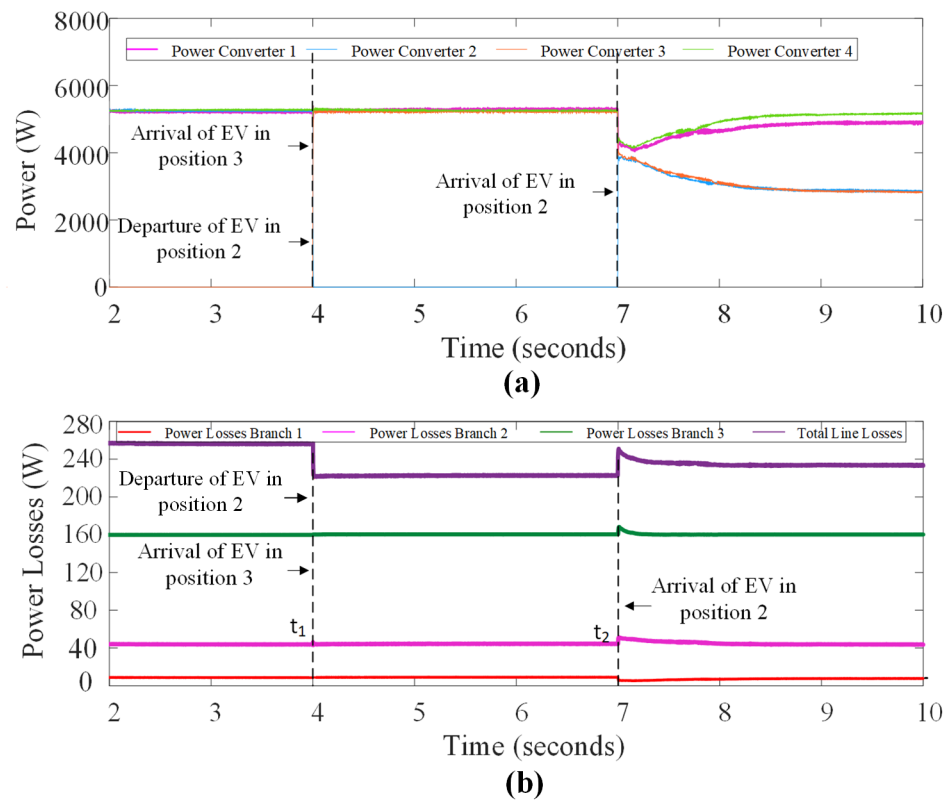


Figure 43: Case 2 with Proposed Algorithm. (a) Power Injected, (b) Power Losses

The optimization variables for both the algorithm-assisted and algorithm-independent scenarios are concisely summarized in Table VIII, while Table IX shows the results for the 2nd case of study.

TABLE VIII: OPTIMIZATION PARAMETERS FOR 2nd CASE OF STUDY

Variables	Value
Initial State of charge in Position 1 SOC_1 (%)	90
Initial State of charge in Position 2 SOC_2 (%)	70
Initial State of charge in Position 3 SOC_3 (%)	0
Initial State of charge in Position 4 SOC_4 (%)	60
State of charge in Position 2 at Departure SOC_2 (%)	0
State of charge in Position 3 at Arrival SOC_3 (%)	55
State of charge in Position 2 at Arrival SOC_2 (%)	50
Total Power Injected P_{inj} (kW)	16
Line Impedance Z_{ii}	$(84 + j0.2\omega) \cdot 10^{-3}$
Output Impedance Z_{out}	$(84 + j0.2\omega) \cdot 10^{-3}$

TABLE IX: RESULTS FOR 2nd CASE OF STUDY

Variables	$t \leq t_1$	$t_1 \leq t \leq t_2$	$t \geq t_2$
$P_{1,A}$ (kW)	5.3	5.3	5.2
$P_{2,A}$ (kW)	5.3	5.3	2.8
$P_{3,A}$ (kW)	0	5.3	2.8
$P_{4,A}$ (kW)	5.3	0	5.2
P_1 (kW)	5.5	7	4.7
P_2 (kW)	5.3	0	4.8
P_3 (kW)	0	2.5	3.4
P_4 (kW)	5.2	6.5	3.1
$P_{\text{loss},A}$ (W)	260	220	235
P_{loss} (W)	265	240	260

5.3.1.3 Case 3

Figure 44 shows the power injected to the grid by each converter and the power losses for the first three branches and the entire line, respectively, when the algorithm is not used for the 3rd case of study. Initially, for $t \leq 4s$, the power is distributed as follows: Approximately 7.3kW and 6.7kW are drawn, respectively, from the EVs in positions 4 and 1 with associated SOC values of 70% and 60%, respectively, while positions 2 and 3 are empty. A power reallocation is needed at $t_1 = 4s$ due to the EV's arrival in position 3. In the interval $4s \leq t \leq 7s$, the power is distributed as follows: the maximum power is injected by the 4th EV with 70% of SOC, close to 8kW, while 3.8kW and 2.2kW are drawn from EVs in position 1 and 3. Finally, at $t_2 = 7s$ the arrival of the EV in position 2 with 55% of SOC implies another power reallocation. Also, the total amount of power injected into the grid increases from 14kW to 16kW. In this case, 5kW is injected from the 4th EV, 3.5kW from the 1st and 2nd EVs, and around 4kW from the 2nd one, without any consideration for losses and EVs' SOC. This results in total line losses equal to 180W for $t \leq t_1$, 200W for $t_1 \leq t \leq t_2$, and 225W for $t \geq t_2$.

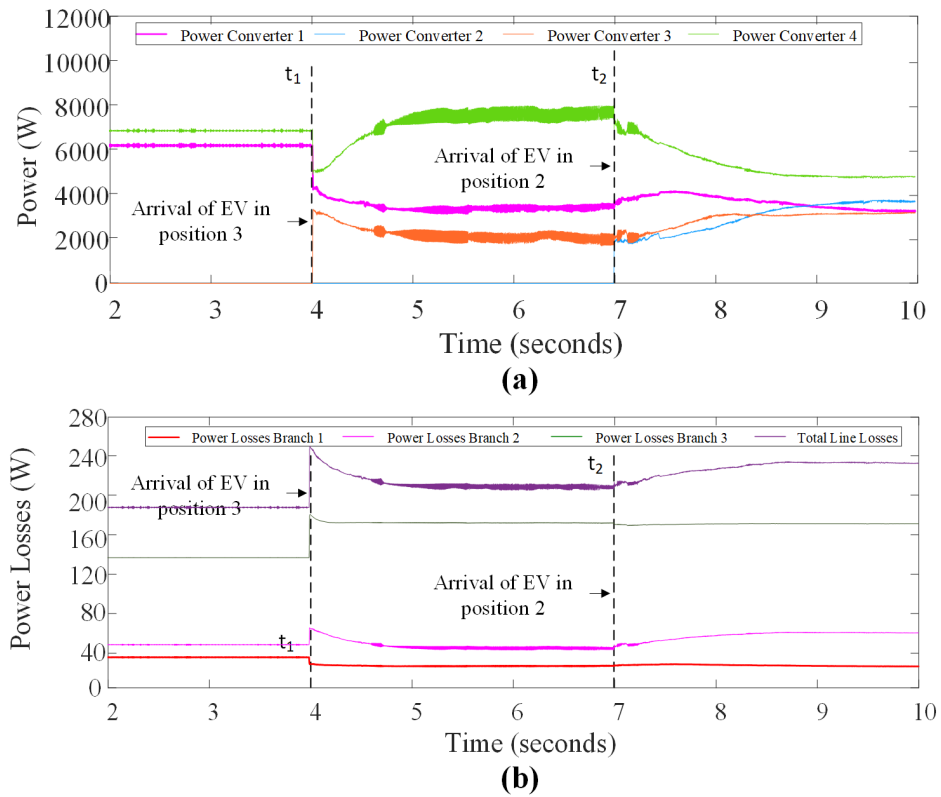


Figure 44: Case 3 without Proposed Algorithm. (a) Power Injected, (b) Power Losses

Figure 45 illustrates the results when the algorithm is implemented. Initially, power distribution favors the 4th EV, as it exhibits lower losses and maintains higher SOC for $t \leq 4$ s. Since the maximum power drawn from each EV is set to 8kW, 6kW are drawn from the 1st EV. The scenario progresses to $t_1 = 4$ s, indicating the arrival of an EV at position 3 in accordance with the optimization algorithm Equation 5.25. So, a similar amount of power is drawn from the EV in position 4, while around 3kW are injected from the 1st and 3rd EVs. Finally, the arrival of an EV in position 2 at time $t_2 = 7$ s prompts a further adjustment in power distribution. After that, the 4th EV injects the maximum power limit, and the same amount of power is drawn

from the other EVs, resulting in lower losses. The losses after the algorithm implementations are as follows: starting from 165W for $t \leq t_1$, increasing to 200W between t_1 and t_2 , and finally reducing to 195W after t_2 . This demonstrates the algorithm's ability to optimize power distribution and to significantly reduce total losses.

Obviously, the impact of the algorithm on reducing losses is less clear in the second time interval, as the maximum power has been drawn from the 4th EV even without the algorithm in this case.

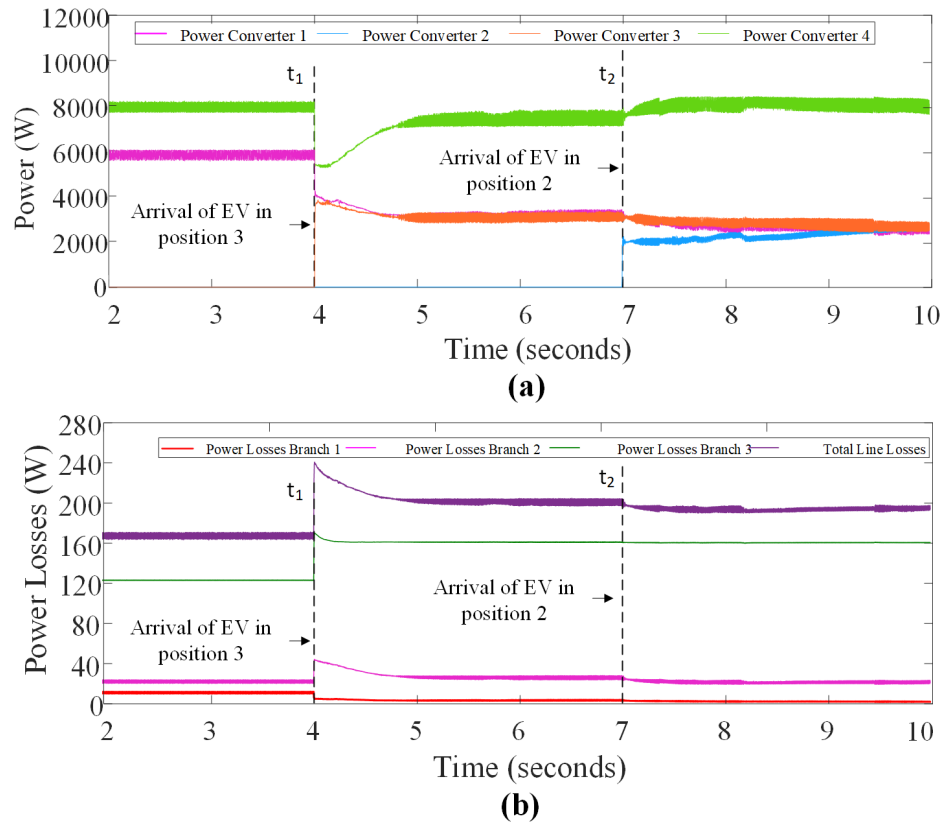


Figure 45: Case 3 with Proposed Algorithm. (a) Power Injected, (b) Power Losses

The optimization variables for both the scenarios with and without algorithm assistance are concisely summarized in Table X, while the results are presented in Table XI.

TABLE X: OPTIMIZATION PARAMETERS FOR 3rd CASE OF STUDY

Variables	Value
Initial State of charge in Position 1 SOC_1 (%)	60
Initial State of charge in Position 2 SOC_2 (%)	0
Initial State of charge in Position 3 SOC_3 (%)	0
Initial State of charge in Position 4 SOC_4 (%)	70
State of charge in Position 3 at Arrival SOC_3 (%)	50
State of charge in Position 2 at Arrival SOC_2 (%)	55
Total Power Injected $P_{\text{inj},0}$ (kW)	14
Total Power Injected $P_{\text{inj},1}$ (kW)	16
Line Impedance Z_{ii}	$(84 + j0.2\omega) \cdot 10^{-3}$
Output Impedance Z_{out}	$(84 + j0.2\omega) \cdot 10^{-3}$

TABLE XI: RESULTS FOR 3rd CASE OF STUDY

Variables	$t \leq t_1$	$t_1 \leq t \leq t_2$	$t \geq t_2$
$P_{1,A}$ (kW)	6	3.25	2.7
$P_{2,A}$ (kW)	0	0	2.7
$P_{3,A}$ (kW)	0	3.25	2.7
$P_{4,A}$ (kW)	8	7.5	8
P_1 (kW)	6.7	3.8	3.5
P_2 (kW)	0	0	3.5
P_3 (kW)	0	2.2	4
P_4 (kW)	7.3	8	5
$P_{\text{loss},A}$ (W)	165	200	195
P_{loss} (W)	180	200	225

5.3.1.4 Case 4

Figure 46 shows the power injected to the grid by each converter and the power losses for the first three branches and the entire line, respectively, when the algorithm is not used for the 4th case of study. Initially, the 1st and 4th charging stations are empty. Then, for $t \leq 4s$, the power is distributed as follows: Approximately 7.5kW and 6.5kW are drawn, respectively, from the EVs in positions 2 and 3 with associated SOC values of 60% and 70%, respectively. A power reallocation is needed at $t_1 = 4s$ due to the Evs' arrival in positions 1 and 4. Also, the power injected into the grid increases from 14kW to 16kW. In the interval $4s \leq t \leq 7s$, the power is distributed as follows: the maximum power is injected by the 1st and 4th EVs with 50% of SOC each, close to 5kW, while 2.3kW and 3.7kW are drawn from the EVs in position 2 and 4. Finally, at $t_2 = 7s$ the departure of the EV in position 3 implies another power reallocation. In this time interval, 6.2kW is injected from the 1st EV, 4.4kW from the 2nd, and 5.4kW from the 4th EV, without any consideration for losses and EVs' SOC. This results in total line losses equal to 220W for $t \leq t_1$, 245W for $t_1 \leq t \leq t_2$, and 265W for $t \geq t_2$.

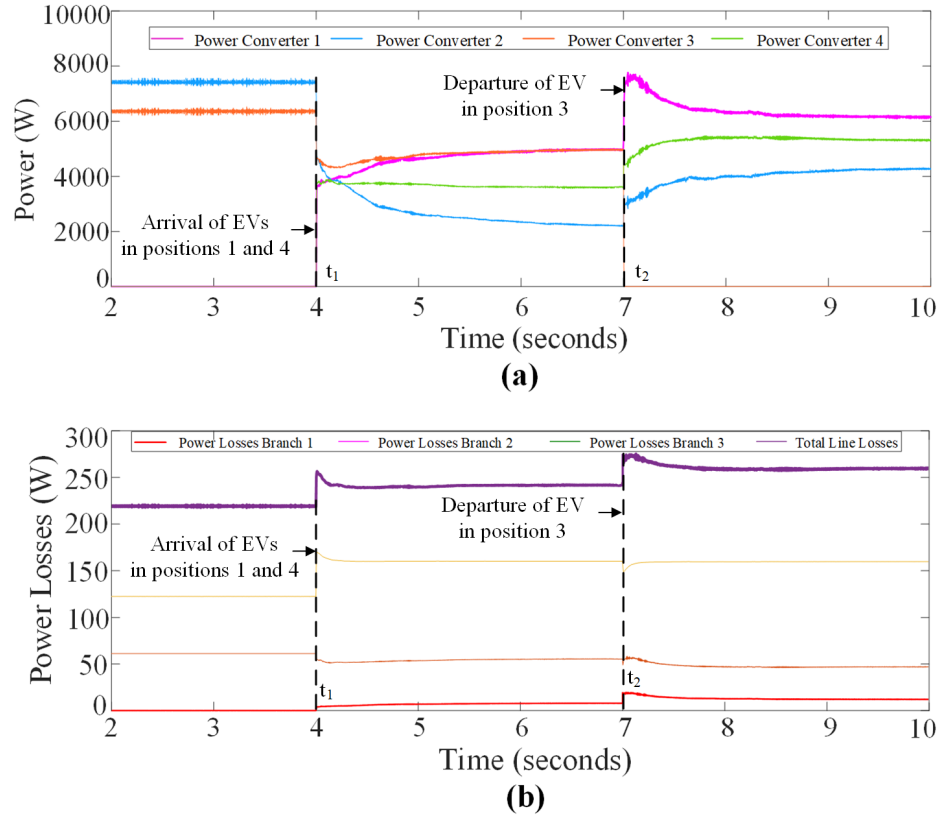


Figure 46: Case 4 without Proposed Algorithm. (a) Power Injected, (b) Power Losses

Figure 47 illustrates the results when the algorithm is implemented. Initially, power distribution favors the 3rd EV, as it exhibits lower losses and maintains higher SOC for $t \leq 4$ s. Since the maximum power drawn from each EV is set to 8kW, 6kW are drawn from the 2nd EV. The scenario progresses to $t_1 = 4$ s, indicating the arrival of an EVs at positions 1 and 4 in accordance with the optimization algorithm Equation 5.25. So, a similar amount of power is drawn from the EVs in positions 1,2 and 4, while around 5.8kW are injected from the 3rd EV. Finally, the departure of the EV in position 3 at time $t_2 = 7$ s prompts a further adjustment in power distribution. Then, all the remaining EVs inject 5.3kW into the grid. The losses after

the algorithm implementations are as follows: starting from 205W for $t \leq t_1$, increasing to 235W between t_1 and t_2 , and finally reducing to 260W after t_2 .

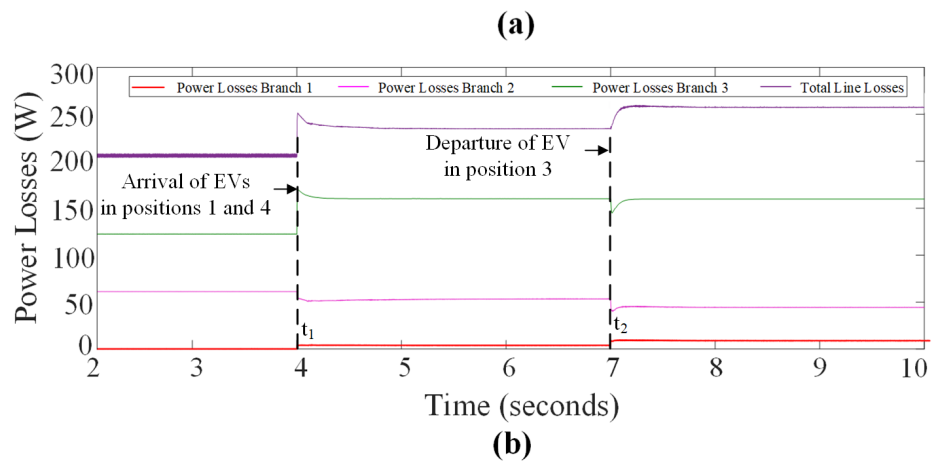
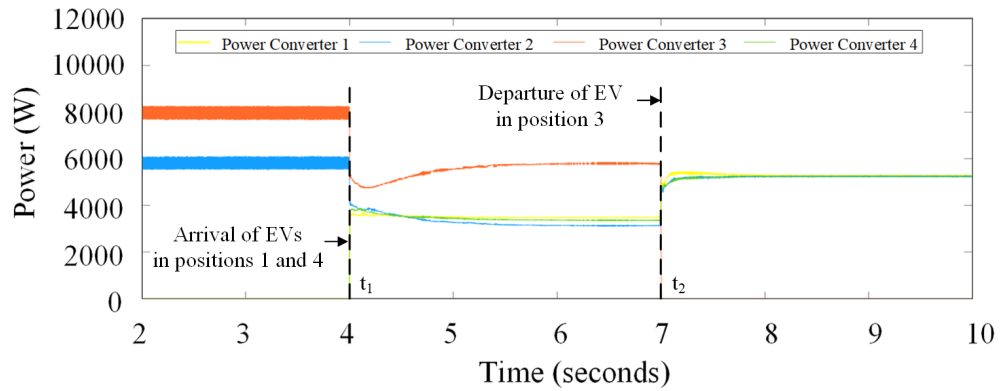


Figure 47: Case 4 with Proposed Algorithm. (a) Power Injected, (b) Power Losses

The optimization variables for both the scenarios with and without algorithm assistance are concisely summarized in Table XII, while the results are presented in Table XIII.

TABLE XII: OPTIMIZATION PARAMETERS FOR 4th CASE OF STUDY

Variables	Value
Initial State of charge in Position 1 SOC ₁ (%)	0
Initial State of charge in Position 2 SOC ₂ (%)	60
Initial State of charge in Position 3 SOC ₃ (%)	70
Initial State of charge in Position 4 SOC ₄ (%)	0
State of charge in Position 1 at Arrival SOC ₁ (%)	50
State of charge in Position 4 at Arrival SOC ₄ (%)	50
State of charge in Position 3 at Departure SOC ₃ (%)	0
Total Power Injected P _{inj,0} (kW)	14
Total Power Injected P _{inj,1} (kW)	16
Total Power Injected P _{inj,2} (kW)	16
Line Impedance Z _{ii}	$(84 + j0.2\omega) \cdot 10^{-3}$
Output Impedance Z _{out}	$(84 + j0.2\omega) \cdot 10^{-3}$

TABLE XIII: RESULTS FOR 4th CASE OF STUDY

Variables	$t \leq t_1$	$t_1 \leq t \leq t_2$	$t \geq t_2$
P _{1,A} (kW)	0	3.4	5.3
P _{2,A} (kW)	6	3.4	5.3
P _{3,A} (kW)	8	5.8	0
P _{4,A} (kW)	0	3.4	5.3
P ₁ (kW)	0	5	6.2
P ₂ (kW)	7.5	2.3	4.4
P ₃ (kW)	6.5	5	0
P ₄ (kW)	0	3.7	5.4
P _{loss,A} (W)	205	235	260
P _{loss} (W)	220	245	265

5.3.1.5 Case 5

Figure 48 shows the power drawn to the grid by each converter and the power losses for the first three branches and the entire line, respectively, when the algorithm is not used. For $t \leq 4s$, the power is distributed as follows: 3.7kW are drawn from the EV in positions 1

associated SOC values of 50%, 2.5kW are from the EV in positions 2 with 60% of SOC, and 4.1kW and 5.7kW from the EVs in positions 3 and 4, which show 60% and 80% of SOC. A power reallocation is needed at $t_1 = 4s$ due to the EVs' departures from positions 2 and 4. In the interval, $4s \leq t \leq 7s$, the same power is injected to the 1st and 3rd EVs, respectively, with 50% and 60% of SOC. Finally, at $t_2 = 7s$ the arrival of the EV in position 2 with 80% of SOC implies another power reallocation. Here, 5.8kW are injected from the EV in position 1 (it shows the lowest SOC), while 5.5kW and 4.7kW are drawn from the remaining two EVs. This results in total line losses equal to 225W for $t \leq t_1$, 230W for $t_1 \leq t \leq t_2$, and 310W for $t \geq t_2$.

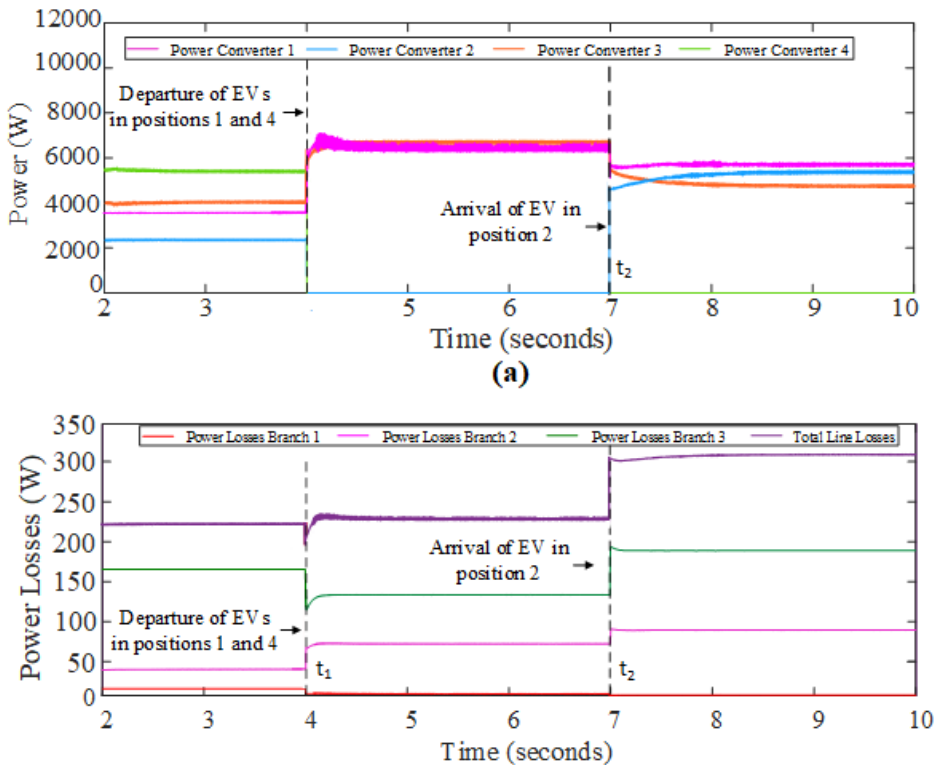


Figure 48: Case 5 without Proposed Algorithm. (a) Power Injected, (b) Power Losses

Figure 49 illustrates the results when the algorithm is implemented. Initially, power distribution favors the 4th EV, as it exhibits lower losses and maintains SOC for $t \leq 4s$. The 2nd and 3rd EVs inject the same amount of power, while the EV in position 1, only 800W, since it shows the lowest SOC and highest losses. The scenario progresses to $t_1 = 4s$, marking the departure of the EVs previously situated in positions 2 and 4, which necessitates a reallocation of power distribution in accordance with the prescribed optimization algorithm Equation 5.25. Now 8kW are drawn from the 3rd EV and 6kW from the 1st one. Finally, the arrival of an EV in position 2 at time $t_2 = 7s$ prompts a further adjustment in power distribution. Beyond this point, the 3rd and 2nd EVs having identical SOC, and the same amount of power is drawn from them. The efficiency of the distribution algorithm is validated by lower losses with respect to the case without the proposed algorithm: starting from 225W for $t \leq t_1$, increasing to 230W between t_1 and t_2 , and further increasing to 285W after t_2 .

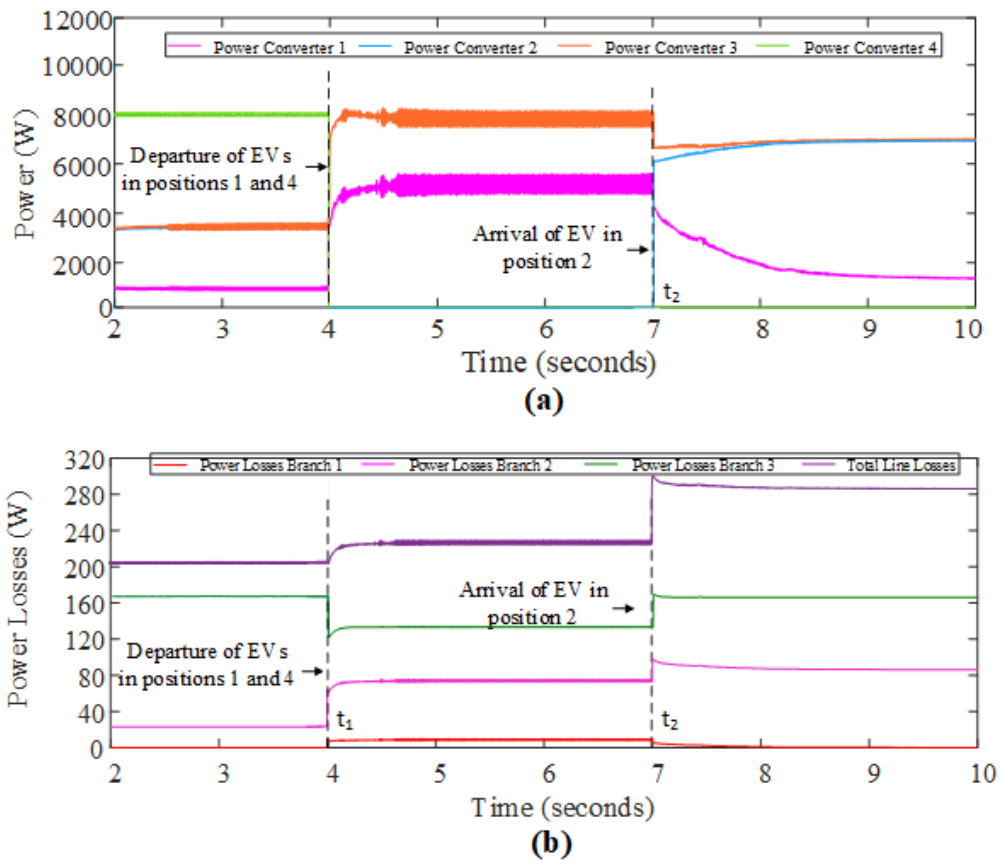


Figure 49: Case 5 with Proposed Algorithm. (a) Power Injected, (b) Power Losses

The optimization variables for both the algorithm-assisted and algorithm-independent scenarios are detailed in Table XIV, while Table XV describes the results for the 5th case of study.

TABLE XIV: OPTIMIZATION PARAMETERS FOR 5th CASE OF STUDY

Variables	Value
Initial State of charge in Position 1 SOC_1 (%)	50
Initial State of charge in Position 2 SOC_2 (%)	60
Initial State of charge in Position 3 SOC_3 (%)	60
Initial State of charge in Position 4 SOC_4 (%)	80
State of charge in Position 2 at Departure SOC_2 (%)	0
State of charge in Position 4 at Departure SOC_4 (%)	0
State of charge in Position 2 at Arrival SOC_2 (%)	60
Total Power Injected $P_{\text{inj},0}$ (kW)	16
Total Power Injected $P_{\text{inj},1}$ (kW)	14
Total Power Injected $P_{\text{inj},2}$ (kW)	16
Line Impedance Z_{ii}	$(84 + j0.2\omega) \cdot 10^{-3}$
Output Impedance Z_{out}	$(84 + j0.2\omega) \cdot 10^{-3}$

TABLE XV: RESULTS FOR 5th CASE OF STUDY

Variables	$t \leq t_1$	$t_1 \leq t \leq t_2$	$t \geq t_2$
$P_{1,A}$ (kW)	0.8	6	1.6
$P_{2,A}$ (kW)	3.6	0	7.2
$P_{3,A}$ (kW)	3.6	8	7.2
$P_{4,A}$ (kW)	8	0	0
P_1 (kW)	3.7	7	5.8
P_2 (kW)	2.5	0	5.5
P_3 (kW)	4.1	7	4.7
P_4 (kW)	5.7	0	0
$P_{\text{loss},A}$ (W)	205	225	285
P_{loss} (W)	225	230	310

CHAPTER 6

CLOSING REMARKS AND FUTURE WORK

6.1 Closing Remarks

Major parts of the results and discussions in this thesis chapter are derived from my paper accepted for publication at IEEE IECON 2024 (4). In this thesis optimization algorithm has been proposed to manage the integration of DC charging stations into the power grid. The system is made up of a group of EVs in a parking lot that exchange energy with the DC distribution system through bidirectional CLLC resonant converters. The DC microgrid is connected to a grid-forming inverter, which allows for the exchange of energy with the AC grid. The non-linear optimization algorithm implemented is linearly constrained, with the goal of minimizing line losses. It also aims to distribute the injected power to the grid based on the EV's SOC upon arrival and updates the drawn power from each converter upon any EV's departure or arrival. Additionally, a CLLC converter design specifically for DC charging stations has been proposed. The design achieves linear control, soft-switching, and meets FHA design specifications. A frequency modulation control strategy has also been implemented, which makes the converter work in the inductive region at any load condition. Finally, simulation results based on the proposed scenarios highlight the algorithm's effectiveness in minimizing losses compared to random power assignments without any algorithm assistance (4).

6.2 Future Work

This thesis lays the foundation for future exploration in this related area, including:

1. Hardware implementation of the proposed system
2. Improving CLLC Converter Voltage Ranges: Enhancing the voltage ranges for both battery and grid sides will increase the flexibility of the converters in DC charging stations
3. Integration of Grid-Forming Inverters: Integrating grid-forming inverters into the simulated system to better understand their performance and impact on the overall system
4. Energy Management System: Developing energy management system based on peak demand and energy price fluctuations to optimize energy usage and reduce costs.

CITED LITERATURE

1. Safayatullah, M., Elrais, M. T., Ghosh, S., Rezaii, R., and Batarseh, I.: A comprehensive review of power converter topologies and control methods for electric vehicle fast charging applications. IEEE Access, 10:40753–40793, 2022.
2. Yang, D., Zhang, Y., Liu, X., Wang, W., and Liu, J.: Overview of clc modulation strategy. In 2022 International Power Electronics Conference (IPEC-Himeji 2022-ECCE Asia), pages 1633–1640, Himeji, Japan, 2022.
3. Erickson, R. W. and Maksimovic, D.: Fundamentals of Power Electronics. Springer, third edition, 2019.
4. P. Minerva, A. Gohari, M. B. S. and Bayhan, S.: Optimal design and control of dc charging stations using clc converter for grid integration. Manuscript submitted to the 2024 Annual Conference of the IEEE Industrial Electronics Society (IECON), 2024.
5. Gohari, A., Althuwaini, H., and Shadmand, M. B.: Optimal utilization of battery sources in cascaded h-bridge inverter by coordinated sequence selection. IEEE Transactions on Industrial Electronics, 2023.
6. Nazaralizadeh, S., Banerjee, P., Srivastava, A. K., and Famouri, P.: Battery energy storage systems: A review of energy management systems and health metrics. Energies, 17(5):1250, 2024.
7. Guille, C. and Gross, G.: Design of a conceptual framework for the v2g implementation. In 2008 IEEE Energy 2030 Conference, pages 1–3, Atlanta, GA, USA, 2008.
8. Liu, C., Sen, B., Wang, J., Gould, C., and Colombage, K.: A clc resonant converter based bidirectional ev charger with maximum efficiency tracking. In Proc. 8th IET Int. Conf. Power Electron., Mach. Drives (PEMD), pages 1–6, 2016.
9. Hutson, C., Venayagamoorthy, G. K., and Corzine, K. A.: Intelligent scheduling of hybrid and electric vehicle storage capacity in a parking lot for profit maximization in grid power transactions. In 2008 IEEE Energy 2030 Conference, pages 1–8, Atlanta, GA, USA, 2008.

10. Han, S., Han, S., and Sezaki, K.: Development of an optimal vehicle-to-grid aggregator for frequency regulation. IEEE Transactions on Smart Grid, 1(1):65–72, June 2010.
11. Shi, W. and Wong, V. W. S.: Real-time vehicle-to-grid control algorithm under price uncertainty. In 2011 IEEE International Conference on Smart Grid Communications (SmartGridComm), pages 261–266, Brussels, Belgium, 2011.
12. Vadi, S., Bayindir, R., Colak, A. M., and Hossain, E.: A review on communication standards and charging topologies of v2g and v2h operation strategies. Energies, 12(19):3748, 2019.
13. of Energy, U. D.: Efficiency ratios for light-duty all-electric vehicles in the united states. <https://afdc.energy.gov/>, June 2023. Alternative Fuels Data Center. [Online; accessed 13/04/2024].
14. IEA: Comparison of global average lifecycle emissions by powertrain in the stated policies and announced pledges scenarios, 2023-2035. <https://www.iea.org/data-and-statistics/charts/comparison-of-global-average-lifecycle-emissions-by-powertrain-in-the-stated-policies-and-announced-pledges-scenarios-2023-2035>, 2024. IEA, Paris. Licence: CC BY 4.0. [Online; accessed 20/05/2024].
15. IEA: Cumulative renewable electricity capacity in the main and accelerated cases and net zero scenario. <https://www.iea.org/data-and-statistics/charts/cumulative-renewable-electricity-capacity-in-the-main-and-accelerated-cases-and-net-zero-scenario>, 2024. IEA, Paris. Licence: CC BY 4.0. [Online; accessed 20/05/2024].
16. IEA: World energy outlook 2023. <https://www.iea.org/reports/world-energy-outlook-2023>. [Online; accessed 20/05/2024].
17. Kempton, W. and Tomić, J.: Vehicle-to-grid power fundamentals: Calculating capacity and net revenue. Journal of Power Sources, 144(1):268–279, 2005.
18. Yilmaz, M. and Krein, P. T.: Review of benefits and challenges of vehicle-to-grid technology. In 2012 IEEE Energy Conversion Congress and Exposition (ECCE), pages 3082–3089, 2012.
19. Rivera, S., Goetz, S. M., Kouro, S., Lehn, P. W., Pathmanathan, M., Bauer, P., and Mastromauro, R. A.: Charging infrastructure and grid integration for electromobility. Proceedings of the IEEE, 111(4):371–396, 2023.

20. Kyrylenko, O., Denysiuk, S., Strzelecki, R., Blinov, I., Zaitsev, I., and Zaporozhets, A.: Power Systems Research and Operation. 2024. Selected Editors.
21. Tu, H., Feng, H., Srdic, S., and Lukic, S.: Extreme fast charging of electric vehicles: A technology overview. IEEE Transactions on Transportation Electrification, 5(4):861–878, 2019.
22. He, P. and Khaligh, A.: Comprehensive analyses and comparison of 1 kw isolated dc–dc converters for bidirectional ev charging systems. IEEE Transactions on Transportation Electrification, 3(1):147–156, 2017.
23. Morrison, R. and Egan, M.: A new single transformer, power factor corrected ups design. In APEC '98 Thirteenth Annual Applied Power Electronics Conference and Exposition, volume 1, pages 237–243, 1998.
24. Du, Y., Lukic, S., Jacobson, B., and Huang, A.: Review of high power isolated bi-directional dc-dc converters for phev/ev dc charging infrastructure. In 2011 IEEE Energy Conversion Congress and Exposition, pages 553–560, 2011.
25. Inoue, S. and Akagi, H.: A bi-directional dc/dc converter for an energy storage system. In APEC 07 - Twenty-Second Annual IEEE Applied Power Electronics Conference and Exposition, pages 761–767, 2007.
26. Kheraluwala, M., Gascoigne, R., Divan, D., and Baumann, E.: Performance characterization of a high-power dual active bridge dc-to-dc converter. IEEE Transactions on Industry Applications, 28(6):1294–1301, 1992.
27. Guennouni, N., Chebak, A., and Machkour, N.: Optimal dual active bridge dc-dc converter operation with minimal reactive power for battery electric vehicles using model predictive control. Electronics, 11, 05 2022.
28. Gao, G., Lei, W., Lv, G., Li, K., Cui, Y., and Li, T.: The output-voltage-ripple analysis of dual active bridge converter based on a novel ripple recovery technique. In 2019 10th International Conference on Power Electronics and ECCE Asia (ICPE 2019 - ECCE Asia), pages 2409–2414, 2019.
29. Panchanathan, S., Vishnuram, P., Rajamanickam, N., Bajaj, M., Blazek, V., Prokop, L., and Misak, S.: A comprehensive review of the bidirectional converter topologies for the vehicle-to-grid system. Energies, 16(5):2503, 2023.

30. Xuwei, P. and Rathore, A.: Novel bidirectional snubberless naturally commutated soft-switching current-fed full-bridge isolated dc/dc converter for fuel cell vehicles. IEEE Transactions on Industrial Electronics, 61:2307–2315, 2014.
31. Zahid, Z., Dalala, Z., Chen, R., Chen, B., and Lai, J.-S.: Design of bidirectional dc–dc resonant converter for vehicle-to-grid (v2g) applications. IEEE Transactions on Transportation Electrification, 1:232–244, 2015.
32. Xu, B., Wang, H., Sun, H., and Wang, Y.: Design of a bidirectional power converter for charging pile based on v2g. In Proceedings of the 2017 IEEE International Conference on Industrial Technology (ICIT), pages 527–531, Toronto, ON, Canada, March 2017.
33. Olivares-Rodríguez, C., Castillo-Calzadilla, T., and Kamara-Esteban, O.: Bio-inspired approximation to mppt under real irradiation conditions. In Intelligent Distributed Computing XII, volume 798, pages 107–118. Cham, Switzerland, Springer, 2018.
34. Shanmugam, Y., Narayanamoorthi, R., Vishnuram, P., Bajaj, M., AboRas, K., Thakur, P., and Kitmo, A.: Systematic review of dynamic wireless charging system for electric transportation. IEEE Access, 10:133617–133642, 2022.
35. Shi, Y., Li, R., Xue, Y., and Li, H.: Optimized operation of current-fed dual active bridge dc–dc converter for pv applications. IEEE Transactions on Industrial Electronics, 62:6986–6995, 2015.
36. Rathore, A. and Prasanna, U.: Analysis, design, and experimental results of novel snubberless bidirectional naturally clamped zcs/zvs current fed half-bridge dc/dc converter for fuel cell vehicles. IEEE Transactions on Industrial Electronics, 60:4482–4491, 2013.
37. Geetha, A., Subramaniam, N. P., and Gnanadass, R.: Operation of current-fed dual active bridge dc-dc converters for microgrid. International Journal of Recent Technology and Engineering (IJRTE), 8(2):3169–3175, 2019.
38. Sharma, A. and Sharma, S.: Review of power electronics in vehicle-to-grid systems. Journal of Energy Storage, 21:337–361, 2019.
39. Wang, H., Dusmez, S., and Khaligh, A.: Design and analysis of a full-bridge llc-based pev charger optimized for wide battery voltage range. IEEE Transactions on Vehicular Technology, 63(4):1603–1613, April 2014.

40. Haga, H. and Kurokawa, F.: Modulation method of a full-bridge three-level llc resonant converter for battery charger of electrical vehicles. IEEE Transactions on Power Electronics, 32(4):2498–2507, April 2017.
41. Li, B., Lee, F. C., Li, Q., and Liu, Z.: Bi-directional on-board charger architecture and control for achieving ultra-high efficiency with wide battery voltage range. In Proc. IEEE Appl. Power Electron. Conf. Expo. (APEC), pages 3688–3694, March 2017.
42. Zhao, S., Li, Q., Lee, F. C., and Li, B.: High-frequency transformer design for modular power conversion from medium-voltage ac to 400 vdc. IEEE Transactions on Power Electronics, 33(9):7545–7557, 2018.
43. Chen, W., Rong, P., and Lu, Z.: Snubberless bidirectional dc–dc converter with new clc resonant tank featuring minimized switching loss. IEEE Transactions on Industrial Electronics, 57(9):3075–3086, 2010.
44. Zou, S., Lu, J., Mallik, A., and Khaligh, A.: Bi-directional clc converter with synchronous rectification for plug-in electric vehicles. IEEE Transactions on Industry Applications, 54(2):998–1005, 2018.
45. Zhang, Z., Liu, C., Wang, M., Si, Y., Liu, Y., and Lei, Q.: High-efficiency high-power-density clc resonant converter with low-stray-capacitance and well-heat-dissipated planar transformer for ev on-board charger. IEEE Transactions on Power Electronics, 35(10):10831–10851, 2020.
46. Wang, C.-S., Zhang, S.-h., Wang, Y.-f., Chen, B., and Liu, J.-h.: A 5-kw isolated high voltage conversion ratio bidirectional cltc resonant dc–dc converter with wide gain range and high efficiency. IEEE Transactions on Power Electronics, 34(1):340–355, 2019.
47. Huang, J., Zhang, X., Shuai, Z., Zhang, X., Wang, P., Koh, L. H., Xiao, J., and Tong, X.: Robust circuit parameters design for the clc-type dc transformer in the hybrid ac–dc microgrid. IEEE Transactions on Industrial Electronics, 66(3):1906–1918, 2019.
48. Li, B., Li, Q., Lee, F. C., Liu, Z., and Yang, Y.: A high-efficiency high-density wide-bandgap device-based bidirectional on-board charger. IEEE Journal of Emerging and Selected Topics in Power Electronics, 6(3):1627–1636, 2018.

49. Cao, Y., Ngo, M., Burgos, R., Ismail, A., and Dong, D.: Switching transition analysis and optimization for bidirectional clc resonant dc transformer. IEEE Transactions on Power Electronics, 37(4):3786–3800, April 2022.
50. Xu, B., Wang, H., Sun, H., and Wang, Y.: Design of a bidirectional power converter for charging pile based on v2g. 2017 IEEE International Conference on Industrial Technology (ICIT), pages 527–531, 2017.
51. Wang, X., Jiang, C., Lei, B., Teng, H., Bai, H. K., and Kirtley, J. L.: Power-loss analysis and efficiency maximization of a silicon-carbide mosfet-based three-phase 10-kw bidirectional ev charger using variable-dc-bus control. IEEE Journal of Emerging and Selected Topics in Power Electronics, 4(3):880–892, 2016.
52. Zou, S., Lu, J., Mallik, A., and Khaligh, A.: Bi-directional clc converter with synchronous rectification for plug-in electric vehicles. IEEE Transactions on Industry Applications, 54(2):998–1005, 2018.
53. Lee, B.-K., Kim, J.-P., Kim, S.-G., and Lee, J.-Y.: An isolated/bidirectional pwm resonant converter for v2g(h) ev on-board charger. IEEE Transactions on Vehicular Technology, 66(9):7741–7750, 2017.
54. Zahid, Z. U., Dalala, Z. M., Chen, R., Chen, B., and Lai, J.: Design of bidirectional dc-dc resonant converter for vehicle-to-grid (v2g) applications. IEEE Transactions on Transportation Electrification, 1(3):232–244, 2015.
55. Wei, Y., Woldegiorgis, D., and Mantooh, A.: Control strategies overview for llc resonant converter with fixed frequency operation. In 2020 IEEE 11th International Symposium on Power Electronics for Distributed Generation Systems (PEDG), pages 63–68, 2020.
56. Wei, Y., Luo, Q., and Mantooh, A.: Overview of modulation strategies for llc resonant converter. IEEE Transactions on Power Electronics, 35(10):10423–10443, 2020.
57. Liu, W., Wang, B., Yao, W., Lu, Z., and Xu, X.: Steady-state analysis of the phase shift modulated llc resonant converter. In Proc. IEEE Energy Convers. Congr. Expo., pages 1–5, Milwaukee, WI, USA, 2016.
58. Kollipara, N., Kazimierczuk, M. K., Reatti, A., and Corti, F.: Phase control and power optimization of llc converter. In Proc. IEEE Int. Symp. Circuits Syst., pages 1–5, Sapporo, Japan, 2019.

59. Murata, K. and Kurokawa, F.: Performance characteristic of interleaved llc resonant converter with phase shift modulation. In Proc. IEEE Int. Telecommun. Energy Conf., pages 1–5, Osaka, Japan, 2015.
60. Wu, H., Mu, T., Gao, X., and Xing, Y.: A secondary-side phase-shift controlled llc resonant converter with reduced conduction loss at normal operation for hold-up time compensation application. IEEE Trans. Power Electron., 30(10):5352–5357, Oct. 2015.
61. Sun, X., Li, X., Shen, Y., Wang, B., and Guo, X.: Dual-bridge llc resonant converter with fixed-frequency pwm control for wide input applications. IEEE Trans. Power Electron., 32(1):69–80, Jan. 2017.
62. Wang, H. and Li, Z.: A pwm llc type resonant converter adapted to wide output range in pev charging applications. IEEE Trans. Power Electron., 33(5):3791–3801, May 2018.
63. Zhu, T., Zhuo, F., Zhao, F., Wang, F., Yi, H., and Zhao, T.: Optimization of extended phase-shift control for full-bridge clc resonant converter with improved light-load efficiency. IEEE Transactions on Power Electronics, 35(10):11129–11142, Oct. 2020.
64. Hua, W., Wu, H., Yu, Z., Xing, Y., and Sun, K.: A phase-shift modulation strategy for a bidirectional clc resonant converter. In 2019 10th International Conference on Power Electronics and ECCE Asia (ICPE 2019 - ECCE Asia), pages 1–6, 2019.
65. Zhu, T., Zhuo, F., Zhao, F., Yu, K., Wang, F., and Song, R.: A novel apwm control scheme for gan based full-bridge clc resonant converter with improved light-load efficiency. In 2020 IEEE Applied Power Electronics Conference and Exposition (APEC), pages 2081–2085, 2020.
66. Shucheng, L., Bangyin, L., Qing, J., and Shanxu, D.: Analysis of operating characteristics of bidirectional clc resonant dc converter based on synchronous pwm control. Transactions of the China Electrotechnical Society, 34(S2):543–552, 2019.
67. Mishima, T. and Koga, Y.: Variable frequency phase-difference controlled clc resonant bidirectional dc-dc converter featuring wide-range zvs performance and reactive power reduction. In 2018 IEEE Energy Conversion Congress and Exposition (ECCE), pages 6283–6290, 2018.

68. Zong, S., Luo, H., Li, W., Deng, Y., and He, X.: Asymmetrical duty cycle-controlled llc resonant converter with equivalent switching frequency doubler. IEEE Transactions on Power Electronics, 31(7):4963–4973, July 2016.
69. Lu, X. and Wang, H.: Three-port bidirectional clc resonant converter based on-board charger for pev hybrid energy management system. In 2017 IEEE Energy Conversion Congress and Exposition (ECCE), pages 1432–1438, 2017.
70. Yuan, Y., Tong, X., Huang, J., Zhang, W., Xiao, J., and Koh, L. H.: Power flow analysis of three-port resonant dc transformer and discussion on phase shift control. In 2020 15th IEEE Conference on Industrial Electronics and Applications (ICIEA), pages 1242–1247, 2020.
71. Rivera, S., Goetz, S. M., Kouro, S., Lehn, P. W., Pathmanathan, M., Bauer, P., and Mastromauro, R. A.: Charging infrastructure and grid integration for electromobility. Proceedings of the IEEE, 111(4):371–396, 2023.
72. Blaabjerg, F., Teodorescu, R., Liserre, M., and Timbus, A.: Overview of control and grid synchronization for distributed power generation systems. IEEE Transactions on Industrial Electronics, 53(5):1398–1409, 2006.
73. Rocabert, J., Luna, A., Blaabjerg, F., and Rodríguez, P.: Control of power converters in ac microgrids. IEEE Transactions on Power Electronics, 27(11):4734–4749, 2012.
74. Fang, J., Tang, Y., Li, H., and Li, X.: A battery/ultracapacitor hybrid energy storage system for implementing the power management of virtual synchronous generators. IEEE Transactions on Power Electronics, 33(4):2820–2824, 2018.
75. Svensson, J.: Synchronization methods for grid-connected voltage source converter. Generation, Transmission and Distribution, IEE Proceedings-, 148:229 – 235, 06 2001.
76. Zhong, Q.-C., Nguyen, P.-L., Ma, Z., and Sheng, W.: Self-synchronized synchronverters: inverters without a dedicated synchronization unit. IEEE Transactions on Power Electronics, 29(2):617–630, February 2014.
77. Liserre, M., Teodorescu, R., and Blaabjerg, F.: Stability of photovoltaic and wind turbine grid-connected inverters for a large set of grid impedance values. IEEE Transactions on Power Electronics, 21(1):263–272, January 2006.

78. Fang, J., Lin, P., Li, H., Yang, Y., and Tang, Y.: An improved virtual inertia control for three-phase voltage source converters connected to a weak grid. IEEE Transactions on Power Electronics, 34(9):8660–8670, September 2019.
79. Natarajan, V. and Weiss, G.: Synchronverters with better stability due to virtual inductors, virtual capacitors, and anti wind-up. IEEE Transactions on Industrial Electronics, 64(7):5994–6004, July 2017.
80. Unruh, P., Nuschke, M., Strauß, P., and Welck, F.: Overview on grid-forming inverter control methods. Energies, 13(10):2589, 2020.
81. Williams, D. O., Li, Z. S., Luo, X., Zhang, Q., Maslennikov, S., and Tbaileh, A.: An overview of industry-related grid forming inverter controls. In 2023 Global Reliability and Prognostics and Health Management Conference (PHM-Hangzhou), pages 1–9, Hangzhou, China, 2023.
82. Jung, J., Kim, H., Ryu, M., and Baek, J.: Design methodology of bidirectional clc resonant converter for high-frequency isolation of dc distribution systems. IEEE Transactions on Power Electronics, 28(4):1741–1755, 2012.
83. He, P. and Khaligh, A.: Comprehensive analyses and comparison of 1 kw isolated dc–dc converters for bidirectional ev charging systems. IEEE Transactions on Transportation Electrification, 3(1):147–156, 2016.
84. He, P. and Khaligh, A.: Comprehensive analyses and comparison of 1 kw isolated dc–dc converters for bidirectional ev charging systems. IEEE Transactions on Transportation Electrification, 3(1):147–156, 2017.
85. Jung, J.-H., Kim, H.-S., Ryu, M.-H., and Baek, J.-W.: Design methodology of bidirectional clc resonant converter for high-frequency isolation of dc distribution systems. IEEE Transactions on Power Electronics, 28(4):1741–1755, 2013.
86. Liu, X., Wu, X., and Wang, H.: Parameters analysis and control strategy combined with synchronous rectification technology for bidirectional clc resonant converter. Electrical Engineering, 105:1397–1412, 2023.
87. Lv, Z., Yan, X., Fang, Y., and Sun, L.: Mode analysis and optimum design of bidirectional clc resonant converter for high-frequency isolation of dc distribution systems. In 2015 IEEE Energy Conversion Congress and Exposition (ECCE), pages 1513–1520, 2015.

88. Siebke, K., Schobre, T., and Mallwitz, R.: Comparison of gan based clc converters for ev chargers operating at different switching frequency ranges. In 2019 21st European Conference on Power Electronics and Applications (EPE'19 ECCE Europe), pages P-1. IEEE, 2019.
89. Tabari, M. and Yazdani, A.: A mathematical model for stability analysis of a dc distribution system for power system integration of plug-in electric vehicles. IEEE Transactions on Vehicular Technology, 64(5):1729–1738, May 2015.

VITA

- NAME** Pietro Minerva
- EDUCATION** B.Sc. Mechanical Engineering, Politecnico di Torino, Italy 2022.
M.Sc. Mechatronics Engineering, Politecnico di Torino, Italy 2024.
M.Sc. Electrical and Computer Engineering, University of Illinois Chicago, Chicago, IL, USA, 2024.
- PAPER** Pietro Minerva, A. Gohari, Mohammad B. Shadmand, and S. Bayhan. “Optimal Design and Control of DC Charging Stations Using CLLC Converter For Grid Integration” Manuscript accepted for publication at the 2024 Annual Conference of the IEEE Industrial Electronics Society (IECON, 2024).